

Influence of the Sweep Angle on the Leading Edge Vortex and its Relation to the
Power Extraction Performance of a Fully-Passive Oscillating-Plate Hydrokinetic
Turbine Prototype

by

Walfred Lee

B.Eng. Nagoya University, 2018

A Thesis Submitted in Partial Fulfillment of the
Requirements for the Degree of

MASTER OF APPLIED SCIENCE

in the Department of Mechanical Engineering

© Walfred Lee, 2021
University of Victoria

All rights reserved. This thesis may not be reproduced in whole or in part, by
photocopying or other means, without the permission of the author.

Influence of the Sweep Angle on the Leading Edge Vortex and its Relation to the
Power Extraction Performance of a Fully-Passive Oscillating-Plate Hydrokinetic
Turbine Prototype

by

Waltfred Lee
B.Eng. Nagoya University, 2018

Supervisory Committee

Dr. Peter Oshkai, Supervisor
Department of Mechanical Engineering

Dr. Brad Buckham, Departmental Member
Department of Mechanical Engineering

ABSTRACT

Oscillating-foil hydrokinetic turbines have gained interest over the years to extract energy from renewable sources. The influence of the sweep angle on the performance of a fully-passive oscillating-plate hydrokinetic turbine prototype was investigated experimentally in the present work. The sweep angle was introduced to promote spanwise flow along the plate in order to manipulate the leading edge vortex (LEV) and hydrodynamically optimize the performance of the turbine.

In the present work, flat plates of two configurations were considered: a plate with a 6° sweep angle and an unswept plate (control), which were undergoing fully-passive pitch and heave motions in uniform inflow at the Reynolds numbers ranging from 15 000 to 30 000. The resulting kinematic parameters and the energy extraction performance were evaluated for both plates.

Planar (2D) particle image velocimetry (PIV) was used to obtain patterns of the phase-averaged out-of-plane vorticity during the oscillation cycle. The circulation in the wake was then related to the induced-forces on the plate by calculating the moments of vorticity of the LEV with respect to the pitching axis of the plate.

Tomographic (3D) PIV was implemented in evaluating the influence of the spanwise flow on the dynamics of the vortex structure in three-dimensional space. The rate of deformation of the vortex length was quantified by calculating the deformation terms embedded in the vorticity equations, then linked to the stability of the vortex.

The results show evidence of delay of the shedding of LEV and increased vortex stability, in the case of the swept plate. The manipulation of the LEV by the spanwise flow was related to the induced kinematics exhibited by the prolonged heave forces experienced by the swept plate, which led to the higher power extraction performance at high inflow velocities. In the presence of spanwise flow, positive vortex stretching along the vortex line increased the stabilization of the vortex core and prevented the onset of helical vortex breakdown, observed in the case of the unswept plate. The use of the sweep profile on the plate has led to the improvement of energy extraction performance of the fully-passive hydrokinetic turbine.

Contents

Supervisory Committee	ii
Abstract	iii
Contents	iv
List of Figures	vi
List of Tables	x
Acknowledgements	xiv
1 Introduction	1
1.1 Hydrokinetic energy	1
1.2 Oscillating-foil turbine	3
1.3 Optimization of oscillating-foil turbines	7
1.4 Spanwise flow component	9
1.5 Objectives	11
1.6 Structure of the thesis	12
2 Experimental system and techniques	13
2.1 Fully-passive turbine prototype	13
2.2 Experimental setup	18
2.3 Experimental techniques	20
3 Quantitative flow imaging	22
3.1 Planar (2D) Particle Image Velocimetry	22
3.2 Tomographic (3D) Particle Image Velocimetry	23
4 Hydrokinetic performance of the oscillating-foil turbine	26

4.1	Baseline case of the unswept oscillating-plate	26
4.2	Effects of the inflow velocity on the turbine performance	27
5	Quantitative flow patterns	32
5.1	Two-dimensional flow patterns	32
5.2	Contributions of the shed vorticity to the instantaneous forces on the plate	38
5.3	Three-dimensional vortex structure	43
5.3.1	Spanwise variation of the structure of the LEV	45
5.3.2	Inner structure and stability of the core of the LEV	48
5.3.3	Deformation and stretching of the LEV	48
6	Conclusion	58
6.1	Future Work	60
Appendix A Validation of vector fields acquired from Planar PIV		62
Appendix B Assessment of the Tomographic PIV data quality		64
B.1	Quality of the tomographic reconstruction	64
B.2	Quality of the vector calculation	65
Appendix C Illuminated region and the ghost intensity		69
Appendix D Influence of the bottom endplate		72
Appendix E Standard deviations of the kinematic and performance parameters		75
Bibliography		78

List of Figures

Figure 1.1	Types of cross-flow hydrokinetic turbines: vertical-axis turbine (a) and oscillating-foil turbine (b). Adapted from [8].	3
Figure 1.2	General concept of an oscillating foil over one period.	4
Figure 1.3	Vector components of the flow on the infinite-span swept wing.	9
Figure 2.1	Schematic of the passively oscillating-plate.	14
Figure 2.2	The setup of the fully-passive turbine prototype on the water channel.	19
Figure 2.3	Schematic of the unswept plate (a) and the swept plate (b) in the side view.	20
Figure 3.1	Schematic of the Particle Image Velocimetry setup.	24
Figure 4.1	Turbine performance and kinematic parameters functions of inflow velocity (U_∞). Open symbols (\circ) represent results of the unswept plate ($\Lambda = 0^\circ$) and filled symbols (\bullet) represent results of the swept plate ($\Lambda = 6^\circ$). The initial and final viscous damping and coulomb friction of each series of test were: $D_{h,v}^* = [0.09 - 0.11]$; $D_\theta^* = [0.007 - 0.007]$; $C_{FyCoulomb} = [0.01 - 0.04]$; $C_{MCoulomb} = [0.006 - 0.006]$ and $D_{h,v}^* = [0.09 - 0.10]$; $D_\theta^* = [0.007 - 0.007]$; $C_{FyCoulomb} = [0.02 - 0.01]$; $C_{MCoulomb} = [0.006 - 0.006]$ for the unswept plate and swept plate, respectively. The vertical dashed line corresponds to the baseline case.	29
Figure 4.2	Reduced frequency (solid black), reduced heave natural frequency (dashed blue) and reduced pitch natural frequency (dashed red) as a function of the inflow velocity (U_∞) for the unswept plate ($\Lambda = 0^\circ$) (a) and the swept plate ($\Lambda = 6^\circ$) (b).	30

Figure 5.1 Phase-averaged out-of-plane dimensionless vorticity fields at sequential phases $t^* = 0/10$ (i), $1/10$ (ii), $2/10$ (iii), $3/10$ (iv) and $4/10$ (v) for the unswept plate ($\Lambda = 0^\circ$) at $z^* = 0.5$. The filled symbol (\bullet) corresponds to the location of the pitching axis. The flow velocity $U_\infty = 0.41$ m/s was directed from top to bottom.	33
Figure 5.2 Phase-averaged out-of-plane dimensionless vorticity fields at sequential phases $t^* = 0/10$ (i), $1/10$ (ii), $2/10$ (iii), $3/10$ (iv) and $4/10$ (v) for the swept plate ($\Lambda = 6^\circ$) at $z^* = 0.5$. The filled symbol (\bullet) corresponds to the location of the pitching axis. The flow velocity $U_\infty = 0.41$ m/s was directed from top to bottom.	34
Figure 5.3 Phase-averaged out-of-plane dimensionless vorticity fields at sequential phases, $t^* = 0/10$ (i), $1/10$ (ii), $2/10$ (iii), $3/10$ (iv) and $4/10$ (v) for the swept plate ($\Lambda = 6^\circ$) at $z^* = 0.88$. The filled symbol (\bullet) corresponds to the location of the pitching axis. The flow velocity $U_\infty = 0.41$ m/s was directed from top to bottom.	35
Figure 5.4 Calculated moments of vorticity $(M_\omega)_x$ (a) and $(M_\omega)_y$ (b) of the vortex A (\bullet) and the vortex B (\circ) for the unswept plate ($\Lambda = 0^\circ$) at $z^* = 0.5$	39
Figure 5.5 Calculated moments of vorticity $(M_\omega)_x$ (a) and $(M_\omega)_y$ (b) of the vortex A (\bullet) and the vortex B (\circ) for the swept plate ($\Lambda = 6^\circ$) at $z^* = 0.5$	40
Figure 5.6 Calculated moments of vorticity $(M_\omega)_x$ (a) and $(M_\omega)_y$ (b) of the vortex A (\bullet) and the vortex B (\circ) for the swept plate ($\Lambda = 6^\circ$) at $z^* = 0.88$	41
Figure 5.7 Location of the vortex A (a) at phase $t^* = 2/10$ to $t^* = 4/10$ and the vortex B (b) at phase $t^* = 0/10$ to $t^* = 4/10$ with respect to the pitching axis.	42
Figure 5.8 Schematic of the location of the tomographic PIV data acquisition volume with reference to the plate and the 2D vorticity plots at $t^* = 1/10$	45
Figure 5.9 Iso-surface of the Q criterion of the vortex B in the case of the unswept plate ($\Lambda = 0^\circ$) at phase $t^* = 1/10$. Axonometric view (a), y -normal view (b) and x -normal view (c).	46

Figure 5.10	Iso-surface of the Q criterion of the vortex B in the case of the swept plate ($\Lambda = 6^\circ$) at phase $t^* = 1/10$. Axonometric view (a), y -normal view (b) and x -normal view (c).	47
Figure 5.11	Iso-surfaces of the vorticity turning term $(\omega \cdot \nabla)U_\top = \pm 75$ in the x -direction (a), y -direction (b) and z -direction (c) for the case of the unswept plate ($\Lambda = 0^\circ$). The iso-surface of the $Q = 15$ is indicated by the light pink colour.	51
Figure 5.12	Iso-surfaces of the vorticity turning term $(\omega \cdot \nabla)U_\perp = \pm 75$ in the x -direction (a), y -direction (b) and z -direction (c) for the case of the unswept plate ($\Lambda = 0^\circ$). The iso-surface of the $Q = 15$ is indicated by the light pink colour.	52
Figure 5.13	Iso-surfaces of the vorticity turning term $(\omega \cdot \nabla)U_\top = \pm 75$ in the x -direction (a), y -direction (b) and z -direction (c) for the case of the swept plate ($\Lambda = 6^\circ$). The iso-surface of the $Q = 15$ is indicated by the light pink colour.	53
Figure 5.14	Iso-surfaces of the vorticity turning term $(\omega \cdot \nabla)U_\perp = \pm 75$ in the x -direction (a), y -direction (b) and z -direction (c) for the case of the swept plate ($\Lambda = 6^\circ$). The iso-surface of the $Q = 15$ is indicated by the light pink colour.	54
Figure 5.15	Iso-surfaces of the vorticity stretching term $(\omega \cdot \nabla)U_\parallel = \pm 75$ in the x -direction (a), y -direction (b) and z -direction (c) for the case of the unswept plate ($\Lambda = 0^\circ$). The iso-surface of the $Q = 15$ is indicated by the light pink colour.	56
Figure 5.16	Iso-surfaces of the vorticity stretching term $(\omega \cdot \nabla)U_\parallel = \pm 75$ in the x -direction (a), y -direction (b) and z -direction (c) for the case of the swept plate ($\Lambda = 6^\circ$). The iso-surface of the $Q = 15$ is indicated by the light pink colour.	57
Figure A.1	The number of instantaneous vorticity fields and the calculated averaged moment of vorticity in the x -component (a) and y -component (b).	63
Figure B.1	Measured intensity by the dual-pulse laser across the reconstructed volume in the case of unswept plate ($\Lambda = 0^\circ$) (a) and swept plate ($\Lambda = 0^\circ$) (b).	66

Figure B.2 Joint PDFs of the $\delta U_y/\delta y$ and $-(\delta U_x/\delta x + \delta U_z/\delta z)$ in the case of the unswept plate ($\Lambda = 0^\circ$) at $z = 207$ mm (a) and $z = 213$ mm (b), and averaged across the VOI (c). There are 15 contour levels.	67
Figure B.3 Joint PDFs of the $\delta U_y/\delta y$ and $-(\delta U_x/\delta x + \delta U_z/\delta z)$ in the case of the swept plate ($\Lambda = 6^\circ$) at $z = 207$ mm (a) and $z = 213$ mm (b), and averaged across the VOI (c). There are 15 contour levels. 68	68
Figure C.1 An example of the x -normal view of the tomographic volume reconstruction at pulse 1 (a) and pulse 2 (b).	70
Figure C.2 An example of the y -normal view of the tomographic volume reconstruction at pulse 1 (a) and pulse 2 (b).	71
Figure E.1 Time evolution of the normalized heave (a) and pitch (b) positions of the unswept plate ($\Lambda = 0^\circ$) over 10 cycles at $U_\infty = 0.452$ m/s.	75

List of Tables

Table 2.1	Variables and terms involved in the governing equations of motion. Adapted from [44].	16
Table 4.1	The normalized structural parameters of the unswept plate at the baseline case.	27
Table D.1	Kinematic and performance parameters of the plates, with and without the presence of the bottom endplate. The initial and final viscous damping and coulomb friction of each series of test were: $D_{h,v}^* = [0.09 - 0.11]$; $D_{\theta}^* = [0.007 - 0.005]$; $C_{FyCoulomb} = [0.03 - 0.01]$; $C_{MCoulomb} = [0.01 - 0.01]$ and $D_{h,v}^* = [0.10 - 0.13]$; $D_{\theta}^* = [0.018 - 0.007]$; $C_{FyCoulomb} = [0.03 - 0.05]$; $C_{MCoulomb} = [0.02 - 0.01]$ for the unswept plate ($\Lambda = 0^\circ$) and swept plate ($\Lambda = 6^\circ$), respectively.	73
Table E.1	Standard deviations of the kinematic and performance parameters of the unswept plate ($\Lambda = 0^\circ$), presented in Fig 4.1.	76
Table E.2	Standard deviations of the kinematic and performance parameters of the swept plate ($\Lambda = 6^\circ$), presented in Fig 4.1.	76
Table E.3	Standard deviations of the kinematic and performance parameters of the plates, with and without the attachment of the bottom endplate, presented in Table D.1.	77

List of Symbols

$(\omega \cdot \nabla)U_{\parallel}$	Vorticity stretching term
$(\omega \cdot \nabla)U_{\perp}$	Vorticity turning term
$(\omega \cdot \nabla)U_{\top}$	Vorticity turning term
β	Aperture angle
\mathbf{S}	Rate of strain tensor
η	Efficiency
Ω	Rate of rotation tensor
ω	Vorticity
ϕ	Phase lag
ρ	Density
θ	Pitch angle
\wedge	Sweep angle
b	True span length
b'	Effective span length
c	Streamwise chord length
c'	Effective chord length
C_p	Power coefficient

$C_{FyCoulomb}$	Coulomb friction force coefficient in heave
C_{Fy}	Hydrodynamic force coefficient in heave
$C_{MCoulomb}$	Coulomb friction moment of force coefficient
C_M	Hydrodynamic moment of force coefficient
D_θ	Pitch bearings damping coefficient
D_h	Linear heaving damping coefficient
$D_{h,v}$	Heave bearings damping coefficient
$D_{h,e}$	Eddy-current brake damping coefficient
f^*	Reduced frequency
$f_{n,\theta}^*$	Reduced pitch natural frequency
$f_{n,h}^*$	Reduced heave natural frequency
h	Heave position
H_0	Heave amplitude
H_0^*	Normalized heave amplitude
I_θ	Moment of inertia
$I_{insideVOI}$	Intensity within the VOI
$I_{outsideVOI}$	Intensity outside of the VOI
k_θ	Pitch stiffness constant
k_h	Heave stiffness constant
M_ω	Moment of vorticity
m_h	Heaving mass
P_0	Pitch amplitude
Q	Q criterion

R^2	Correlation coefficient
Re	Reynolds number
S	Static moment
t^*	Phase
U	Flow velocity
x_θ	Location of centre of mass from pitching axis
x_p	Location of pitching axis from the leading edge
z^*	Spanwise location of PIV DAP/DAV

Abbreviations

2D	Two-dimensional
3D	Three-dimensional
DAP	Data acquisition plane
DAV	Data acquisition volume
LEV	Leading edge vortex
PDF	Probability density function
PIV	Particle image velocimetry
SNR	Signal-to-noise ratio
TSR	Tip speed ratio
VOI	Volume of interest

ACKNOWLEDGEMENTS

I would like to thank:

Dr. Peter Oshkai, for the opportunity of a lifetime. Your passionate guidance and expertise have made this academic journey a memorable one, and your teachings will continue to inspire me.

Dr. Guy Dumas, and his research team at Université Laval on sharing their knowledge on oscillating-foils and their state-of-the-art fully-passive oscillating-foil turbine prototype.

Mostafa Rahimpour and Dylan Iverson for taking the time and effort to show me the ropes. Your invaluable insights have made this academic work possible and are gratefully appreciated.

Research groupmates, Duncan McIntyre, Sierra Mann, Osman Uluocak and Gleb Shrikov, for driving me to keep doing better.

And my partner Celebi Wan, for always being there for me.

Chapter 1

Introduction

1.1 Hydrokinetic energy

In the current energy and economic climate of the world, the cost of energy from conventional fossil fuel sources is targeted to increase [1], while its sources grow scarce. At this pace of the development of societies, anthropogenic emissions are not slowing down [2], and any proposed policy, such as the Paris Agreement, to contain climate change appears to be lacking [3]. The environmental demise will be inevitable without the substitutions of hydrocarbons as the primary energy source. Efforts to utilize renewable environmental sources for energy, such as rivers and biofuels have begun in several countries.

However, green energy harvesting at a large scale requires strong economic development of government and scientific infrastructure to ensure sustainable development [4]. This means the switch from hydrocarbons to renewable sources is not as simple as the flickering of a light switch. Countries would have to strike a balance between economic growth and energy efficiency, and here is where most developing countries would favour the prior. Nevertheless, the adaptation of green energy at the large scale had started across the world, demonstrated by the use of large windmills, hydro dams and solar farms.

Over the years, many forms of energy harvesting devices from various sources of energy have been proposed. The interest in energy harvesting via hydrodynamic energy conversion has been gradually growing. Rapid urbanization usually located close to body of waters, such as coastal waters and waterways, are within reach of hydrodynamic potential energy. Not to mention, the significantly higher energy

density of fluid flow, compared to wind, makes these moving bodies of water attractive sources of energy. Furthermore, water flows are more consistent and predictable, which can lead to efficient integration of energy into the electrical grid.

In recent years, there has been an abundance of research and progress on the development of hydrokinetic turbines, which focuses on the conversion of hydrodynamic energy, from their surroundings into usable mechanical energy. Hydrokinetic turbines specifically cross-flow turbines show great promise in energy harvesting from moving bodies of water with shallow depths. Cross-flow turbines are devices with their rotational axis oriented perpendicularly to the incoming flow direction, which take advantage of lower channel depths through the effective use of extraction windows that are extended in the lateral direction. The extraction window, in this case, is a rectangular swept area which is wider orthogonally and narrower vertically, suitable for low depth applications [5]. Cross-flow turbines can be implemented into unconventional places such as shallow streams and non-uniform tidal currents, urban water supply pipelines [6] and even the recapture of energy from the tailraces of dams [7]. In fact, the application of such technologies can be considered a potential solution to the energy crisis in rural and remote communities due to its applicability at unconventional locations.

There are two common types of cross-flow turbines: the vertical-axis turbine and the oscillating-foil turbine, presented in Fig. 1.1(a) and Fig. 1.1(b), respectively [8]. Vertical-axis turbines are classified as a rotary type turbine, consisting of several blades revolving about the axis perpendicular to the flow. Depending on the configurations of the blades, the rotary-type cross-flow turbines are further classified into multiple types such as the Darrieus turbines, Gorlov turbine, Savonius turbine and more [5] [9] [10] [11]. Vertical-axis turbines are insensitive to the direction of the incoming flow and can achieve efficiencies comparable with their counterpart, horizontal-axis turbines [11] [12].

However, vertical-axis turbines suffer from the fundamental problem of scaling, that is common in rotary systems. Rotary systems are limited by the balance between three factors: the size of the blade (considering the construction strength to overcome the centrifugal forces), the available velocity of the incoming flow and the resulting power coefficient. These three factors define the tip-speed ratio (TSR), the ratio between the tangential speed of the blade tip to the speed of the incoming flow. Peak energy extraction efficiency can only be achieved at optimal TSR, and beyond the optimal value, the efficiency reduces drastically [13] [14] [15]. The scaling of

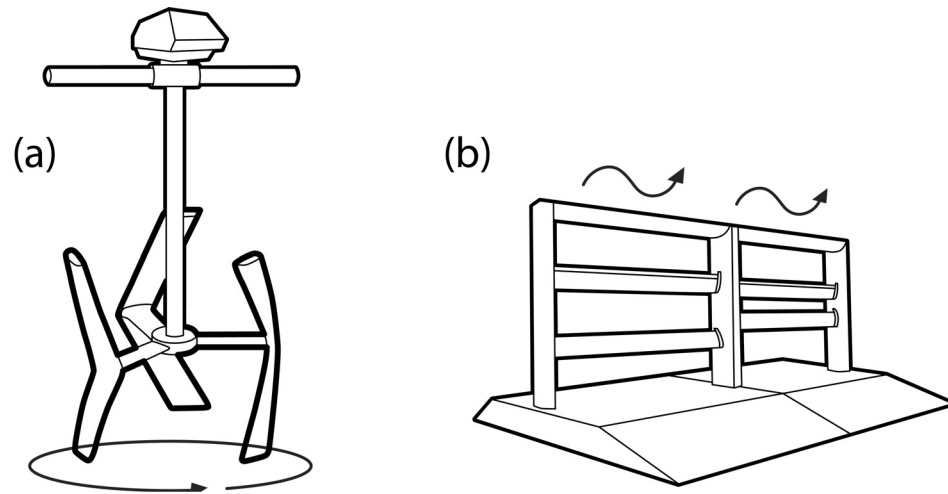


Figure 1.1: Types of cross-flow hydrokinetic turbines: vertical-axis turbine (a) and oscillating-foil turbine (b). Adapted from [8].

the size of the rotary turbine changes the TSR value, in which limits the range of optimal operational conditions, further reducing the area of application for increasing turbine sizes. Furthermore, rotating blades are also prone to cavitation at the tips, generating high-frequency noises. Large scale implementation of rotary turbine farms will eventually add on to the list of anthropogenic noise pollution [16].

Therefore, there is a recent shift of interest in the field of cross-flow turbines into the oscillating-foil concept. Oscillating-foil turbines pose as an attractive alternative to the traditional rotary turbines, which overcome the issues mentioned on scaling and noise. The oscillating-foil turbine concept is the main subject of this thesis and will be thoroughly described in the following sections.

1.2 Oscillating-foil turbine

Oscillating-foils

Oscillating-foils are streamline bodies moving in two degrees of freedom within a given flow, undergoing heaving motion and pitching motion. The heaving motion corresponds to the movement of the foil in the direction perpendicular to the direction of flow. The pitching motion corresponds to the axial rotation of the foil about its pitching axis. The heave and pitch motions can be described as a function of time, $h(t)$ and $\theta(t)$, respectively. The amplitude of the heave motion, H_0 corresponds to the maximum displacement of the pitching axis from the equilibrium position. The

amplitude of the pitch motion, P_0 corresponds to the maximum pitch angle about the pitching axis. Fig. 1.2 summarises these concepts visually over one oscillation cycle.

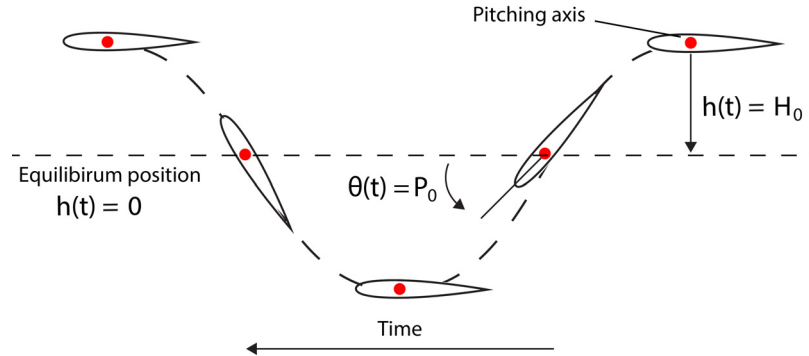


Figure 1.2: General concept of an oscillating foil over one period.

The concept of oscillating-foils is inspired by nature. Oscillating-foil adopts the principle of repetitive oscillatory motion of rotation and the motion of translation of streamline body, which is usually seen in the flapping of bird's wings, beating of insect's wings and undulation of fish's caudal fin. Scientists have found out that flapping-wings utilizes the significant adverse pressure gradient caused by the manipulation of the leading edge vortex (LEV) [17]. The pressure gradient creates high instantaneous lift forces. This mechanism provides the means for small-scale wings of insects to carry their own weight [18] and the high manoeuvrability performed by fish [19].

The study of oscillating-foils undergoing pitch and heave motions has grown over the years. As a matter of fact, with the current accelerated progress in technological advancement, the study of oscillating-foils has grown tenfold in the 21st century [20] [21]. Oscillating-foils can produce high instantaneous forces by utilizing certain unsteady flow features, unlike traditional rotary turbines, that are dependent on smoothly attached flows. Extensive research has been done to adopt the concept of oscillating-foil, not only into propulsion systems, such as unmanned machines [22], ships and submarines [23] [24], but also onto energy extraction devices.

However, strict kinematic profile must be imposed on the foil to appropriately function an oscillating-foil system. Meticulous control of the simultaneous motion of heave and pitch is required to achieve a high level of performance. These motions must also be constrained under unsteady flow features to prevent damping or uncontrolled positive feedback. The control and constraint of such a system involve the use of intricate mechanical design of the degrees of freedom. Computationally, the modelling

of such systems has a certain level of complexity as well. The difficulty of such balance between the control and constraint of the degrees of freedom is deemed the primary cause of the absence of practicable deployment of oscillating-foil technologies at a large scale, at the moment.

Fully-active oscillating-foil turbines

The adoption of the oscillating-foil concept on energy harvesting application was first suggested by McKinney and DeLaurier [25] in the form of a fully-active oscillating foil. Full-active oscillating foil turbines are specific to turbines with actively prescribed motions in both heave and pitch of the foil. These motions are usually prescribed sinusoidally with a phase lag between the heave and pitch. The sinusoidal heaving motion, $h(t)$ and pitching motion, $\theta(t)$ can be defined in the function of time as:

$$h(t) = H_0 \sin(\gamma t + \phi) \quad (1.1)$$

$$\theta(t) = \theta_0 \sin(\gamma t) \quad (1.2)$$

where θ_0 is the pitching amplitude, H_0 is the heaving amplitude, γ is the angular frequency, ϕ is the phase lag and t is the time. Physically, these prescribed motions are either constrained by mechanical links attached between the heave and pitch, or prescribed individually by direct control of forces, usually generated electrically.

Extensive compilations of research on oscillating-foil technologies in regards to energy harvesting applications can be found in the reviews by Young et al.[20], Xiao and Zhu [26] and Wu et al. [21]. Numerical studies by Jones et al. [27] and later, Kinsey and Dumas [28] assessed the feasibility of fully-active turbines. Energy generation efficiencies were found to be comparable to the commonly used horizontal-axis turbines and other alternative forms of cross-flow turbines. Later on, multi-foil tandem systems that harvest the remaining wake energy of the upstream foil were developed with the aim of large scale construction of oscillating-foil turbine farms [29] [30] [31].

However, in the latest *in situ* deployment of oscillating-foil turbine technologies had provided discouraging results. Prototypes by The Engineering Business Ltd [32] and Pulse Tidal Ltd produced sub-par efficiencies. Further developments on these prototypes were economically unsustainable, following with the unfortunate liquidation of Pulse Tidal Ltd and the halt on the Stingray turbine project. Kinsey

et al. [33] performed *in situ* experiments on a dual-hydrofoil turbine. The turbine was able to achieve peak power extraction efficiencies of 30% but it was deemed highly susceptible to losses. The prototype by Kinsey et al. was a one degree of freedom turbine. The one degree of freedom was made possible via a four-link mechanism on each of the heave and pitch motions. The authors estimated that the mechanical loss of the prototype turbine was at least 25% of the total power extracted and was associated with the friction generated from the complex linkage system.

Numerically and experimentally, fully-active oscillating-foil turbines have shown great energy harvesting potential from the surrounding flow. However, the practical implementation of constrained coupling between the heave and pitch motion of the foil requires complex structural design and the need for multiple electrical generators. Not to mention, strictly imposed motion of the foil leads to further friction losses in power and, induced mechanical stresses that occur under unpredictable perturbation and turbulence from incoming currents. Thus, researches have started investigations on the simplification of such constraints, mainly by removing the need for active controls and replacing them with passive systems.

Semi-passive/Fully-passive oscillating-foil turbine

Passive oscillating-foil systems involve the use of passive constraints on any or all degrees of freedom of the foil. Semi-passive oscillating-foils are systems where part of the motion of the foil is actively prescribed and the other is passively constrained. If all degrees of freedom of the foil are passively constrained without the use of any active prescription, the oscillating system is considered to be a fully-passive oscillating-foil. The passive constraints are commonly implemented in the form of stiffness and damping parameters. The adjustment of these stiffness and damping parameters are responded by the change in the amplitudes and frequency of the passive heave and pitch motions of the foil. Here, the motions remain bounded but at the same time, are able to move freely and have unrestricted relative phase lag.

Semi-passive oscillating-foil systems were assessed by several researchers numerically and experimentally. The authors reported reasonable efficiencies in the order of 30% to 40% [34] [35] [36] [37] [38]. Physically, the practical implementation of the semi-passive system would require power input to actively impose one of the degrees of freedom, while disregarding any mechanical coupling or additional motors on the passive degree of freedom, a step forward towards simplicity than the fully-active

systems.

Greater simplification to the oscillating-foil system into a fully-passive system was initially demonstrated by Poirel et al. [39] and followed by Peng and Zhu [40]. The proposed design consist of self-induced evolution of both heave and pitch motions by the interaction between the foil and the flow. Physically, the motions of the foil were constrained elastically by springs and dampers to maintain a self-sustained limit cycle oscillations. A number of other works have focused on studying the structural response and stability analysis of the aeroelastic phenomenon and have determined multiple modes of oscillatory response [40] [41] [42] [43]. Optimal energy harvesting has been linked to one oscillation mode of high amplitude in the heave and pitch motions along with the presence of harmonic wake-body synchronization. Previous research showed that in order to achieve such behaviour, careful selection of structural parameters are required. The seven core structural parameters are listed in the next section.

A fully-passive turbine prototype examined by Boudreau et al. [44] was able to exploit such an operating regime and achieved promising energy extraction efficiency in the order of 30%. The exact prototype was used in the present work and is further described in Section 2.1. Even so, the reported efficiency is still far from the values recorded from numerical predictions, suggesting that precise parameterization and the balance of structural components are difficult and physically laborious. These challenges prompt the need for other means of optimization to reach the goal of practical applications of fully-passive oscillating-foil turbines.

1.3 Optimization of oscillating-foil turbines

Oscillation mode corresponding to motions of large heave and pitch amplitude suits best for energy harvesting applications. In general, the motion of the two degrees of freedom and the synchronization between both can be quantified by four kinematic parameters. The kinematic parameters are heave amplitude, pitch amplitude, oscillation frequency and phase lag. Optimal values of these kinematic parameters was determined by several research groups [28] [35] [38] [45] [46] [47] and can be found well summarized in the review papers by Wu et al. [21], and Xiao and Zhu [26].

In a fully-passive system, the kinematic of the foil is dependent on the structural parameters imposed on the system. They are the seven dimensionless structural parameters $(m_h^*, I_\theta^*, S^*, k_h^*, k_\theta^*, D_h^*, D_\theta^*)$ embedded in the governing equations of motion

of the foil presented in Section 2.1. The manipulation of these structural parameters influences the response of the foil and the resulting limit-cycle oscillation mode. Optimization of these parameters can alter the kinematic parameters to fall within the desired oscillation mode of large heave and pitch amplitude, which is optimal for energy harvesting [40] [41] [42] [43] [46] [48] [49]. The prototype developed by Boudreau et al. [44] used in the present work was based on the numerical optimization of the structural parameters by Veilleux and Dumas [48] [46]. Optimization of such kind deals with preventing the instability of the system, specifically the divergence instability and the flutter instability.

Separating from the fundamental problem of instability in aeroelastic systems, fluid dynamics and fluid-structure interaction in the near vicinity of the foil can also influence the kinematic parameters of the foil. Fluid-structure interactions, such as with the LEV, can transform the surrounding pressure field of the foil and the resulting motion of the foil. It is universally known that all lift-based foil technology suffers from the stall phenomenon. As the angle of attack of the foil increases, LEV grows in size and strength, feeding from the shear layer. The separation of flow occurs when the stagnation point transverses pass the trailing edge of the foil. Here the LEV is shed into the wake and the adverse pressure gradient stabilizes. The foil then stalls and experience a decrease in the dynamic force experienced by the foil [50]. Therefore, clever manipulation of the LEV and the surrounding pressure field can be utilized to delay or, in some cases, entirely prevent the stall phenomenon.

Several researches have investigated several means to alter the flow topography surrounding a foil and control the LEV. Among the studies on foil deformation, Le and Ko [51], and Liu and Xiao [52] considered chordwise flexibility of the foil while Siala and Liburdy [53], and Totpal et al. [54] examined chord actuation of the foil, in which all depend on the similar principle of modifying the effective local angle of attack of the foil. Investigation on certain foil shape configurations ranging from cylinders to flat plates [55], to NACA foils [56] and even interesting geometries of NACA foil hybrids [57], have reported improvement in energy harvesting performance. Zhu et al. [58] and Bouzaher et al. [59] have performed tests on the use of Gurney flaps on the trailing edge of the foils and concluded an increase in lift forces due to the increase in the pressure gradient across the foil. Qadri et al. [60] proposed the use of heave and pitch limiters to indirectly enforce certain heave and pitch kinematics of the foil, preventing dynamic stall.

The physical manipulation of the flow field, although through varying means, all

focuses on certain key principles to hinder the separation of flow and control the LEV. The control of the vortex ensures that the centre of pressure concentrates close to the aerodynamic centre of the foil for an extended period of time, in return providing prolonged lift forces on the foil. The mentioned campaigns, tackling only the flow field in two-dimensions, were successful in this matter. Alternatively, works by Kinsey and Dumas [61] and Kim et al. [62] have looked into the three-dimensional effects of the oscillating-foil turbine and proposed the use of appropriate aspect ratio of the foil and end plates to minimize tip losses. Their work suggested that strategic use of certain three-dimensional effects can also provide a positive contribution to energy harvesting potential, in which prompted the use of spanwise flow component in the present work, to optimize the fully-passive oscillating-foil turbine prototype.

1.4 Spanwise flow component

The vector component of an incident flow onto a leading edge with a sweep angle, Λ can be decomposed into chordwise and spanwise flow components. The chordwise flow component is the flow vector parallel to the chord line, while the spanwise flow is the flow vector perpendicular to the chord line. Both flow components are illustrated in Fig. 1.3 for an infinite-span swept wing. This suggests that the flow structure around a swept wing must be considered in three dimensions.

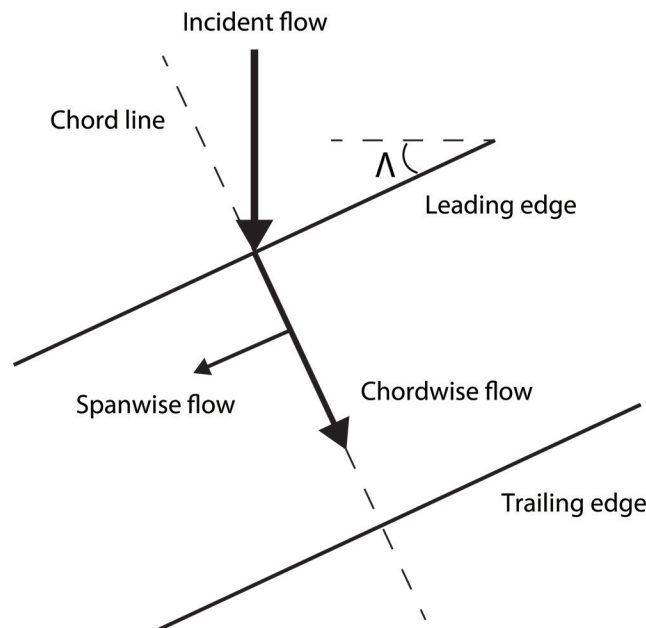


Figure 1.3: Vector components of the flow on the infinite-span swept wing.

Unlike the leading-edge stagnation point in a two-dimensional (2D) flow, a swept wing has a non-zero velocity along the spanwise direction of the leading edge. This creates a leading-edge attachment line instead of a stagnation line along the span of the swept wing. The development of the attachment line boundary layer also differs with the stagnation point boundary layer, where the three-dimensionality of the attachment line boundary layer causes lower surface pressure as compared to the stagnation pressure [63]. The flow field response to these pressure changes is reflected in the flow separation and the formation of the primary LEV.

The notion of spanwise flow component stabilizes the LEV was first proposed by Ellington et al. [64] on their study of LEV on insect flights. Three-dimensional (3D) flow structure similar to the conical LEV on delta wings, was observed on their mechanical hawkmoth wing model. The convection of circulation towards the wing-tip was determined to be the source of stable LEV attachment in the majority of the downstroke motion of the wing. Later on, several other claims on the cause of the stability of LEV has been raised. Birch and Dickinson [65] conducted further studies on LEV attachment on insect wings and have concluded that the downwash near the wing-tip was the more likely source. Lentink and Dickinson [66] through their revolving wings experiments claimed that it was the centripetal acceleration and Coriolis effects that caused stabilization of LEV. Nevertheless, with the increasing investigations on the effects of spanwise flow on wings in the recent years, the general consensus is that spanwise flow does provide a positive contribution to the stability of the LEV attachment [67] [68] [69] [70] [71]. However, spanwise convection of vorticity alone does not ensure stable LEV attachment [72] [73].

The present work is motivated by the spanwise flow study on plates through the use of a sweep profile, conducted by Beem et al. [74]. The study was an actively prescribed heave-only plunging motion of a flat plate, and have reported an absence of LEV stabilization. On the other hand, evidence of the delay of LEV shedding was present when the flat plate was swept. Wong et al. [68] followed up with experimentation on flapping plates with sweep profiles and found evidence on regulation of vortex strength through the spanwise flow. Later, Wong and Rival [71] outlined improved LEV stability in the presence of spanwise vorticity transport. These series of works verified the important notion of LEV stability on the sweep profile of wings and inspired the further study on the three-dimensionality of flow on energy harvesting turbine.

1.5 Objectives

Optimization on the system dynamics via structural alteration of the foil has proven to be effective in optimizing turbine technologies. However, it can be argued that the practical implementation of such methods is specific to controlled scenarios, usually within laboratory settings. From an economical and practical point of view, affordable means of optimization are required to push forward the real-world implementation of the oscillating-foil turbine technology.

The primary objective of this campaign is to optimize the oscillating-plate prototype hydrodynamically, through fluid-structure interactions of the three-dimensional effects. The present work assesses the use of spanwise flow on the optimization of the fully-passive turbine concept demonstrated by Boudreau et al. [44]. The study involves the simple use of a sweep profile on the leading edge that promotes the spanwise flow component along the span of the plate. As an elementary investigation into the spanwise flow on oscillating-foil turbine, the present work studies the use of a flat plate instead of the favoured NACA shaped foil to prevent vortex dynamics stemming from the geometry of the foil. Thus, the secondary objective of this campaign, the evaluation of the distinct influence on the LEV by the spanwise flow, can be better performed.

To the current knowledge of the author, there have been no publications on the direct use of spanwise flow to optimize the performance of oscillating-foil turbines. Considering the use of such optimization method involving unsteady events in three-dimensional space, high fidelity simulation of the 3D flow would be cost and time ineffective. In this aspect, the proposed experimental work adds on to the knowledge gap surrounding 3D flow phenomena of oscillating-foil technologies. Furthermore, most published works on the understanding of the principle of LEV stabilization and spanwise flow were based on settings involving actively-actuated foils. The use of passive scenarios in observing the cause and effect of LEV stabilization via spanwise flow will provide a novel perspective to the field.

Provided the opportunity of a well-built fully-passive turbine prototype by Boudreau et al. [44] and the appropriate visualization means, up to the third dimension, available in the Fluid Mechanic Laboratory, in the University of Victoria, the author has chosen to experimentally study the influence of sweep angle on the LEV and its relation to the power extraction performance of a fully-passive oscillating-plate hydrokinetic turbine prototype.

The author aims to add to the collective effort of oscillating-foil studies, specifically on the subject of the induced vortex. The present work is aspired to contribute to the practical development of oscillating-foil turbines and the eventual large scale applications in the coming time.

1.6 Structure of the thesis

The following chapters start with the description of the governing equations of the oscillating-plate turbine prototype, following up with the experimental setup, the visualization techniques and the results. Finally, the thesis is concluded with a summary of the main results and recommendations for future work. The majority of the thesis is written with the purpose of journal publication, where each chapter would represent a section of the published paper:

Chapter 1 General background of oscillating-foil turbines. Various methods of optimization of the fully-passive oscillating-foil turbine. Objective of the present work.

Chapter 2 Describes the fundamentals of the oscillating-plate turbine prototype and the experimental method.

Chapter 3 Summary of the planar and tomographic Particle Image Velocimetry techniques.

Chapter 4 The power extraction performance of the oscillating-plate turbine prototype between the unswept and swept plates.

Chapter 5 Visualization of the flow field in two-dimension and three-dimension. Estimation of the induced-forces acting on the plate by calculating the moment of vorticity. The three-dimensional study of the vortical structure of the LEV.

Chapter 6 Concluding statements of the proposed results and a list of recommended directions for the future work.

Chapter 2

Experimental system and techniques

2.1 Fully-passive turbine prototype

The fully-passive turbine prototype in the current campaign is the same physical prototype used in the study by Boudreau et al. [44]. For detailed descriptions of the design and calibration of the prototype, the reader is referred to the previous work mentioned. Key parameters relevant to the present work are discussed in the following. An important difference between the present work and the investigation by Boudreau et al. is the cross-sectional and spanwise geometry of the foil. In the current campaign, the NACA 0015 foil was replaced with a flat plate. Moreover, a sweep angle with respect to the direction of the inflow was introduced along the span of the plate. The details of the plate geometry are provided in Section 2.2.

A schematic of the two degrees of freedom oscillating-plate system is shown in Fig. 2.1. The plate of chord length, c was free to move in the heave direction along the y -axis and the pitch direction, about the z -axis. The heave and pitch positions are indicated in Fig. 2.1 as $h(t)$ and $\theta(t)$, respectively. The direction of fluid flow was oriented towards the positive x -direction. The pitching axis was located at distance x_p downstream from the leading edge of the plate and was always parallel to the z -axis, perpendicular to the flow direction. Both the heave and pitch motion were elastically constrained by heave springs of stiffness k_h and pitch springs of stiffness k_θ . Damping in both heave and pitch motions are indicated by D_h and D_θ , respectively.

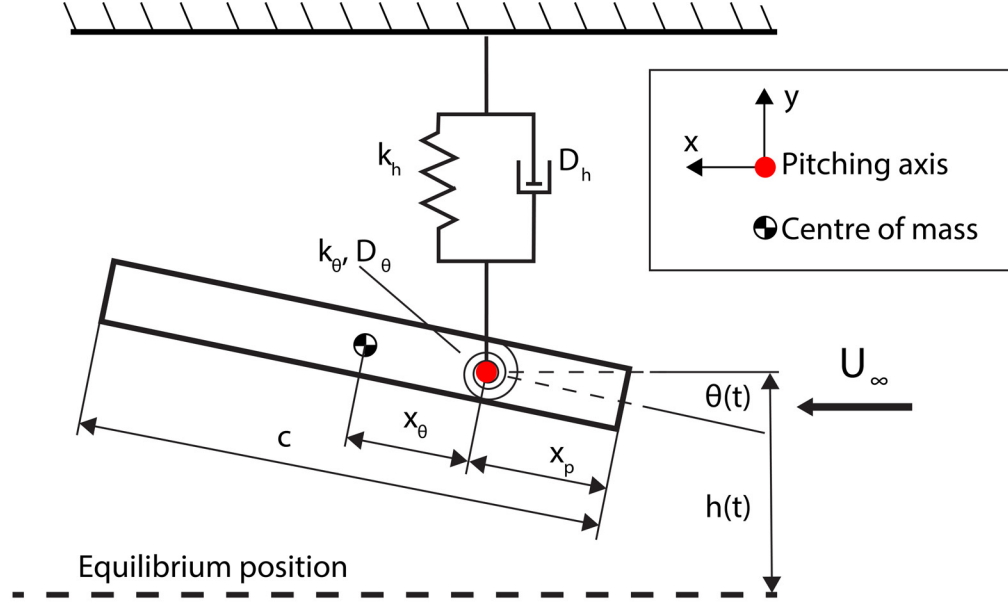


Figure 2.1: Schematic of the passively oscillating-plate.

The dimensionless governing equations for the heaving and pitching motions of the passively oscillating-plate derived using a Lagrange approach presented in the thesis of Veilleux [48], are shown in Eq. 2.1 and Eq. 2.2, respectively. The superscripts (\cdot) and $(\ddot{\cdot})$ denotes the first and the second derivatives with respect to time, respectively.

$$C_{Fy}/2 = m_h^* \ddot{h}^* + S^* (\ddot{\theta}^* \cos\theta - \dot{\theta}^{*2} \sin\theta) + D_h^* \dot{h}^* + k_h^* h^* + C_{Fy} Coulomb/2 \quad (2.1)$$

$$C_M/2 = I_\theta^* \ddot{\theta}^* + S^* \ddot{h}^* \cos\theta + D_\theta^* \dot{\theta}^* + k_\theta^* \theta + C_M Coulomb/2 \quad (2.2)$$

The terms defining Eq. 2.1 and Eq. 2.2 are expanded and shown from Eq. 2.3 to Eq. 2.7. All the variables and terms appearing in the governing equations of motions are listed in Table 2.1, accompanied with their respective descriptions.

$$C_{Fy} = \frac{F_y}{0.5\rho U_\infty^2 bc} \quad C_{Fy} Coulomb = \frac{F_y Coulomb}{0.5\rho U_\infty^2 bc} \quad (2.3)$$

$$C_M = \frac{M}{0.5\rho U_\infty^2 bc} \quad C_M Coulomb = \frac{M_{Coulomb}}{0.5\rho U_\infty^2 bc} \quad (2.4)$$

$$m_h^* = \frac{m_h}{\rho bc} \quad I_\theta^* = \frac{I_\theta}{\rho bc^4} \quad S^* = \frac{S}{\rho bc^3} \quad (2.5)$$

$$k_h^* = \frac{k_h}{\rho U_\infty^2 bc} \quad k_\theta^* = \frac{k_\theta}{r h o U_\infty^2 bc^2} \quad D_h^* = \frac{D_h}{\rho U_\infty^2 bc} \quad D_\theta^* = \frac{D_\theta}{\rho U_\infty^2 bc^3} \quad (2.6)$$

$$h^* = \frac{h}{c} \quad \dot{h}^* = \frac{\dot{h}}{U_\infty} \quad \ddot{h}^* = \frac{\ddot{h}c}{U_\infty^2} \quad \dot{\theta}^* = \frac{\dot{\theta}c}{U_\infty} \quad \ddot{\theta}^* = \frac{\ddot{\theta}c}{U_\infty^2} \quad (2.7)$$

In a given flow, the 9 dimensionless structural parameters that define the two degrees of freedom of motion of the system are:

$$m_h^* \quad I_\theta^* \quad S^* \quad k_h^* \quad k_\theta^* \quad D_h^* \quad D_\theta^* \quad C_{F_y Coulomb} \quad C_{M Coulomb}$$

Naturally, oscillation does not last forever due to the presence of damping. The viscous damping in heave, $D_{h,v}$ and pitch, $D_{\theta,v}$ along with the Coulomb friction in heave, $F_{y Coulomb}$ and pitch $M_{Coulomb}$ in the bearings provide undesired losses in the system. Another additional source of damping in heave was the adjustable eddy-current braking. The eddy-current braking imitates an energy sink, or more specifically the equivalent energy conversion into electricity output for the system. The total linear damping coefficient is then defined as the sum of all sources of damping in as shown in Eq. 2.8 and Eq. 2.9, for the heave and pitch degrees of freedom, respectively. The linear heave damping coefficient was contributed both from the viscous damping and the desired energy sink, while the linear pitch damping coefficient consists only of viscous damping from the bearing. Although, the prototype was equipped with eddy-current braking in the pitch degree of freedom, it was not implemented in any case in the present work.

$$D_h = D_{h,e} + D_{h,v} \quad (2.8)$$

$$D_\theta = D_{\theta,v} \quad (2.9)$$

The energy sink in heave consists of a thin aluminum plate attached to the heave carriage, which travels through a magnetic yoke placed at a determined relative distance. With the knowledge of the heave velocity of the carriage and the calibrated heave damping coefficient of the eddy-current brake [44], the cycle-averaged power dissipated through the eddy-current brake, $\overline{P_{h,ej}}$ can be estimated according to:

Table 2.1: Variables and terms involved in the governing equations of motion. Adapted from [44].

Symbol	Units	Definition
b	$[m]$	True span length
b'	$[m]$	Effective span length ($b \cos \Lambda$)
c	$[m]$	Chord length in the streamwise direction
ρ	$[kgm^{-3}]$	Water density
U_∞	$[ms^{-2}]$	Freestream velocity along the x -axis
h	$[m]$	Heave position of the pitching axis along the y -axis
θ	$[rad]$	Pitch angle (clockwise is positive)
t	$[s]$	Time
x_p	$[m]$	Distance between the leading edge and location of pitching axis
x_θ	$[m]$	Distance between the centre of mass and the location of pitching axis (positive when pitch axis is upstream of the centre of mass)
F_y	$[N]$	Hydrodynamic force component in the heave direction (y -direction)
M	$[N \cdot m]$	Hydrodynamic moment of force component about the pitch axis (z -axis)
$F_{yCoulomb}$	$[N]$	Coulomb friction force component in the heave direction (y -direction)
$M_{Coulomb}$	$[N \cdot m]$	Coulomb friction moment of force component about the pitch axis (z -axis)
m_h	$[kg]$	Mass of all component undergoing heave motion
I_θ	$[kg \cdot m^2]$	Moment of inertia about the pitching axis
S	$[kg \cdot m]$	Static moment (mass of all components undergoing pitching motion times x_θ)
k_h	$[N/m]$	Heave stiffness coefficient
k_θ	$[N \cdot m/rad]$	Pitch stiffness coefficient
D_h	$[N \cdot s/m]$	Total linear heave damping coefficient
$D_{h,e}$	$[N \cdot s/m]$	Linear heave damping coefficient of the eddy-current brake (desired energy sink)
$D_{h,v}$	$[N \cdot s/m]$	Linear heave damping coefficient of the heave bearings
D_θ	$[N \cdot s \cdot m/rad]$	Linear pitch damping coefficient of the pitch bearings

$$\overline{P_{h,ej}} = \frac{1}{T_j} \int_t^{t+T_j} (D_{h,e} \dot{h}^2) dt \quad (2.10)$$

where T is the oscillation period and the subscript j denotes values from a j th cycle. The two essential performance parameters used in evaluating energy extraction performance, the efficiency η_e and the power coefficient in heave $C_{P_{h,e}}$, are defined from the cycle-averaged dissipated power as follows:

$$\eta_{e j} = \frac{\overline{P_{h, ej}}}{0.5 \rho U_\infty^3 b' d_j} \quad (2.11)$$

$$\overline{C_{p_{h,e} j}} = \eta_{e j} \frac{d_j}{c} \quad (2.12)$$

where d_j is the heave distance (between the extrema) of the plate during a j th cycle. The efficiency is the ratio between the power extracted by the turbine and the total available power across the entire extraction window, defined by the heaved area of the plate. The power coefficient is the ratio between the power extracted by the turbine and the total available power across the surface area of the plate.

The motion of the plate undergoing oscillation are evaluated using the kinematic parameters. These parameters denote the reduced frequency of the oscillation, the phase lag between the heave and pitch motions, the heave amplitude, and the pitch amplitude of the plate. The kinematic parameters are indicated in Eq. 2.13 to Eq. 2.16 as f_j^* , ϕ , H_0^* and θ_0^* , respectively.

$$f_j^* = \frac{f_j c}{U_\infty} \quad (2.13)$$

$$\phi_j = \frac{360^\circ}{T_j} (t_{\theta_{max j}} - t_{h_{max j}}) \quad (2.14)$$

$$H_0^* j = \frac{h_{max j} - h_{min j}}{2c} \quad (2.15)$$

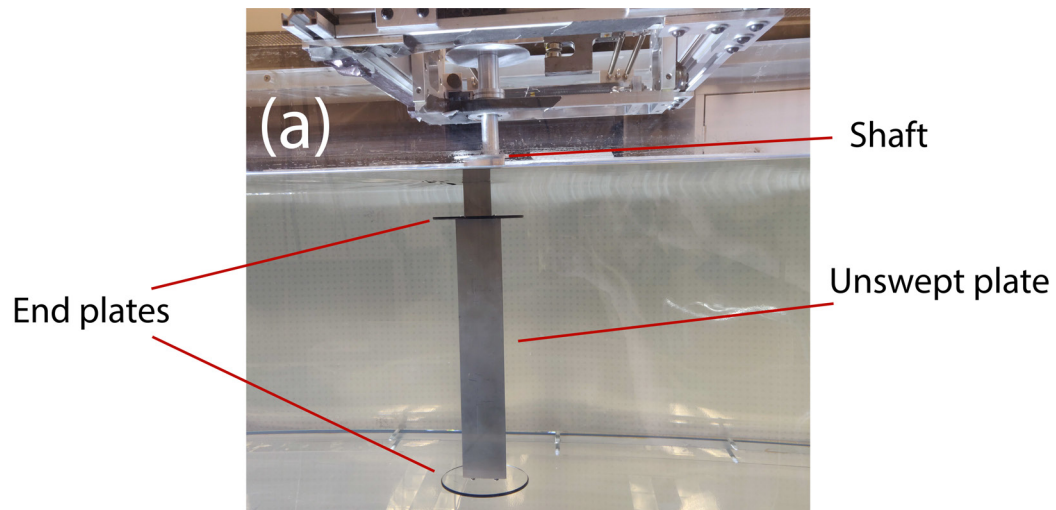
$$\theta_{0j} = \frac{\theta_{max j} - \theta_{min j}}{2} \quad (2.16)$$

All corresponding values of the kinematic and performance parameters presented in Section 4 were averaged over 90 oscillations. It is important to note that the true

span length, b was kept constant for all plates and was used to evaluate the normalized structural parameters of the system, such as the ones shown in Eq. 2.3 and Eq. 2.6. However, performance parameters, such as the ones shown in Eq. 2.11 and Eq. 2.12 were directly related to the transfer of hydrodynamic forces by the flow on to the extraction window and surface area of the plate. Thus, it is evaluated by the effective span length, b' . These span length components are demonstrated in Fig. 2.3.

2.2 Experimental setup

All experiments were conducted in the Fluid Mechanics Laboratory water channel at the University of Victoria. The water channel had a cross-sectional dimension of 0.45 m by 0.45 m and a length of 2.5 m. The only component of the fully-passive turbine prototype interacting with the flow of fluid was the plate, as shown in Fig. 2.2(a). All other components of the prototype were placed above the water level, in which were laid on the walls of the channel. The components that characterize the structural parameters are presented in Fig. 2.2(b). The water level height at rest was set to 0.37 m and the plates were positioned to be 50 mm under the free surface, of which the shaft protrudes.



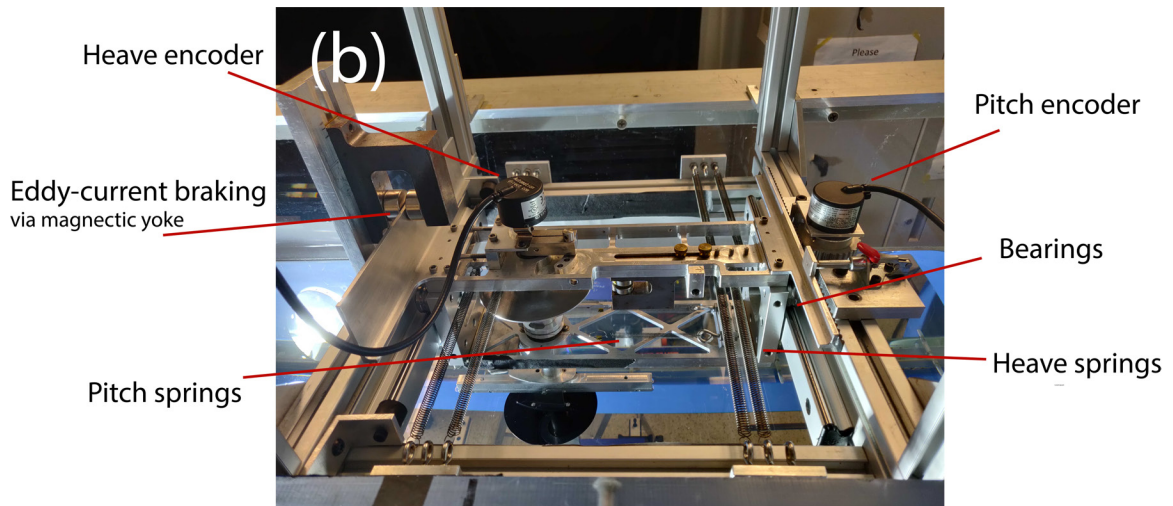


Figure 2.2: The setup of the fully-passive turbine prototype on the water channel.

Two stainless-steel plates were used in this campaign: a flat plate with the leading edge parallel to the pitching axis (unswept) and a flat plate with a sweep angle, $\Lambda = 6^\circ$ between the leading edge line and z -axis. Going forward, the unswept flat plate and flat plate with the sweep profile will be referred to as unswept plate and swept plate, respectively. A schematic of the unswept and swept plates in the side view is shown in Fig 2.3. Both plates had the same thickness of 5 mm and streamwise chord length of $c = 50$ mm. The true span length of both plates were $b = 300$ mm. $\Lambda = 6^\circ$ was chosen because it corresponds to an effective span length difference, $(b - b')/b$ and effective chord length difference $(c - c')/c$ of about 1% as compared to their respective true lengths. This sweep angle ensures that the aspect ratios and geometric features between the unswept and swept plates were consistent and comparable between each other.

The centre of mass of the plates were located at the mid span and at the mid chord point, $x_p/c = 1/2$ from the leading edge. The pitching axis location of the unswept plate was placed at $x_p/c = 1/3$ from the leading edge, equivalently $x_\theta/c = 1/6$ upstream from the centre of mass, as it is indicated in Fig. 2.3. The third-chord point ($x_p/c = 1/3$) is the preferred location for the pitching axis in many pitching foil applications [28], because it places the aerodynamic centre closer to the centre of pressure, a location where the force vector of the total sum of a pressure field acts upon. As it is shown in Fig. 2.3, x_p along the span was constant for the unswept plate but this was not the case for the swept plate. The dissimilarity in the position of x_p causes a difference in fluid dynamic forces on the plate, however, was managed

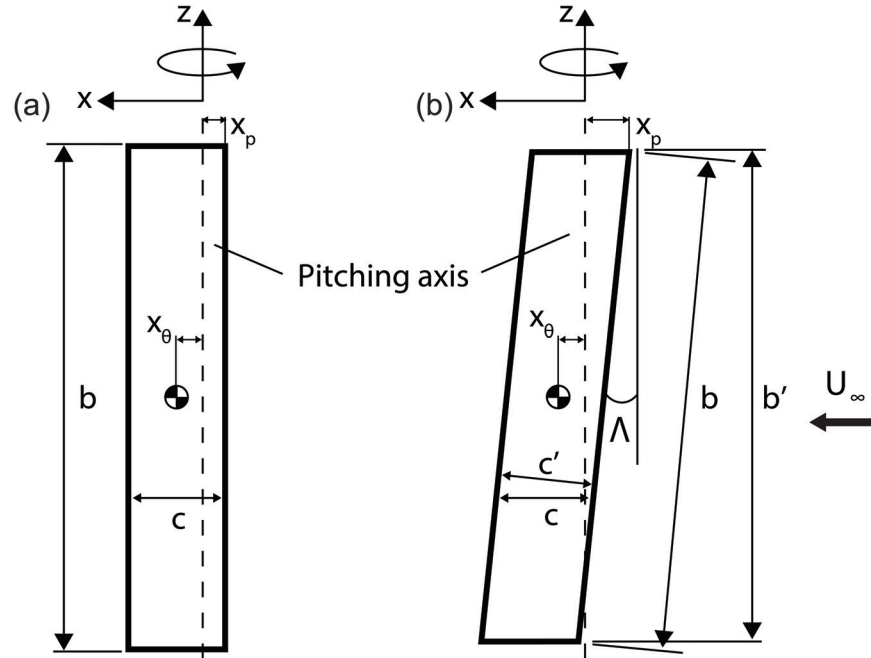


Figure 2.3: Schematic of the unswept plate (a) and the swept plate (b) in the side view.

in the broader sense by positioning the location of the pitching axis of the swept plate at $x_\theta/c = 1/6$ upstream from the centre of mass. The positions of x_θ were the same between the two plates.

Circular endplates were attached at both tips of the plate to minimize the influence from the free surface of the water and tip losses. The size of the endplates were $0.5c$ from the leading edge and trailing edge of the plate to the filleted edge of the endplates, which is an efficient size recommended by Kim et al. [62] at minimizing tip losses. This corresponded to an endplate with a diameter of $2c$ mounted at the mid chord point, at each end of the plate. The endplates were made of Lexan polycarbonate and had a thickness of $0.06c$. The material was transparent to allow light to pass, which enabled the visualization of flow fields in the vicinity of the plates, with the endplates remain attached.

2.3 Experimental techniques

The reader is recommended to refer to the measurement protocol of the experiments and data collection described by Boudreau et al. [44]. Essential and contrasting points will be stated in this section out of necessity.

The frictional damping from the bearing alters with time due to wear. To account for the changes, the different frictional contributions in heave and pitch were estimated before and after conducting each series of experiments. The estimated viscous damping and Coulomb friction values ($D_{h,v}^*$, D_{θ}^* , $C_{FyCoulomb}$ and $C_{MCoulomb}$) of each test are given below. The reader is directed to the publication by Boudreau et al. [44] for the methodology that was used to estimate these frictional contribution values.

The position in heave and pitching angles of the plates were recorded with two rotary encoders, for roughly 100 oscillations. The encoders had a sampling frequency of 1147.7 Hz. The digital signals were converted into 0 – 5 v analog signals which were then read by the NI USB-6218 data acquisition board connected to a laptop.

The inflow freestream velocity was measured using Particle Image Velocimetry (PIV) at 12.95 Hz at the location upstream of the plate. The inflow freestream velocity was estimated by averaging 200 instantaneous velocity fields. The standard deviation across the mean streamwise velocity field was computed to be less than 0.1%, signifying the uniformity of the inflow. The turbulence intensity of the streamwise velocity fluctuations was calculated to be 1% and less.

Temperatures of the water surface and the aluminium sliding plate were measured using an IR thermometer. The water surface temperature was assumed to be the bulk water temperature and was used in determining the water properties to compute the structural and performance parameters. The calibrated heave damping coefficient of the eddy-current brake [44] was corrected for temperature difference based on the recorded temperature of the aluminium sliding plate.

Chapter 3

Quantitative flow imaging

Particle Image Velocimetry (PIV) was employed several instances in this campaign in the measurement of inflow freestream velocity and two-dimensional wake and three-dimensional vortex structures. The flow was seeded with silver coated hollow glass spheres with a mean diameter of $10\ \mu\text{m}$ and was illuminated by the Quantel Evergreen Nd:YAG 532 nm wavelength dual pulsed laser. Davis LaVision 10.0.5 software was utilized for raw image acquisition and final vector field calculation. A schematic of the PIV setup in the Fluid Mechanic Laboratory is presented in Fig. 3.1. Two types of PIV techniques were carried out in this campaign: Planar (2D) PIV and Tomographic (3D) PIV. The focus of each type of PIV technique is unique, depending on the field of view and resolution that each PIV can provide, and is further described in Section 3.1 and Section 3.2 below. The spanwise locations of the data acquisition plane (DAP) and data acquisition volume (DAV) are denoted by the normalized span, $z^* = z/b'$ where the upper and bottom tip of the plate corresponds to $z^* = 0$ and $z^* = 1$, respectively.

3.1 Planar (2D) Particle Image Velocimetry

The Planar (2D) PIV was used to observe the wake structure of the oscillating-plate. The wide field of view offered here enabled the capture of the initial growth of the LEV and its subsequent shedding into the wake. The 2D PIV field of view was illuminated by expanding the laser beam into a planar sheet with diverging lenses. The field of view was captured with a single camera, LaVision XS 6M camera, labelled *C1* in Fig. 3.1, placed at the bottom of the channel. Camera *C1* was equipped with

a 24 mm focal length lens. The field of view of the raw image capture was 235 mm by 185 mm and had a resolution of 2752×2200 pixels, in the x - and y -axis, respectively. Image acquisition was triggered by the data acquisition board when the plate reached a predetermined heave location recorded by the heave rotary encoder. The heave locations correspond to specific phases of the plate oscillation. Due to the passive nature of the system, slight phase variation was expected to arise from the fluctuating heave velocity of the plate at any given instance of the image acquisition trigger. However, the variations were assumed to be small enough to be accounted for by the ensemble averaging of a set number of flow fields. 300 instantaneous velocity fields were used in the ensemble averaging at the same phase of the plate oscillation to obtain the phase-averaged distribution of the flow velocity. The number of averages used was determined by checking the convergence of Eq. 5.1, where the approach is further explained in Appendix A. An initial interrogation window of 64×64 pixels to a final pass of 32×32 pixels with 75% overlap of the neighbouring interrogation windows was applied in the multi-pass vector calculation process [75]. The final PIV results had a spatial resolution of 0.69 mm/vector. The spatial domain of the out-of-plane vorticity fields shown in Section 5.1 spanned 170 mm by 180 mm in the x - and y -axis, respectively.

3.2 Tomographic (3D) Particle Image Velocimetry

The Tomographic (3D) PIV provides measurements of the flow velocity in a three-dimensional volume. This technique is useful in observing the spanwise variation of a given vortex structure. The 3D PIV setup consisted of a total of three cameras: camera $C1$ (similarly set up as in the 2D PIV), and two additional LaVision Imager Intense cameras, labelled $C2$ and $C3$ in Fig. 3.1. Camera $C1$ was equipped with a 24 mm focal length lens. Camera $C2$ and $C3$ were equipped with 28 mm focal length lens, each. The three cameras were placed in a linear configuration perpendicular to the streamwise flow [76] [77]. The aperture angle, β was adjusted to 54° , which was within the suggested range of aperture angle, $20^\circ < \beta < 60^\circ$ [77] [78] for optimal volumetric reconstruction quality. The laser sheet thickness was expanded into a volume with a thickness of $z = 30$ mm by adjusting the divergent sheet optics and divergent lenses attached at the head of the laser.

Similar to the 2D PIV setup, the images were captured when the data acquisition board was triggered by the heave rotary encoder. Slight phase variation in

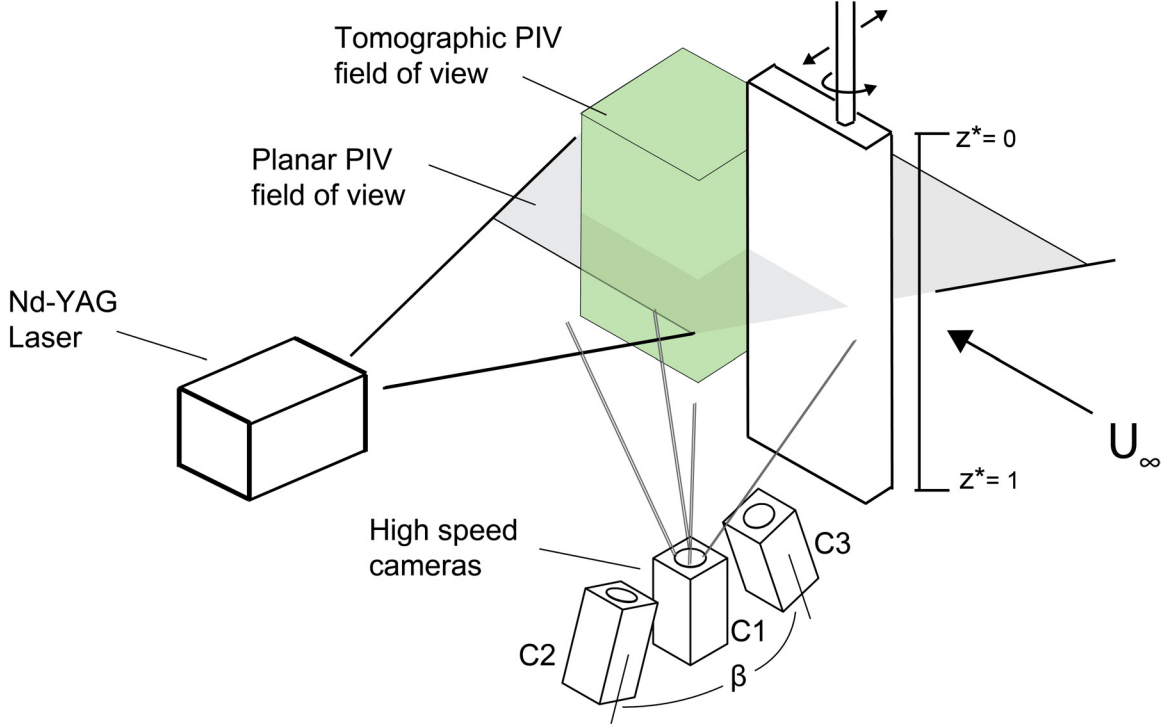


Figure 3.1: Schematic of the Particle Image Velocimetry setup.

the acquired images, as explained in Section 3.1, was expected. The variations were accounted for by the phase-averaging of a set number of flow fields. The seeded particle density across all cameras was estimated to be 0.045 particles per pixel (ppp), which was within a reasonable range of the recommended optimal density at 0.055 ppp [77] [78]. Raw data were first pre-processed to remove background intensity and noise by subtracting the local minimum from each pixel over 3×3 pixel region. Next, particle intensities differences stemming from inhomogeneous laser illumination were normalized over 150 pixels local average. Sliding Gaussian smoothing of 1.5 pixels were applied to improve the particles in the images. Volume self-calibration was performed three times to reduce the initial calibration disparity to an average of 0.02 voxels [79].

The resulting field of view spanned 121 mm by 168 mm by 30 mm with a resolution of $2137 \times 2968 \times 530$ pixels, on the x -, y - and z -axis respectively. Volume reconstruction was performed using 6 multiplicative algebraic reconstruction technique (MART) algorithm iterations [80]. Multi-pass 3D vector calculation of 8 passes was executed with an initial interrogation volume of $96 \times 96 \times 96$ voxels to $32 \times 32 \times 32$ voxels at 75% overlap of the interrogation windows and the vector grid spacing [79].

A $3 \times 3 \times 3$ polynomial smoothing was applied between each step of the correlation. The final vector field of the reconstructed volume, which required an average processing time of 8.5 minutes for each velocity volume, had a spatial resolution of 0.45 mm/vector. The 3D phase-averaged distribution of the flow velocity was obtained by ensemble averaging of 250 instantaneous velocity fields at the same phase of the plate oscillation. The phase-averaged velocity gradients which were susceptible to greater noise were further smoothed with a $3 \times 3 \times 3$ spatial filter. The smoothing process was iterated 10 times. After considering the loss of quality at the edge of the reconstructed volume, the volume of interest (VOI) of all presented 3D flow field results in the present work had a reduced thickness of 22 mm (instead of the illuminated thickness of 30mm). Additional details on the selection of the VOI and the assessment of the tomographic PIV data quality are provided in Appendix B.1. The final 3D PIV results shown in Section 5.3 spanned 80 mm by 110 mm by 22 mm in the x -, y - and z -axis, respectively.

Chapter 4

Hydrokinetic performance of the oscillating-foil turbine

4.1 Baseline case of the unswept oscillating-plate

The baseline case for the unswept plate was selected from a series of preliminary test performed at Re 19 000. The case chosen was a consistent, reliable, high achieving energy extraction case in terms of both efficiency and power coefficient for the unswept plate. The normalized structural parameters governing this case are listed in Table 4.1. Since the streamwise chord and true span of both plates were similar, the normalized structural parameter: k_h^* , k_θ^* and $D_{h,e}^*$ remained consistent between the plates at a given Re number. The only difference within the normalized structural parameters between the separate plates was the total heaving mass, m_h^* moment of inertia, I_θ^* and static moment, S^* of the system, which was inevitable when introducing two plates of varying geometry. The total volume of each plate did not change significantly due to the small sweep angle, resulting in minimal changes in m_h^* . However, a more prominent difference was observed for I_θ^* and S^* and was due to the sweep angle distributing mass further away from the pitching axis.

The values of the structural parameters and those of the normalized structural parameters are of separate values. For example: k_h is a structural parameter and k_h^* is a normalized structural parameter. The entirety of the following experiments measuring the performance of the two plates were executed with the structural parameters (k_h , k_θ and $D_{h,e}$) set constant. The variable parameters in the entire campaign were: the inflow velocity, the sweep angle of the plate and the presence of endplates. The

Table 4.1: The normalized structural parameters of the unswept plate at the baseline case.

Normalized structural parameter	\wedge [°]		
	0	6	
m_h^*	4.26	4.25	± 0.05
I_θ^*	0.323	0.350	± 0.003
S^*	0.113	0.105	± 0.001
k_h^*		3.43	± 0.02
k_θ^*		0.209	± 0.002
$D_{h,e}^*$		0.88	± 0.03
Re		19 000	

impact of these variable parameters on the energy extraction performance will be discussed in the next section. The normalized structural parameters vary with inflow velocity, U_∞ as defined in Eq. 2.5 and Eq. 2.6. Since, the structural parameters were selected based only on the baseline case, the normalized structural parameters were then structurally optimized only for the baseline case. Therefore, the impacts of the kinematic and performance matrices in relation to varying velocities were resulted from the non-constant normalized structural parameters. It is then important to note that the discussions of the following results focus on the result trends corresponding to the two separate plates, rather than the individual trend of each plate.

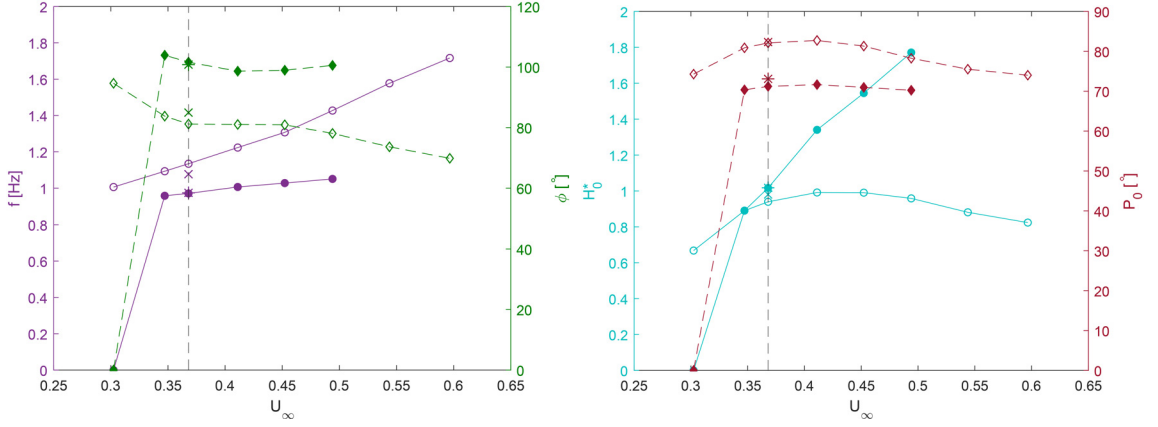
4.2 Effects of the inflow velocity on the turbine performance

The variable parameter of the presented results in this section is the inflow velocity, U_∞ . The inflow velocity range considered here is from 0.3 m/s to 0.6 m/s, which corresponds to the range of Reynolds numbers from Re 15 000 to Re 30 000. The effective flow velocity in chordwise direction of the plate is a function of the incoming inflow velocity and has a magnitude of $U_\infty \cos(\wedge)$. Figure 4.1 shows the effect of the inflow velocity on the turbine performance and kinematic parameters (normalized heave amplitude, pitch amplitude, oscillation frequency and phase lag). All structural parameters were kept constant with reference to the normalized structural parameters baseline values mentioned in Section 4.1. Additional data points (marked \times and $*$

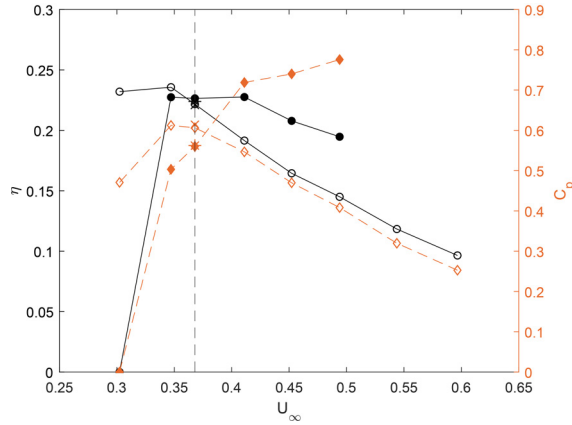
for the unswept plate and swept plate respectively) of equivalent baseline cases from Appendix D was also included to demonstrate the repeatability of the results. The standard deviations of all the kinematic and performance parameters of both plates reported in this section are summarized in Appendix E.

Starting from the low inflow velocity at $U_\infty = 0.3$ m/s, the unswept plate was able to achieve sustainable oscillation, but the swept plate was not. As the velocity was increased to 0.35 m/s, the swept plate was also able to oscillate. It is suggested that the observed increase in the minimum threshold inflow velocity required to establish self-sustained oscillations in the case of the swept plate was due to the combination of a larger moment of inertia and a reduced effective inflow velocity (by a factor of $\cos \Lambda$) relative to the case of the unswept plate. At $U_\infty = 0.35$ m/s, the unswept plate produced a maximum efficiency and power coefficient of $\eta = 23.6$ % and $C_p = 0.61$. Both efficiency and power coefficient decreased with increasing inflow velocities of 0.37 m/s and above. The swept plate on the other hand achieved a maximum efficiency of $\eta = 22.7$ % at $U_\infty = 0.35$ m/s. The relatively constant efficiency values persisted until $U_\infty = 0.41$ m/s and then proceeded to drop for higher inflow velocity values. In contrast to the case of the unswept plate, the power coefficient of the swept plate increased with inflow velocity and reached a maximum of $C_p = 0.78$ at $U_\infty = 0.50$ m/s.

These results suggest a sensitivity to the natural frequency of the heaving and pitching motions of the plates with respect to the oscillation frequency. The natural frequency of the two degrees of freedom can be represented by the reduced heave natural frequency ($f_{n,h}^* = \sqrt{k_h^*/m_h^*}/2\pi$) and the reduced pitch natural frequency ($f_{n,\theta}^* = \sqrt{k_\theta^*/I_\theta^*}/2\pi$). The reduced frequency, reduced heave natural frequency and reduced pitch natural frequency as a function of inflow velocity of both plates are plotted in Fig. 4.2. The points of the high efficiency for both plates correspond to the points where the reduced frequency stayed within close proximity to the reduced heave and the pitch natural frequency. As the reduced frequency deviated far from the reduced natural heave and pitch frequency values shown in Fig. 4.2(a), a decline in efficiency was observed in Fig. 4.1(c). The deviation of the natural frequencies are indications of the poor synchronization between the heave force and heave velocity, resulting in poor energy extraction performance [81]. The phase lag between the heaving and pitching motion also diverged from the optimal value of 90° [28] when the reduced frequency of the system intersected the heave natural frequency, leading to the increase in oscillation frequency shown in Fig. 4.1(a) and the decrease in heave



(a) Frequency (solid purple) and phase lag (dashed green) (b) Normalized heave amplitude (solid cyan) and pitch amplitude (dashed red)



(c) Efficiency (solid black) and power coefficient (dashed orange)

Figure 4.1: Turbine performance and kinematic parameters functions of inflow velocity (U_∞). Open symbols (\circ) represent results of the unswept plate ($\Lambda = 0^\circ$) and filled symbols (\bullet) represent results of the swept plate ($\Lambda = 6^\circ$). The initial and final viscous damping and coulomb friction of each series of test were: $D_{h,v}^* = [0.09 - 0.11]$; $D_\theta^* = [0.007 - 0.007]$; $C_{Fy Coulomb} = [0.01 - 0.04]$; $C_{M Coulomb} = [0.006 - 0.006]$ and $D_{h,v}^* = [0.09 - 0.10]$; $D_\theta^* = [0.007 - 0.007]$; $C_{Fy Coulomb} = [0.02 - 0.01]$; $C_{M Coulomb} = [0.006 - 0.006]$ for the unswept plate and swept plate, respectively. The vertical dashed line corresponds to the baseline case.

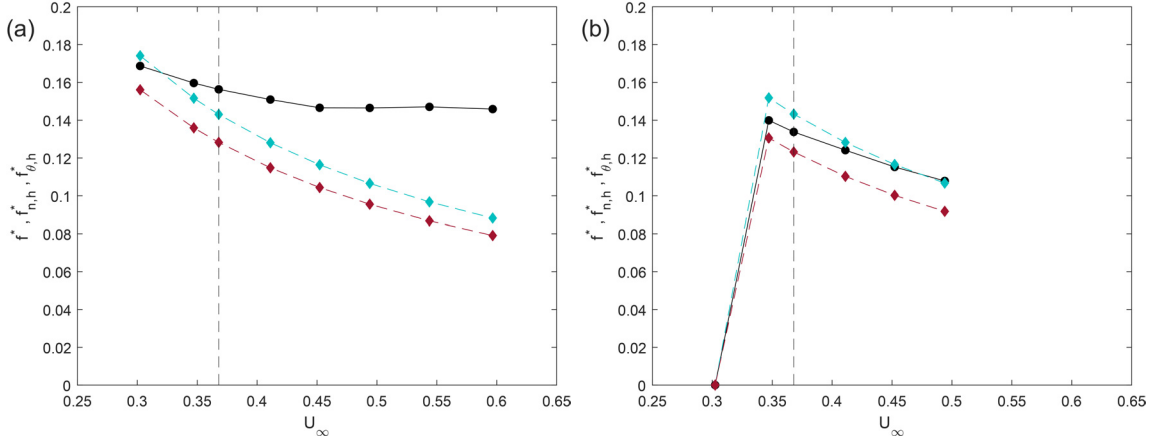


Figure 4.2: Reduced frequency (solid black), reduced heave natural frequency (dashed blue) and reduced pitch natural frequency (dashed red) as a function of the inflow velocity (U_∞) for the unswept plate ($\Lambda = 0^\circ$) (a) and the swept plate ($\Lambda = 6^\circ$) (b).

amplitude shown in Fig. 4.1(b).

In the case of the swept plate, when the values of natural frequency coincided with the reduced heave natural frequency in Fig. 4.2(b), large amplitudes in the heave motion occurred, as shown in Fig. 4.1(b). The increase in heave amplitude at higher inflow velocities is correlated with the large power coefficient values in Fig. 4.1(c). These observations in the present work are in agreement with the findings from the previous campaign by Boudreau et al. [44] where maximum efficiency and power coefficient values of the oscillating-foil turbine were achieved when the reduced frequency and heave natural frequency matched. However, large heave amplitudes of $H_0^* > 1.3$ reduced the efficiency as the angle of attack decreased at certain phases of the oscillation with increasing swept area [26]. Furthermore, as the extraction window increases, power extraction of the turbine could not keep up with the increasing flux of kinetic energy passing through the extraction window, leading to lower efficiency. At higher inflow velocities, the swept plate arrived at the design constraint of the turbine prototype at $H_0^* = 1.8$, which was confined within the walls of the water channel. Thus, the inflow velocity in the case of the swept plate were limited to $U_\infty \leq 0.50$ m/s.

The swept plate obtained consistent efficiency values throughout the tested velocity range and high power coefficient values at higher inflow velocities. The phase lag remained unchanged in the range of 100° . This phase lag corresponds to the range of optimal value for high efficiency cases reported by Boudreau et al. on semi-passive [38] and oscillating foil propulsion systems [82]. The reduced frequency for all cases

of the swept plate also fell well within the optimal range of $f^* = 0.1 \sim 0.15$ suggested by Zhu [45] and, Xiao and Zhu [26] for energy harvesting oscillating foils.

According to the results, it can be concluded that the energy harvesting performance of the swept plate was consistent over a wider range of velocities. This finding indicates that the operation of the swept plate turbine will not be affected by non-uniform inflow velocities that are frequently present in streams and tidal currents. The swept angle is an important construction parameter that should be considered in any energy harvesting oscillating-foil turbines.

Chapter 5

Quantitative flow patterns

5.1 Two-dimensional flow patterns

The out-of-plane vorticity fields in the vicinity of the plates and in the wake were obtained using the PIV technique at the single value of the inflow velocity $U_\infty = 0.41$ m/s. The chosen inflow velocity here correspond to the point where differences in the kinematic and performance matrices become prominent between the cases of the unswept plate and swept plate. The vorticity field was used to provide insights into the relation between the kinematics of the plate motion and the energy extraction performance of the two plates under consideration by studying the space-time evolution of the shed vortices. The location of the 2D PIV DAP along the z -axis can be identified via the normalized span, $z^* = z/b'$ where the upper and bottom tip of the plate is $z^* = 0$ and $z^* = 1$ respectively, as presented in Fig. 3.1. Since the vortical structures in the case of the unswept plate were symmetric with respect to the midspan plane $z^* = 0.5$ [61] [83], PIV data were acquired only at the midspan plane for the unswept plate. Figure 5.1 shows the phase-averaged out-of-plane dimensionless vorticity field for the unswept plate at $z^* = 0.5$. Two vorticity fields at $z^* = 0.5$ and $z^* = 0.88$ were considered in the case of the swept plate to observe the effects to spanwise vorticity transport at different depth. Figure 5.2 and Fig. 5.3 shows the phase-averaged out-of-plane dimensionless vorticity field for swept plate at $z^* = 0.5$ and $z^* = 0.88$, respectively. The origins of the x - and y -axis correspond to the location of the pitching axis when the plate is at rest ($h/c = 0$).

Since the motion of the plate was symmetrical for the first-half and second-half of the oscillation cycle, the vorticity patterns corresponding to the oscillation cycle

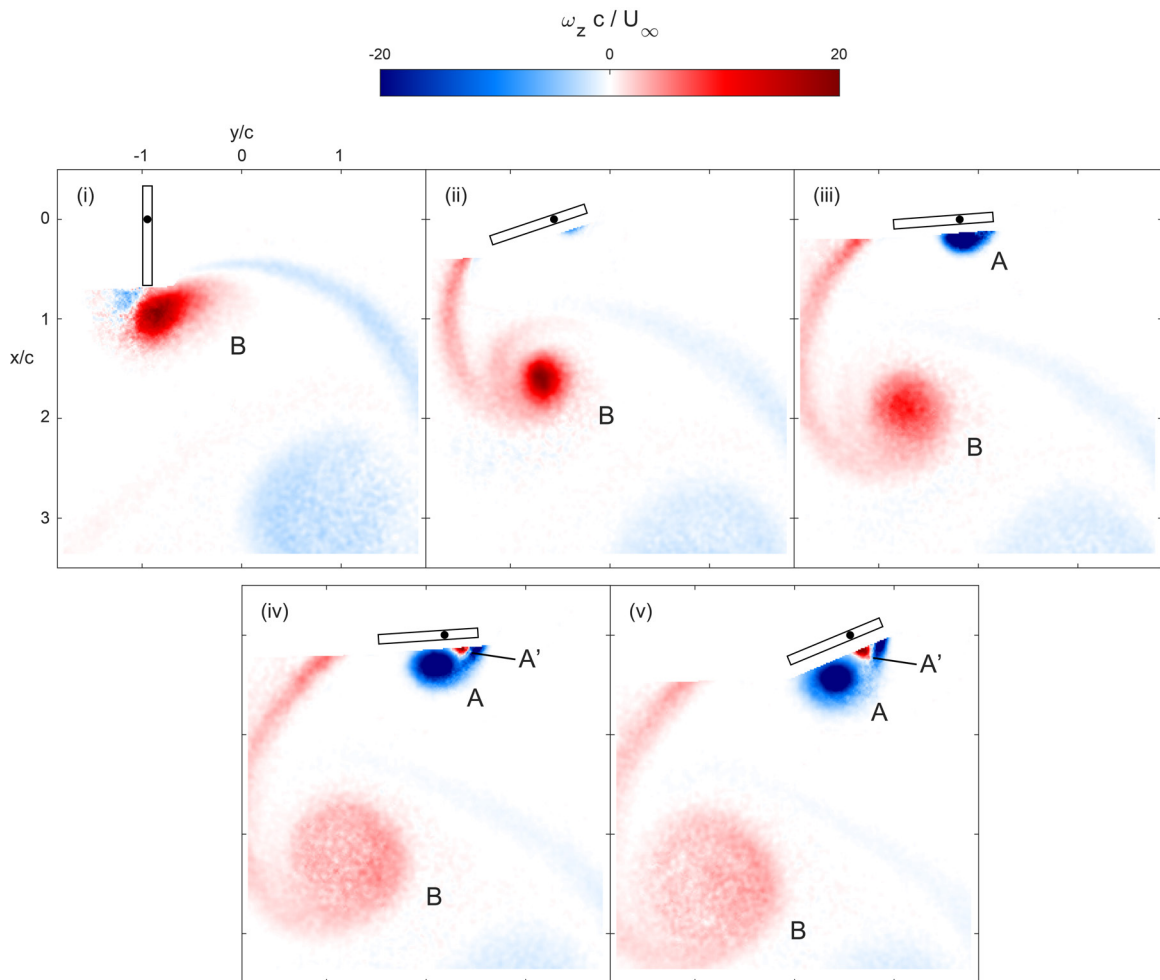


Figure 5.1: Phase-averaged out-of-plane dimensionless vorticity fields at sequential phases $t^* = 0/10$ (i), $1/10$ (ii), $2/10$ (iii), $3/10$ (iv) and $4/10$ (v) for the unswept plate ($\Lambda = 0^\circ$) at $z^* = 0.5$. The filled symbol (\bullet) corresponds to the location of the pitching axis. The flow velocity $U_\infty = 0.41$ m/s was directed from top to bottom.

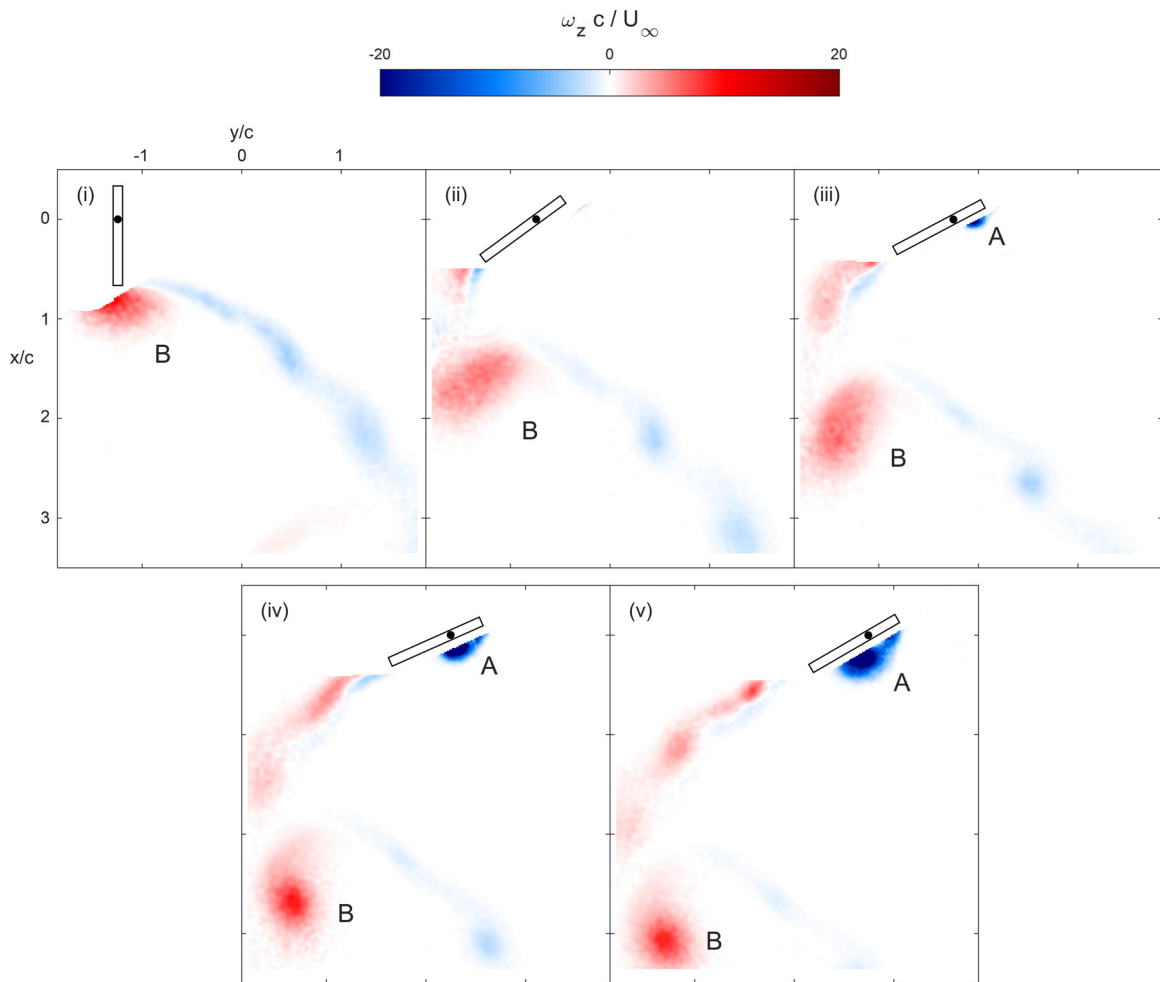


Figure 5.2: Phase-averaged out-of-plane dimensionless vorticity fields at sequential phases $t^* = 0/10$ (i), $1/10$ (ii), $2/10$ (iii), $3/10$ (iv) and $4/10$ (v) for the swept plate ($\Lambda = 6^\circ$) at $z^* = 0.5$. The filled symbol (\bullet) corresponds to the location of the pitching axis. The flow velocity $U_\infty = 0.41$ m/s was directed from top to bottom.

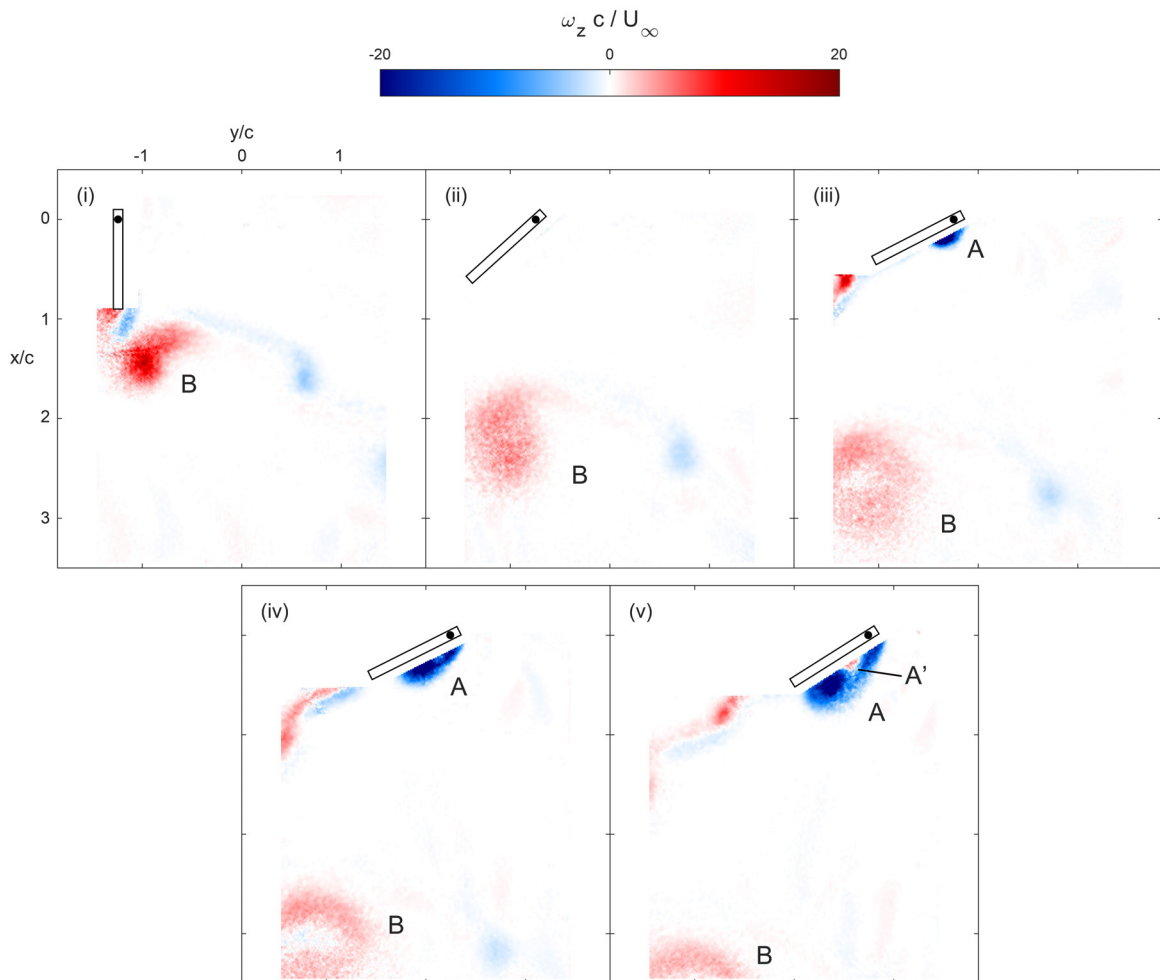


Figure 5.3: Phase-averaged out-of-plane dimensionless vorticity fields at sequential phases, $t^* = 0/10$ (i), $1/10$ (ii), $2/10$ (iii), $3/10$ (iv) and $4/10$ (v) for the swept plate ($\Lambda = 6^\circ$) at $z^* = 0.88$. The filled symbol (\bullet) corresponds to the location of the pitching axis. The flow velocity $U_\infty = 0.41$ m/s was directed from top to bottom.

were essentially identical, but opposite in sign. The first-half of the oscillation cycle is presented in the phase-averaged vorticity fields within five sequential phases $t^* = 0/10, 1/10, 2/10, 3/10$ and $4/10$. The following discussion focuses on the evolution of the LEV in a complete oscillation cycle, starting from its formation at the leading edge to the shedding.

The initial formation of the LEV within the boundary layer could not be visualized at the phases $t^* = 0/10$ and $1/10$ due to the light reflection from the plate surface and the limited spatial resolution. At phase, $t^* = 2/10$, the negative clockwise-rotating LEV, labelled A , was formed for all considered cases. In all considered cases, the boundary layer at this phase was still attached. The vortex A on the unswept plate, shown in Fig. 5.1(ii) was more developed than the LEV on the swept plate in Fig. 5.2(ii) and Fig. 5.3(ii), both in size and in magnitude. The more developed vortex in the case of the unswept plate created a larger local pressure difference between the two sides of the plate, leading to large pitch angles at the current phase $t^* = 2/10$ and $t^* = 3/10$ seen in Fig. 5.1(iii) and Fig. 5.1(iv).

At phase $t^* = 3/10$, the circulation of the vortex A further increased in all considered cases. The vortex A of the unswept plate grew faster than the vortex A corresponding to the swept plate. Dynamic pitching at large angles achieved by the unswept plate led to the formation of a secondary vortex, indicated by the region of positive vorticity between the vortex A and the surface of the plate. The secondary vortex is labelled as A' in Fig. 5.1(iv). According to Doligalski et al. [84], the formation of the secondary vortex corresponds to shedding of the primary LEV, which initiates the stall phenomenon. The following phase of the oscillation cycle at $t^* = 4/10$ in Fig. 5.1(v), shows the unswept plate undergoing deep stall and the subsequent stroke reversal, which results in decreased heave amplitude and power extraction performance (Fig. 4.1).

In the case of the swept plate, the growth of vortex A in size, along the span of the plate was slower than the case of the unswept plate. The spanwise transport of vorticity inhibited local growth of vortex A , especially at the upper-half span of the swept plate. High concentration of vorticity near the bottom tip of the plate at $z^* = 0.88$, promoted the growth of vortex A in Fig. 5.3, but not to the extent shown in case of the unswept plate in Fig. 5.1. The shedding of the vortex A of the swept plate at $z^* = 0.88$ occurred later in the cycle at $t^* = 4/10$ (Fig. 5.3(v)) as compared to the unswept plate, in which the LEV was shed at $t^* = 3/10$ (Fig. 5.1(iv)). However, this trend was observed only at the spanwise location $z^* = 0.88$ in the case of the

swept plate. The secondary vortex was not observed at $z^* = 0.5$, indicating that the shedding of the vortex A did not occur. The difference in LEV shedding at different spanwise location denotes that the growth of the LEV was not uniform along the span of the swept plate. This observation also suggests that the LEV at the upper portion of the span remained attached during the entire period of the oscillation. This finding matches the description by Picard-Deland et al. [81] and Boudreau et al. [49], who reported that highest efficiency values were obtained when the boundary layer remained attached. The attached LEV led to the generation of smooth continuous heave forces during the oscillation cycle.

Note that in the presence of the weaker vortex A , the pressure difference between the two sides of the swept plate was smaller than that of the unswept plate. Therefore, the pitch angles of the swept plate were much lower during most of the oscillation cycle. During these phases $t^* = 2/10$ to $4/10$, the swept plate essentially performed a heave-only motion, resembling the results reported by Mumtaz Qadri et al.[60] for oscillating-foils with pitch limiters. During such oscillations, the duration of the stroke reversal phase was shortened. In the absence of stall, the heaving distance was increased, providing an opportunity to increase the power extraction from the heaving motion. As a result, high power coefficient values were achieved by the swept plate, as shown in Fig. 4.1.

The LEV convected towards the trailing edge of the plate and proceeded to shed downstream during the stroke reversal phase. The remaining discussion in this section considers the LEV shed during the previous oscillation cycle. This positive (counter-clockwise) LEV is labelled B in Fig. 5.1, Fig. 5.2 and Fig. 5.3. Similar to vortex A described above, the vortex B occupied a larger area and had a larger peak vorticity in the case of the unswept plate, compared to its counterpart in the case of the swept plate. The vortex B was positioned farther downstream of the trailing edge of the plate in the case of the unswept plate at the spanwise location $z^* = 0.5$ (Fig. 5.1(i)) and in the case of the swept plate at $z^* = 0.88$ (Fig. 5.3(i)) compared to the case of the swept plate at $z^* = 0.5$ (Fig. 5.2(i)), where the secondary vortex was absent.

The strong circulation in the core of the vortex B of the unswept plate led to the rapid dispersion of vorticity (vortex burst) in the subsequent phases of the oscillation cycle. The dispersion of vorticity was related to the instability of the vortex core which is discussed in more detail in Section 5.3.2. In the case of the swept plate, the dispersion of vorticity was less pronounced. At $z^* = 0.5$, the vortex core of the

vortex B of the swept plate remained mostly intact, as shown in the plots of Fig. 5.2. The change in vorticity magnitude of the vortex B between the spanwise locations $z^* = 0.5$ and $z^* = 0.88$, shown in Fig. 5.2 and Fig. 5.3, respectively, indicates that vorticity dispersion occurred primarily in the z -direction. The dynamics of dispersion observed in both cases are linked to the rate of deformation of the vortex length in Section 5.3.3.

5.2 Contributions of the shed vorticity to the instantaneous forces on the plate

The momentum of a vortex-flow can be used in estimating the flow-induced forces acting on the plate by implementing a concept introduced by Lighthill [85] and Lamb [86]. The vector force acting on the plate can be calculated according to:

$$F = \frac{d}{dt} \rho \int r \cdot \omega dV \quad (5.1)$$

where $\int r \cdot \omega dV$ is the integral of the moment of vorticity with respect to the point of the application of the force. This method has been successfully applied for the cases of oscillating cylinders and foils by Oshkai and Rockwell [87], Siala and Liburdy [88], and more recently by Iverson et al. [89]. The contributions of the shed out-of-plane vorticity corresponding to the LEV, to the flow-induced forces were found by calculating the normalized integrals of the moments of the phase-averaged out-of-plane vorticity, the general dynamics of which are described in Section 5.1. The moments of vorticity acting in the streamwise (x -) and the lateral (y -) directions were then calculated as $(M_\omega)_x = -[1/(U_\infty^2 c)] \int y \omega_z dA$ and $(M_\omega)_y = -[1/(U_\infty^2 c)] \int x \omega_z dA$, respectively, where the point of the force application was assumed to be at the location of the pitching axis. The rate of change of the moments of vorticity, $d[(M_\omega)_x]/dt$ and $d[(M_\omega)_y]/dt$ provide the instantaneous force coefficients experienced by the oscillating-plate in their respective direction.

The calculated moments of vorticity corresponding to the LEV were categorized into those corresponding to the vortex A in the first-half of the oscillation cycle ($t^* = 0/10$ to $t^* = 4/10$) and the vortex B in the second-half of the oscillation cycle ($t^* = 5/10$ to $t^* = 9/10$). Figure 5.4 presents the moments of vorticity of the LEV in the case of the unswept plate at the spanwise location $z^* = 0.5$. Figure 5.5 and

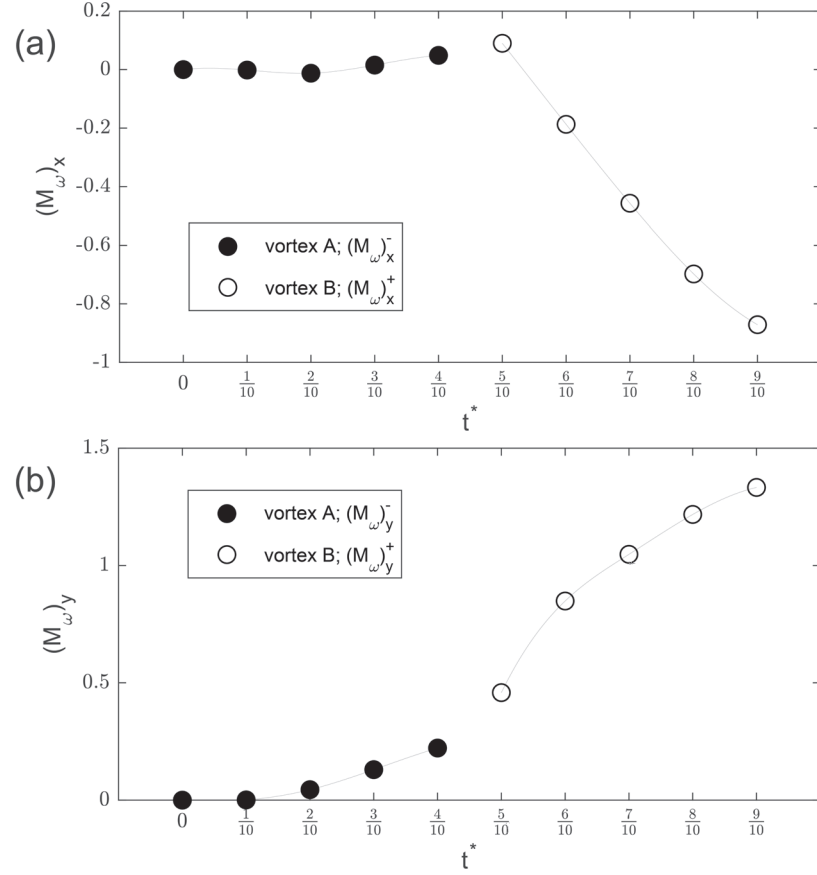


Figure 5.4: Calculated moments of vorticity $(M_\omega)_x$ (a) and $(M_\omega)_y$ (b) of the vortex A (\bullet) and the vortex B (\circ) for the unswept plate ($\Lambda = 0^\circ$) at $z^* = 0.5$.

Fig. 5.6 shows the moments of vorticity of the LEV in the case of the swept plate at $z^* = 0.5$ and $z^* = 0.88$, respectively.

Contributions of the shed negative vorticity, $(M_\omega)^-$ were evaluated for the moments of vortex A and contributions of the shed positive vorticity $(M_\omega)^+$ were evaluated in the opposite sign, using the moments of vortex B from the previous cycle. Note that because of the symmetry of the plate oscillations, these moments correspond to the same negative (clockwise-rotating) when considering a single oscillation cycle. The moments of vorticity of the vortex A and the vortex B are represented in the figures by the filled (\bullet) and the open symbols (\circ), respectively. The area of integration corresponds to the region occupied by respective vortex A and vortex B . The area of integration of the vortex B includes the layer of the shed positive vorticity extending from the plate to the core of the vortex.

The sequential locations of the vortex core with respect to the pitching axis are provided in Fig. 5.7. They were determined by tracking the position of the local

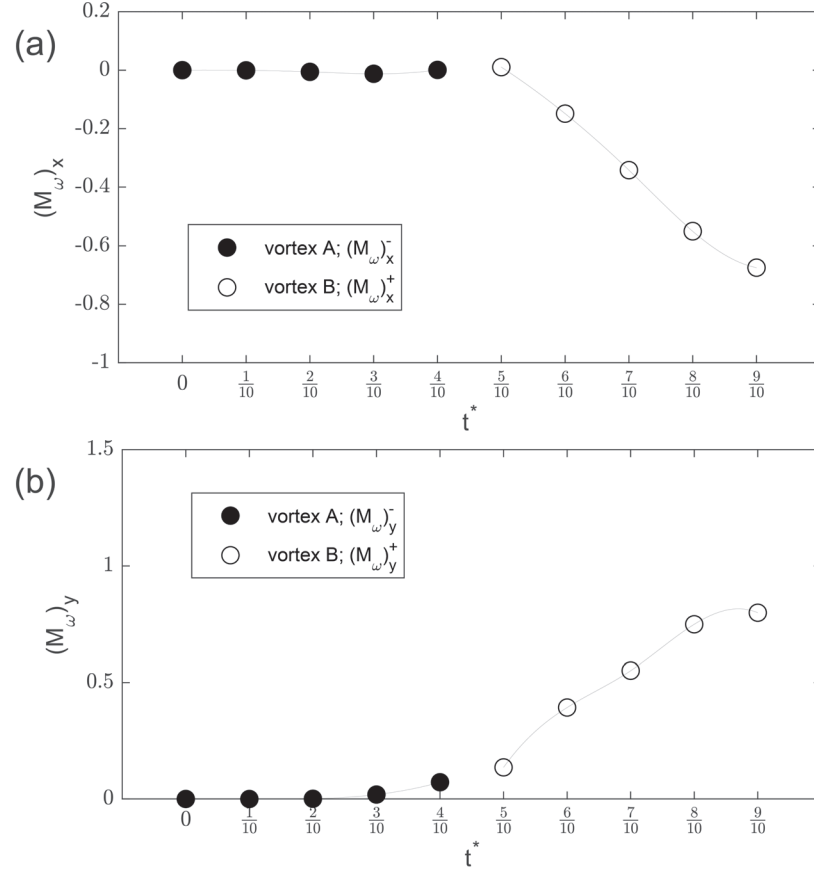


Figure 5.5: Calculated moments of vorticity $(M_\omega)_x$ (a) and $(M_\omega)_y$ (b) of the vortex A (●) and the vortex B (○) for the swept plate ($\Lambda = 6^\circ$) at $z^* = 0.5$.

maximum of the magnitude of vorticity within the specified area of integration.

At the beginning of the cycle from $t^* = 0/10$ to $t^* = 1/10$, the calculated moment of vorticity were negligible because the LEV represented by the vortex A was not resolved. As the vortex A grew and travelled away from the pitching axis in the successive phases from $t^* = 2/10$ to $t^* = 4/10$, the calculated moments $(M_\omega)_x$ and $(M_\omega)_y$ increased in magnitude. The moments of vorticity for all considered cases followed a similar trend over a complete oscillation cycle. The moment of vorticity contributing to the force in the lateral direction $(M_\omega)_y^-$ and induced by the negative vortex A, was larger in the case of the unswept plate, as shown Fig. 5.4(b). The larger magnitude of the moment $(M_\omega)_y^-$ for the unswept plate can be explained by the stronger circulation and the larger displacement of the vortex core from the pitching axis. Despite having a weaker circulation of the vortex core, the calculated moment $(M_\omega)_y^-$ in Fig. 5.6(b) corresponding to the swept plate at $z^* = 0.88$ was comparable with that corresponding to the unswept plate due to the larger displacement from the

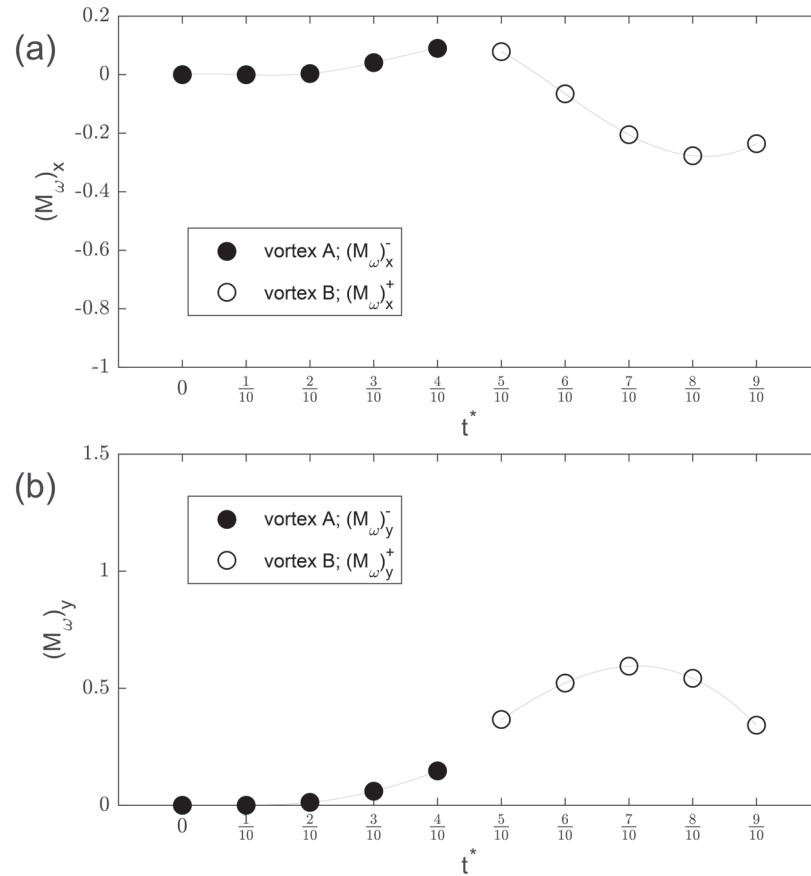


Figure 5.6: Calculated moments of vorticity $(M_\omega)_x$ (a) and $(M_\omega)_y$ (b) of the vortex A (●) and the vortex B (○) for the swept plate ($\Lambda = 6^\circ$) at $z^* = 0.88$.

pitching axis, shown in Fig. 5.7(b). Since the displacement of vortex A in the lateral direction was small, no significant moment $(M_\omega)_x^-$ was produced during the first-half of the cycle in all considered cases.

The contributions of the shed positive vorticity by the counter-clockwise-rotating vortex B occurred as the LEV convected downstream away from the trailing edge, during the second-half of the cycle from $t^* = 5/10$ to $t^* = 9/10$. In Fig. 5.4(b), the positive rate of change of the calculated moment in the lateral direction $d[(M_\omega)_y^+]/dt$ was the largest for the unswept plate at $t^* = 5/10$ and $t^* = 6/10$. The larger rate of change of the calculated moments implies that the instantaneous heaving force experienced by the unswept plate was higher than the force experienced by the swept plate at that phase, resulting in a larger heave velocity and higher oscillation frequency (Fig.4.1). Dissipation of the vortex B that occurred from $t^* = 7/10$ to $t^* = 9/10$ decreased the positive rate of change of the calculated moments, as shown in Fig. 5.4(b). The decreased positive rate of change translated to reduced instantaneous

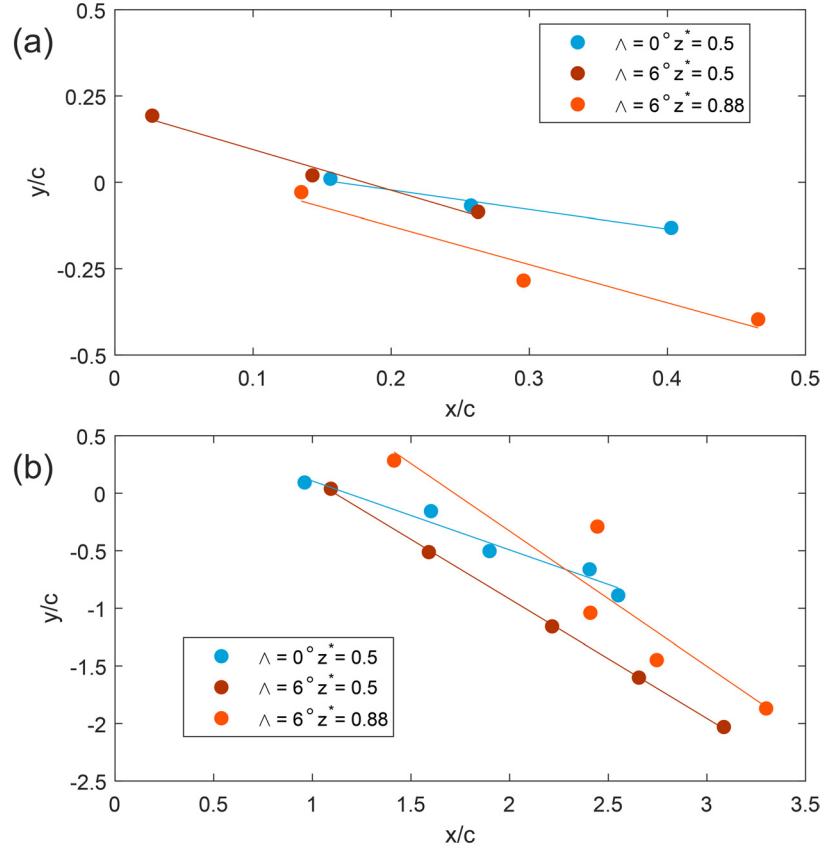


Figure 5.7: Location of the vortex A (a) at phase $t^* = 2/10$ to $t^* = 4/10$ and the vortex B (b) at phase $t^* = 0/10$ to $t^* = 4/10$ with respect to the pitching axis.

heaving force experienced by the unswept plate at the end of the oscillation cycle.

In the case of the swept plate, the contribution of the shed positive vorticity to the flow-induced lateral force had a smaller positive rate of change $d[(M_\omega)_y^+]/dt$ according to Fig. 5.5(b). The lack of the dissipation of the vortex B of the swept plate produced a consistent rate of change of $(M_\omega)_y^+$ throughout the entire second-half of the cycle. The observed trend of the calculated moment $(M_\omega)_y^+$ corresponds to the good synchronization of the heaving motion of the swept plate and the smooth, gradual variation of the heaving force exerted on the plate that is described in Section 4.2 and Section 5.1. At $t^* = 9/10$, part of vortex B travelled outside of the data acquisition area, leading to an incomplete capture of the shed vorticity. The incomplete capture of the vorticity was especially prominent in the case of the swept plate at $z^* = 0.88$ where the calculated moments exhibited an unphysical trend between $t^* = 7/10$ to $t^* = 9/10$, as shown in Fig. 5.6.

The calculated moment $(M_\omega)_x^+$ is associated with the flow-induced force of the

plate acting in the streamwise direction, which is of limited significance in energy harvesting applications. Given that vortex B was not significantly convected in the lateral direction, the trend of moment $(M_\omega)_x^+$ was predominantly determined by its circulation, resulting in a linear variation for $(M_\omega)_x^+$ in all considered cases. Nonetheless, it is useful to note that the moment $(M_\omega)_x^+$ was smaller in the case of the swept plate, compared to that of the unswept plate.

At the end of the oscillation cycle, the moments $(M_\omega)_x$ and $(M_\omega)_y$ reached their maximum magnitudes. The overall moments of vorticity were smaller in the case of the swept plate, which is counter-intuitive considering that the performance of the swept plate as an energy-harvesting device was better than that of the unswept plate, as discussed in Sections 4.2 and 5.1. According to Eq. 5.1, a vortex that convected farther away from the plate and that contained larger circulation provided a larger contribution to the flow-induced force on the plate. In the case of the swept plate, the rate of change of the streamwise displacement of the shed vortex B (Fig. 5.7(b)) was greater, and the vortex core was more stable, compared to the case of the unswept plate. The general dynamics of the LEV in the case of the swept plate suggest that the unchanging positive rate of change of the moment of vorticity in the lateral direction $d[(M_\omega)_y^+]/dt$ will persist for a longer period of time, for phases $t^* > 9/10$, compared to the decreasing $d[(M_\omega)_y^+]/dt$ of the unswept plate. This proposes that the summation of the moment of vorticity over the time domain in the case of the swept plate would then be significantly larger than that of the unswept plate.

The summation of the moment of vorticity over the time domain is defined as the impulse of the vortex-flow where the impulsive force induced by the vortex-flow is calculated by the integration of the induced force (Eq. 5.1) over time, $\int F dt$. Therefore, the appropriate parameter to consider when relating the induced forces to the energy harvesting performance would be the impulse of the vorticity. However, given the limited range of available data in the time domain in the present work, meaningful values of the impulse of vorticity were not obtained.

5.3 Three-dimensional vortex structure

The analysis of the quantitative flow patterns described in Sections 5.1 and 5.2, in conjunction with the turbine performance described in Section 4.2, indicates that controlled growth rate of the LEV and its core stability are the key factors in maintaining high flow-induced forces in the lateral direction, which are beneficial for the

performance of the turbine. Tomographic (3D) PIV was implemented to study the effects of the spanwise flow component on the LEV structure and to gain insights into the underlying three-dimensional fluid mechanics. This analysis is focused on the positive (counter-clockwise) vortex B at the phase $t^* = 1/10$ of the oscillation cycle.

The three-dimensional reconstruction of the phase-averaged structure of the vortex B was achieved by employing the Q criterion as a parameter defining the spatial extent of the vortex. In this approach, the Q criterion [90] defines a vortex as the regions where the local magnitude of the rate of rotation of the fluid exceeds the magnitude of the rate of strain:

$$Q = \frac{1}{2}(\|\Omega\|^2 - \|\mathbf{S}\|^2) \quad (5.2)$$

where Ω is the rate of rotation tensor, \mathbf{S} is the rate of strain tensor and $\|\cdot\|$ represents the tensor norm. The iso-surfaces of the Q criterion are presented in Fig. 5.9 and Fig. 5.10 for the LEV of the unswept plate and the swept plate, respectively. The iso-surfaces of the Q criterion corresponding to $Q = 15$, 225 and 850 were used to visualize separate structural features of the vortex B . The iso-surface of $Q = 15$ represents the outer edge of the vortex. The iso-surface of $Q = 225$ represents the inner region of the vortex. Lastly, the iso-surface of $Q = 850$ represents the core of the vortex.

A schematic of the location of the tomographic PIV data acquisition volume with reference to the plate and the 2D flow patterns is provided in Fig. 5.8. The x - and y -axis origin in Fig. 5.9 and Fig. 5.10 corresponds to the pitching axis of the plate at rest ($h/c = 0$), similar to the phase-average vorticity plots shown in Figs. 5.1–5.3. The z -axis location along the span of the tomographic PIV reconstruction volume corresponds to the spanwise location $z^* = 0.74$. The capture of the data acquisition volume was performed closer to the bottom tip of the plate to minimize the distance of the VOI from the cameras, which reduced light reflection from the free surface and improved the reconstruction quality of the volume. The details are further described in Appendix B.1.

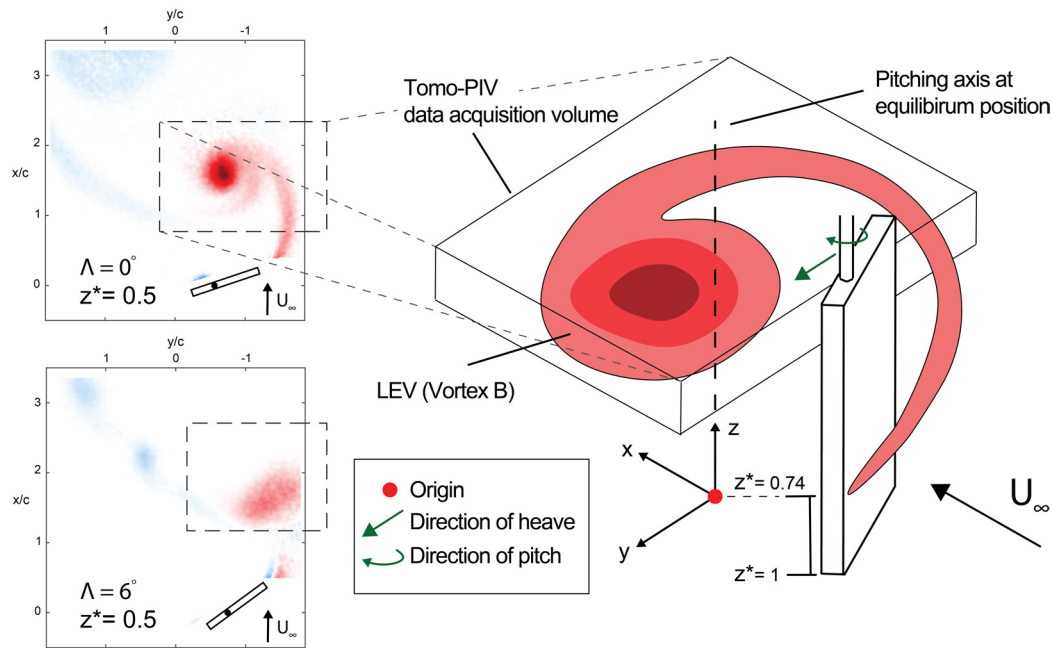


Figure 5.8: Schematic of the location of the tomographic PIV data acquisition volume with reference to the plate and the 2D vorticity plots at $t^* = 1/10$.

5.3.1 Spanwise variation of the structure of the LEV

The outer three-dimensional structure of the LEV produced by the unswept plate was parallel to the pitching axis of the plate (z -direction), as shown by the iso-surfaces corresponding to $Q = 15$ in Fig. 5.9. The lack of spanwise variation in the outer structure of the vortex indicated that the LEV was shed at the same phase of the oscillation cycle along the entire span of the unswept plate.

In the case of the swept plate, the outer structure of the LEV structure, represented by the iso-surface $Q = 15$ in Fig. 5.10, exhibited a tilt in the downstream (x -) direction. This observation, which indicates the presence of a dominant non-zero vorticity component in the x -direction, that was expected due to the presence of the sweep angle between the leading edge and the z -axis. Moreover, the LEV exhibited a tilt in the transverse (y -) direction, as can be seen in Fig. 5.10(c). This observation indicates the presence of a dominant non-zero vorticity in the y -direction that emerged due to the delayed shedding of the LEV along the span of the plate. Specifically, the shedding of the LEV was initiated early in the heaving oscillation cycle in the vicinity of the bottom (downstream) tip of the plate, as indicated by the patterns of the z -direction vorticity component described in Section 5.1. As the swept plate continued to heave in the y -direction, the portion of the LEV that was

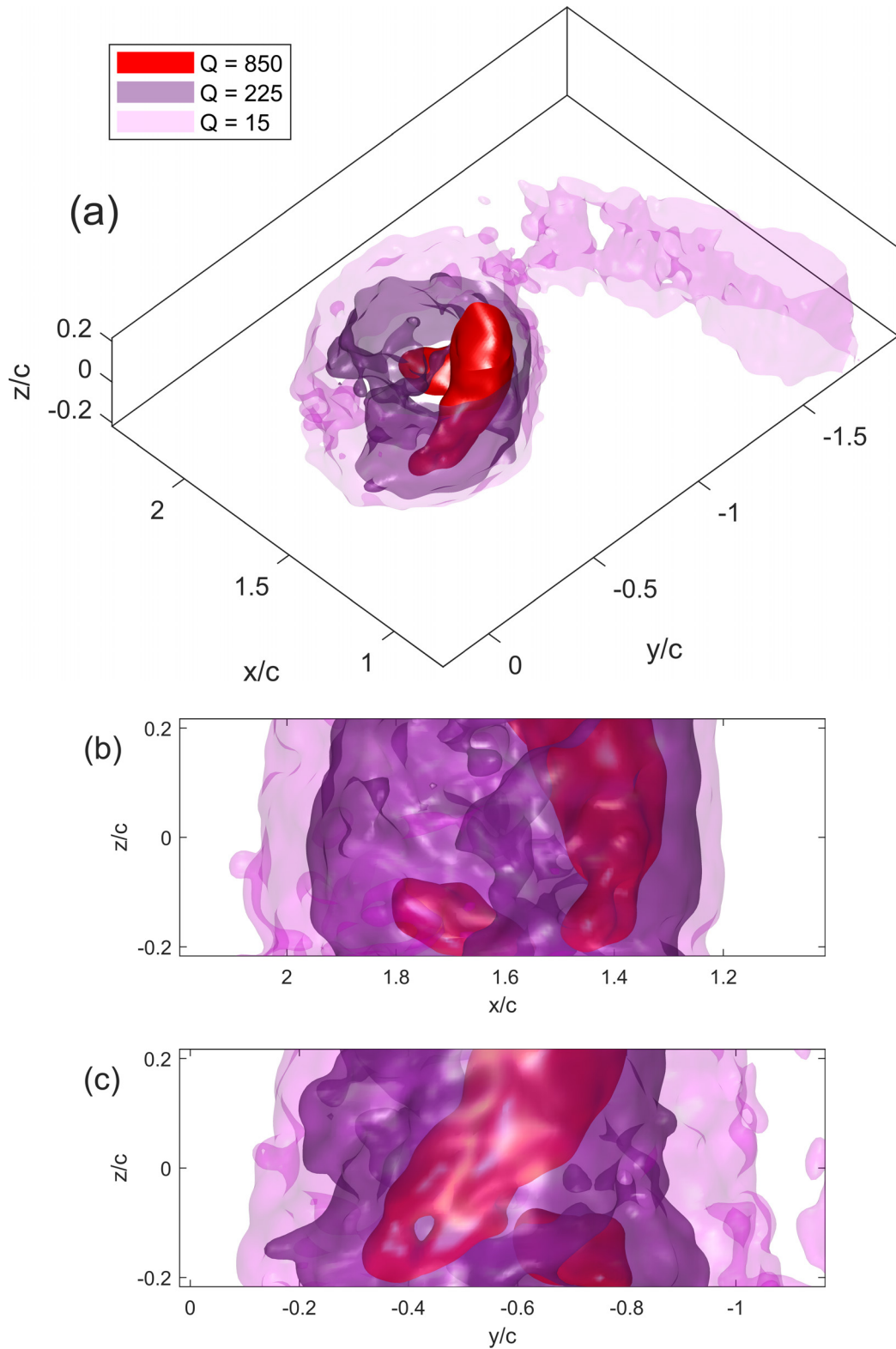


Figure 5.9: Iso-surface of the Q criterion of the vortex B in the case of the unswept plate ($\Lambda = 0^\circ$) at phase $t^* = 1/10$. Axonometric view (a), y -normal view (b) and x -normal view (c).

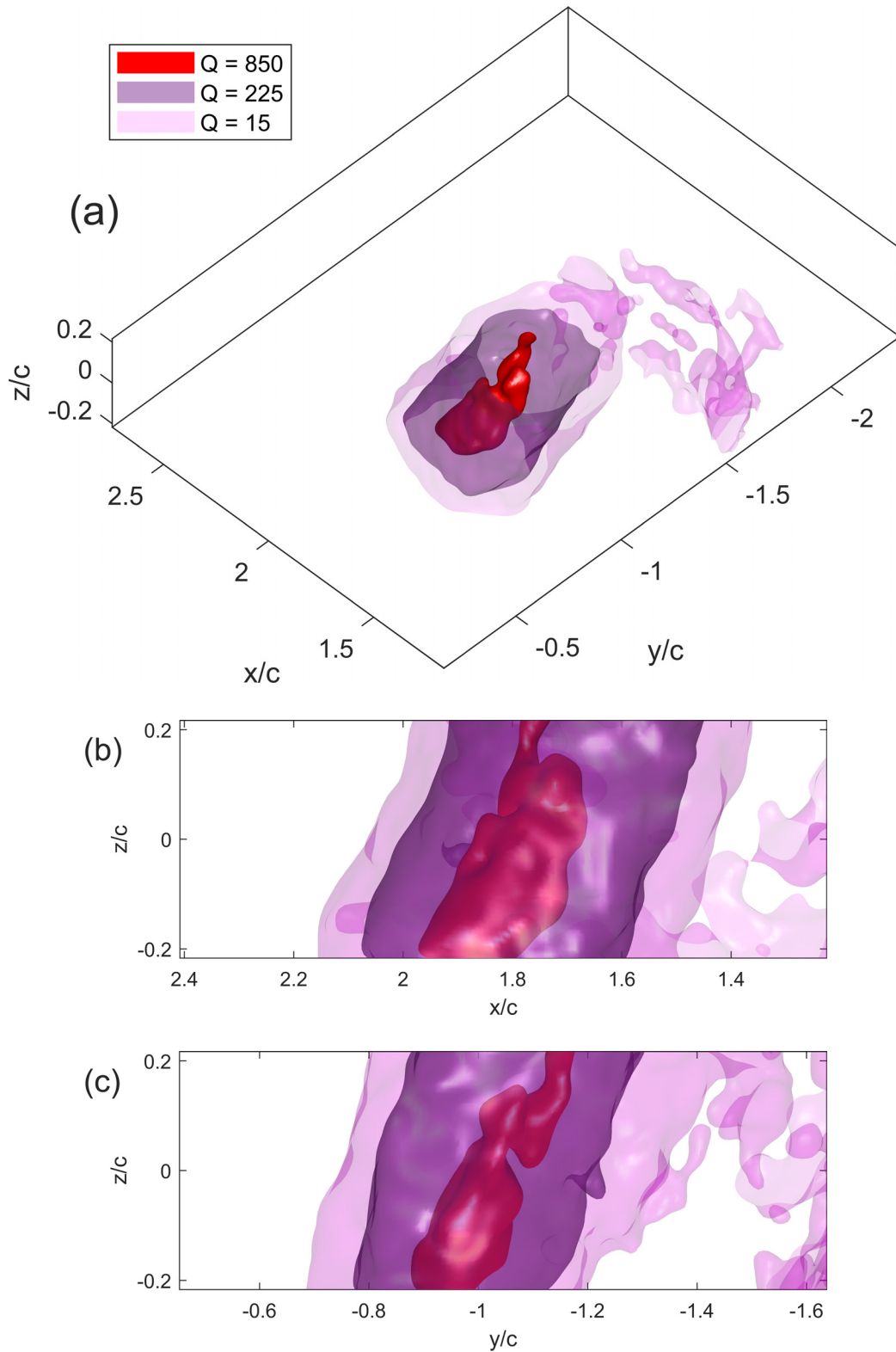


Figure 5.10: Iso-surface of the Q criterion of the vortex B in the case of the swept plate ($\Lambda = 6^\circ$) at phase $t^* = 1/10$. Axonometric view (a), y -normal view (b) and x -normal view (c).

still attached to the top (upstream) section of the plate was carried with it. At the same time, the y -position of the shed portion of the LEV in the vicinity of the bottom (downstream) section of the plate remained relatively unchanged. This delayed vortex shedding along the span of the plate resulted in the oblique vortical structure.

5.3.2 Inner structure and stability of the core of the LEV

In the case of the unswept plate (Fig. 5.9), the inner region and the core of the vortex B, represented by the iso-surface of the Q criterion, $Q = 225$ and $Q = 850$, respectively, exhibit the onset of instability in the form of the double-helical spatial structure. This structure is a manifestation of the instability of the core of the vortex, and it is a precursor of the vortex breakdown [91] that has been documented for the LEVs of delta wings [91] [92] [93] and for swirling flows [94] [95]. The instability of the inner region and the core of the LEV in the case of the unswept plate leads to an early breakdown and relatively small contribution of the LEV to the loading on the plate, as discussed in Section 5.2. Moreover, the core of the LEV exhibits a three-dimensional, axisymmetric instability, manifested in the form of the relative difference in the magnitude of the two helical strands of vorticity represented by the iso-surfaces of $Q = 850$. This instability is conceptually similar to the vortex breakdown mechanism observed for flows in rotating cylindrical enclosures [96] as well as swirling jets and wakes [97].

The helical structure of the core of the LEV was not observed in the case of the swept plate (Fig. 5.10), which indicates that the vortex core remained stable at the shown phase of the oscillation cycle. The enhanced stability of the core of the LEV had a beneficial effect on the energy-extraction performance of the swept plate in terms of generation of high-magnitude loading on the plate that was sustained over a large portion of the oscillation cycle, as discussed in Section 5.2. The physical mechanism of suppressing the three-dimensional instability is likely related to vortex stretching [98], which is described in more details in Section 5.3.3.

5.3.3 Deformation and stretching of the LEV

The Navier-Stokes equation of a viscous flow is written as:

$$\frac{D\underline{U}}{Dt} = -\nabla p + \nu \nabla^2 \underline{U} \quad (5.3)$$

where \underline{U} is the velocity vector, p is the pressure and ν is the kinematic viscosity. The vorticity equation is derived by taking the curl of the Navier-Stokes equation, Eq. 5.3:

$$\frac{\delta \underline{\omega}}{\delta t} = \nabla \times (\underline{U} \times \underline{\omega}) + \nu \nabla^2 \underline{\omega} \quad (5.4)$$

where $\underline{\omega}$ is the vorticity vector. Considering incompressibility of the fluid $\nabla \cdot \underline{U} = 0$, and the curl of a gradient vector being zero, $\nabla \cdot \underline{\omega} = 0$, the vorticity equation is expanded into:

$$\frac{D \underline{\omega}}{Dt} = \frac{\delta \underline{\omega}}{\delta t} + (\underline{U} \cdot \nabla) \underline{\omega} = (\underline{\omega} \cdot \nabla) \underline{U} + \nu \nabla^2 \underline{\omega} \quad (5.5)$$

deformation term diffusion term

On the right hand side, the vorticity equation Eq. 5.5 consist of the deformation term $(\underline{\omega} \cdot \nabla) \underline{U}$ and the diffusion term $\nu \nabla^2 \underline{\omega}$. The term $(\underline{\omega} \cdot \nabla) \underline{U}$ represents the rate of deformation of vorticity due to a combination of turning and stretching motions, while the term $\nu \nabla^2 \underline{\omega}$ represents the rate of diffusion of vorticity due to viscosity. It should be noted that in a 2D flow the deformation term is identically equal to zero due to the fact that the vorticity vector is normal to the velocity vector everywhere in the flow domain. In this section, the contributions of the stretching and turning motions to the deformation term are related to the vorticity transport in the LEV of the oscillating-plate and the stabilization of LEV.

By expanding the deformation term, $(\underline{\omega} \cdot \nabla) \underline{U}$ into its individual Cartesian components, as shown in Eq. 5.6a to 5.6c, the turning and stretching motions can then be defined. The vorticity stretching term, $(\omega \cdot \nabla) U_{\parallel}$ represents the deformation rate of the vortex length along the vortex line. The vorticity turning terms, $(\omega \cdot \nabla) U_{\top}$ and $(\omega \cdot \nabla) U_{\perp}$ represents the deformation rate of the vortex length away from the centre of curvature and along the tangential line, respectively.

$$x : \frac{D \omega}{Dt} = \omega_x \frac{\delta u_x}{\delta x} + \omega_y \frac{\delta u_x}{\delta y} + \omega_z \frac{\delta u_x}{\delta z} \quad (5.6a)$$

$$y : \frac{D \omega}{Dt} = \omega_y \frac{\delta u_y}{\delta y} + \omega_z \frac{\delta u_y}{\delta z} + \omega_x \frac{\delta u_y}{\delta x} \quad (5.6b)$$

$$z : \frac{D \omega}{Dt} = \omega_z \frac{\delta u_z}{\delta z} + \omega_x \frac{\delta u_z}{\delta x} + \omega_y \frac{\delta u_z}{\delta y} \quad (5.6c)$$

$(\omega \cdot \nabla) U_{\parallel}$ $(\omega \cdot \nabla) U_{\top}$ $(\omega \cdot \nabla) U_{\perp}$

The iso-surfaces of the vorticity turning terms for the unswept plate are plotted in Fig. 5.11 and Fig. 5.12, respectively. The iso-surfaces of the vorticity turning terms for the swept plate are plotted in Fig. 5.13 and Fig. 5.14, respectively. The iso-surfaces of the vorticity stretching terms are plotted in Fig. 5.15 and Fig. 5.16 for the unswept plate and swept plate, respectively. In each figure, the pink colour represents an iso-surface of the Q criterion, $Q = 15$, which provides a spatial reference for the extent and location of the LEV. The superscripts $+$ and $-$ indicate the direction of the deformation with respect to the labelled Cartesian components. For example, the label x^+ indicates a deformation of vorticity in the positive- x -direction.

In the case of the unswept plate, the vorticity turning terms $(\omega \cdot \nabla)U_{\top}$ and $(\omega \cdot \nabla)U_{\perp}$ shown in Fig. 5.11 and Fig. 5.12, appeared in approximately equal zones of positive and negative directional contributions. The iso-surfaces representing the positive and negative contributions of the turning terms $(\omega \cdot \nabla)U_{\top y}$ (Fig. 5.11(b)) and $(\omega \cdot \nabla)U_{\perp x}$ (Fig. 5.12(a)) formed a helical configuration, while the iso-surfaces representing other turning terms formed pairs of parallel elliptical cylinders corresponding to the positive and negative contributions. Both types of the spatial structure resulted in a near-zero net turning deformation in each of the Cartesian directions.

In contrast, in the case of the swept plate, the vorticity turning terms in all Cartesian directions were non-zero, as shown in Fig 5.13 and Fig 5.14. It should be noted, however, that these terms still produced a nearly zero combined turning deformation i.e. $(\omega \cdot \nabla)U_{\top x} + (\omega \cdot \nabla)U_{\perp x} \approx 0$. The absence of the net turning of vorticity was expected in both cases based on the time evolution of the LEV shown in Fig. 5.1, which exhibited no turning movement.

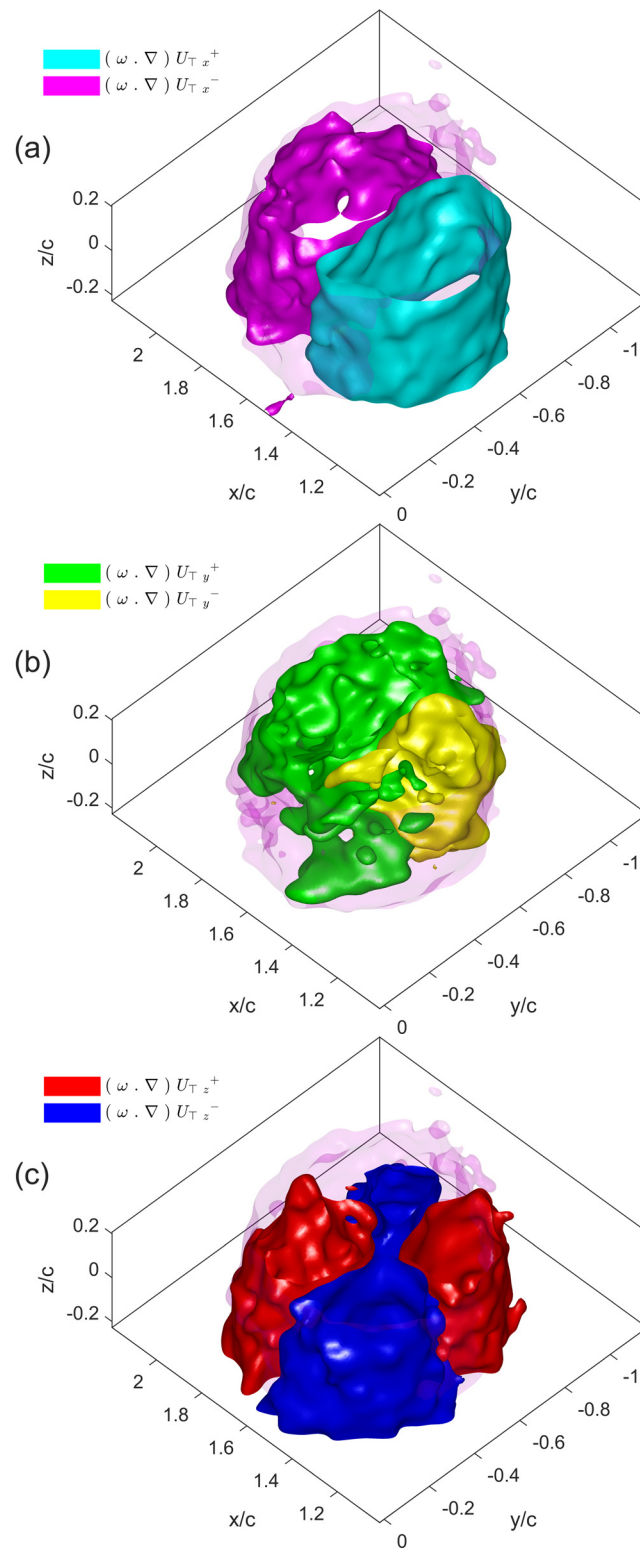


Figure 5.11: Iso-surfaces of the vorticity turning term $(\omega \cdot \nabla)U_T = \pm 75$ in the x -direction (a), y -direction (b) and z -direction (c) for the case of the unswept plate ($\Lambda = 0^\circ$). The iso-surface of the $Q = 15$ is indicated by the light pink colour.

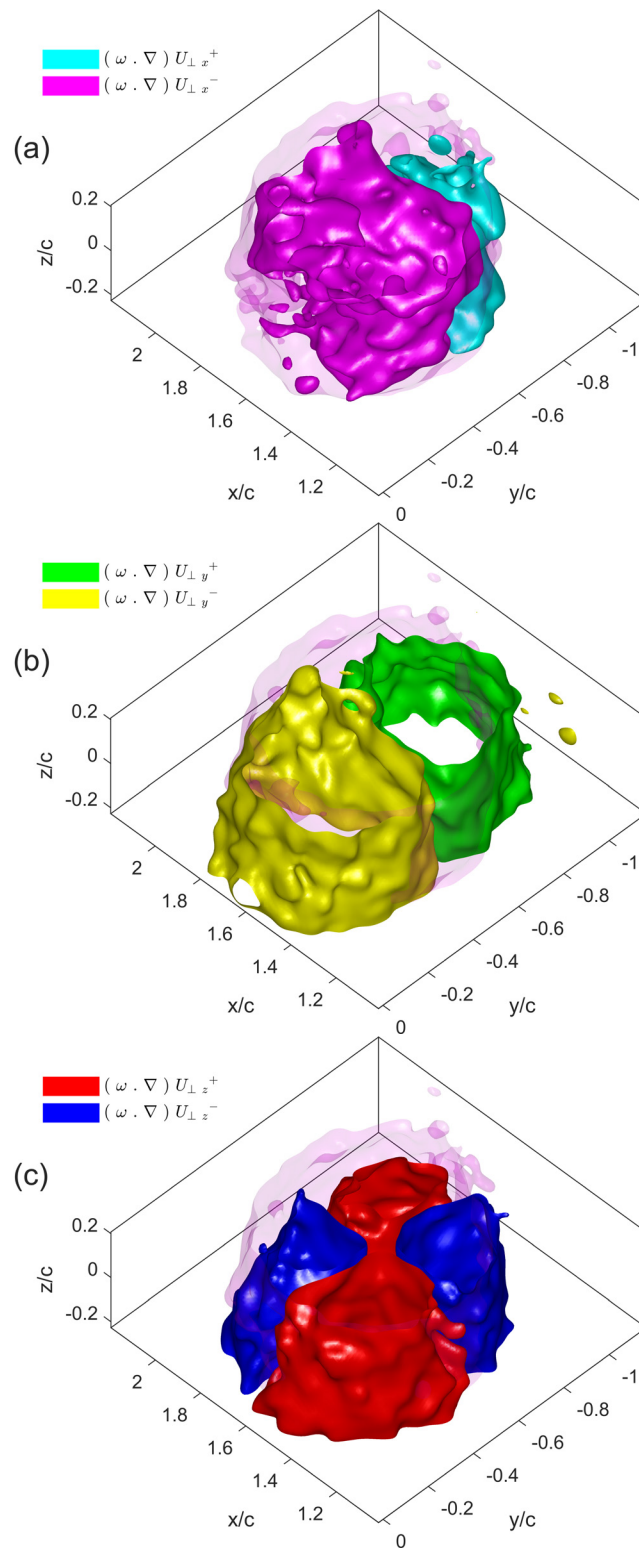


Figure 5.12: Iso-surfaces of the vorticity turning term $(\omega \cdot \nabla)U_{\perp} = \pm 75$ in the x -direction (a), y -direction (b) and z -direction (c) for the case of the unswept plate ($\wedge = 0^\circ$). The iso-surface of the $Q = 15$ is indicated by the light pink colour.

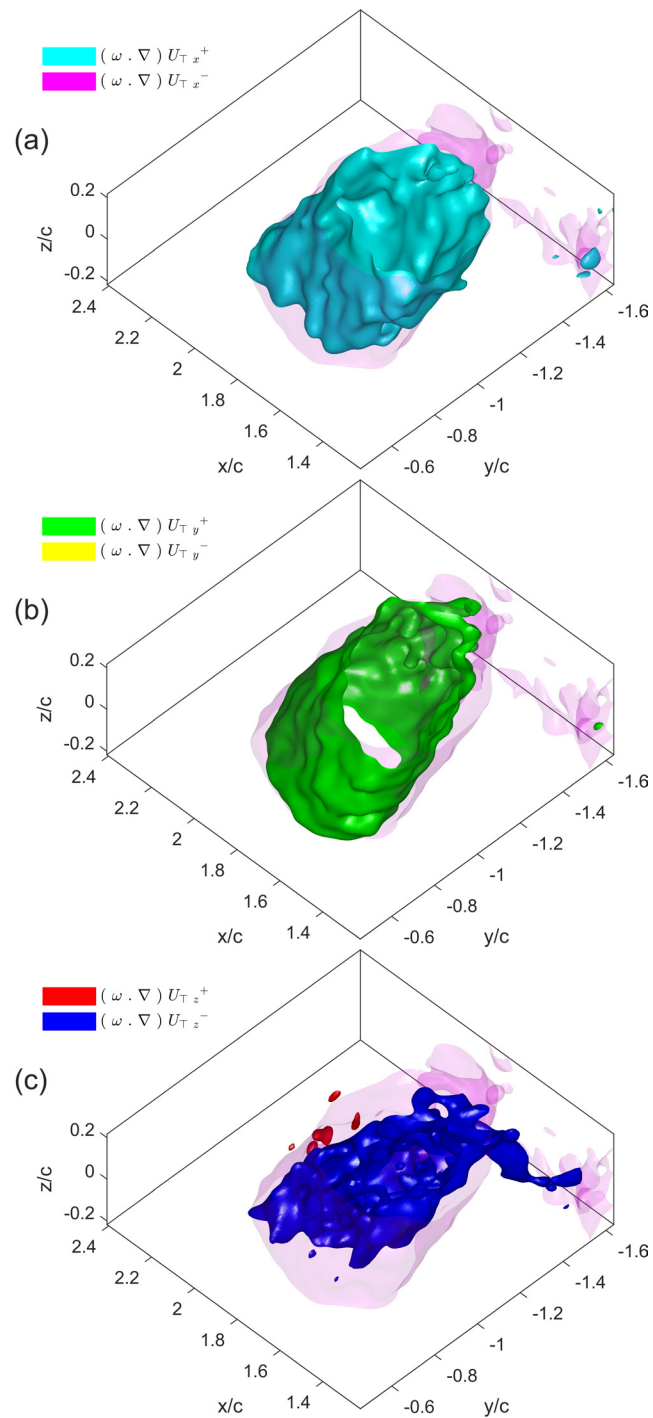


Figure 5.13: Iso-surfaces of the vorticity turning term $(\omega \cdot \nabla)U_{\tau} = \pm 75$ in the x -direction (a), y -direction (b) and z -direction (c) for the case of the swept plate ($\Lambda = 6^\circ$). The iso-surface of the $Q = 15$ is indicated by the light pink colour.

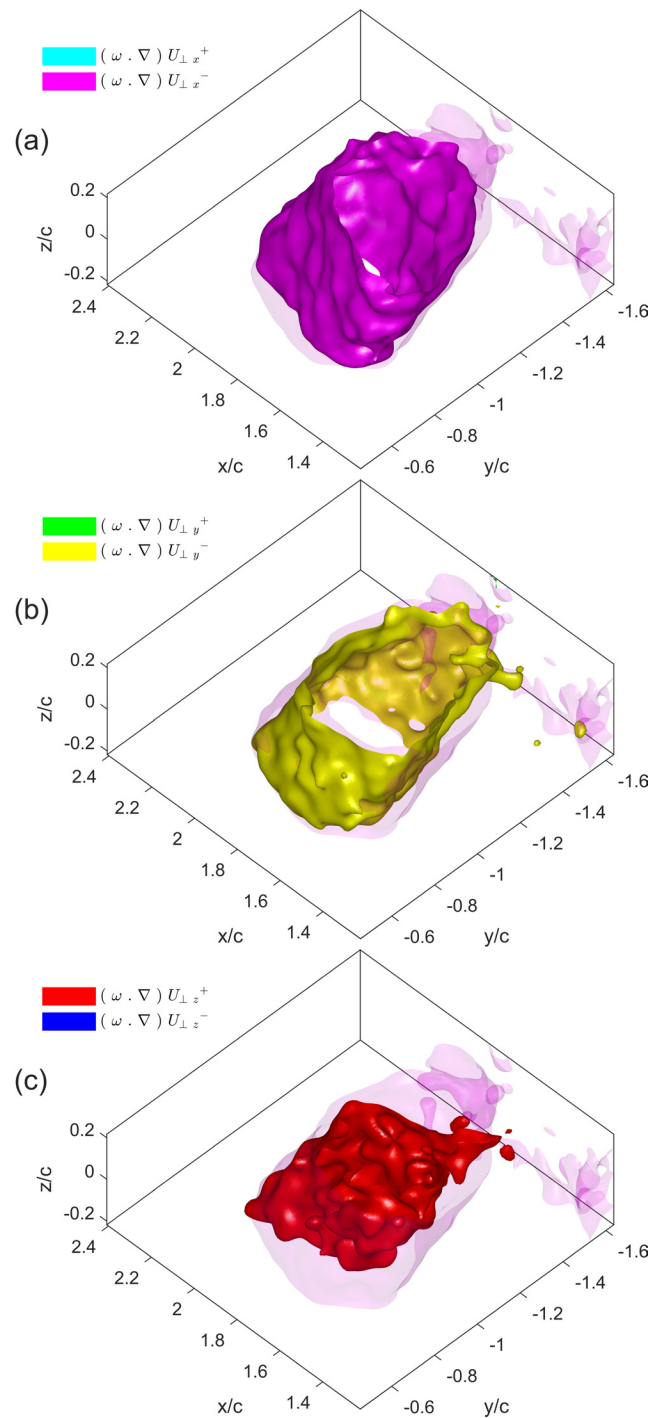


Figure 5.14: Iso-surfaces of the vorticity turning term $(\omega \cdot \nabla)U_{\perp} = \pm 75$ in the x -direction (a), y -direction (b) and z -direction (c) for the case of the swept plate ($\Lambda = 6^\circ$). The iso-surface of the $Q = 15$ is indicated by the light pink colour.

The positive and the negative contributions of the vorticity stretching terms in the x - and the y -directions, $(\omega \cdot \nabla)U_{\parallel x}$ and $(\omega \cdot \nabla)U_{\parallel y}$, shown in Figs. 5.15(a) and 5.15(b) for the case of the unswept plate, did not cancel each other as was the case with the vorticity turning terms. The vorticity stretching terms $(\omega \cdot \nabla)U_{\parallel x}$ and $(\omega \cdot \nabla)U_{\parallel y}$ both provided net negative contributions to the vorticity transport. The effects of the vorticity stretching on the dispersion of the LEV can be observed in the sequence of the patterns of the out-of-plane vorticity in Fig. 5.2.

In the case of the unswept plate, the LEV exhibited negative stretching in the z -direction, $(\omega \cdot \nabla)U_{\parallel z}$ in the core of the vortex. This type of deformation likely stemmed from the centrifugal forces that displaced fluid from the core of the vortex. This displacement resulted in a flow resembling a meridional circulation observed in lid-driven cavity experiments [95] [99]. In contrast to the case of the swept plate, where the LEV exhibited predominantly positive stretching in the z -direction (Fig. 5.16(c)), the negative z -component stretching did not enhance stability of the LEV in the case of the unswept plate.

In the case of the swept plate, the LEV exhibited a net positive stretching in the x -direction, $(\omega \cdot \nabla)U_{\parallel x}$, while undergoing a net negative stretching in the y -direction, $(\omega \cdot \nabla)U_{\parallel y}$, as shown in Figs. 5.16(a) and 5.16(b), respectively. However, the magnitudes of the vorticity stretching in the x - and the y -directions were different, resulting in the unidirectional dispersion of the LEV, which is evident in the out-of-plane vorticity plots of Fig. 5.2.

A significant amount of positive vorticity stretching in the z -direction, $(\omega \cdot \nabla)U_{\parallel z}$ was observed at the core of the LEV of the swept plate, shown in Fig. 5.16(c). The lengthening of the vortex reduced its diameter, which in turn led to the reduced growth of LEV in the case of the swept plate that is discussed in Section 5.1. Furthermore, the suppressed growth of the LEV ties directly to the stable vortex core shown in Fig. 5.10. The stability of vortex core is in agreement with the observation by Wong and Rival [71], who related stabilization of the LEV to vorticity stretching.

The stretching of vorticity is correlated with the increased velocity gradient along the span of the plate. In severe cases, large velocity gradient along the span was found to cause destabilization and bursting of the vortex [100] [101]. However, in the current investigation, the sweep angle was relatively small, and the resulting velocity gradient did not trigger destabilization of the LEV. On the contrary, the moderate velocity gradient prevented the onset of the helical instability in the vortex core and premature breakdown observed in Fig. 5.9 for the case of the unswept plate.

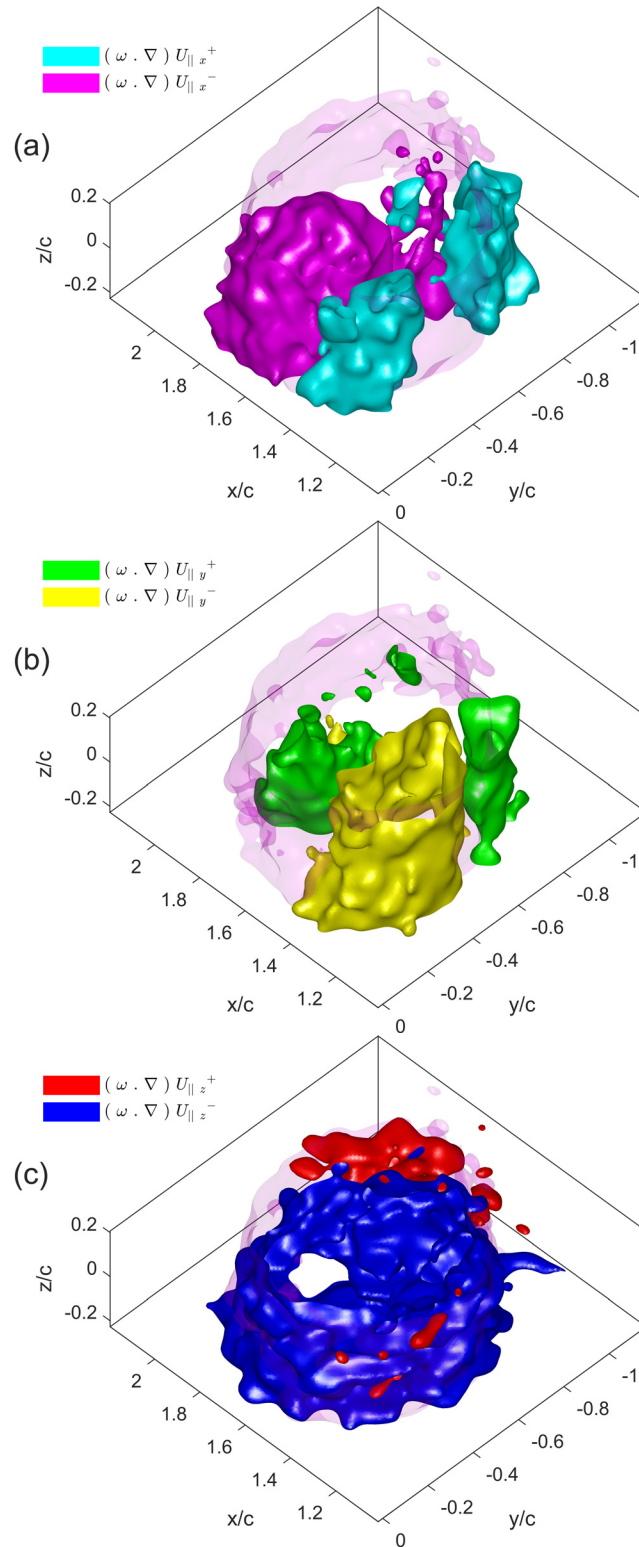


Figure 5.15: Iso-surfaces of the vorticity stretching term $(\omega \cdot \nabla)U_{\parallel} = \pm 75$ in the x -direction (a), y -direction (b) and z -direction (c) for the case of the unswept plate ($\wedge = 0^\circ$). The iso-surface of the $Q = 15$ is indicated by the light pink colour.

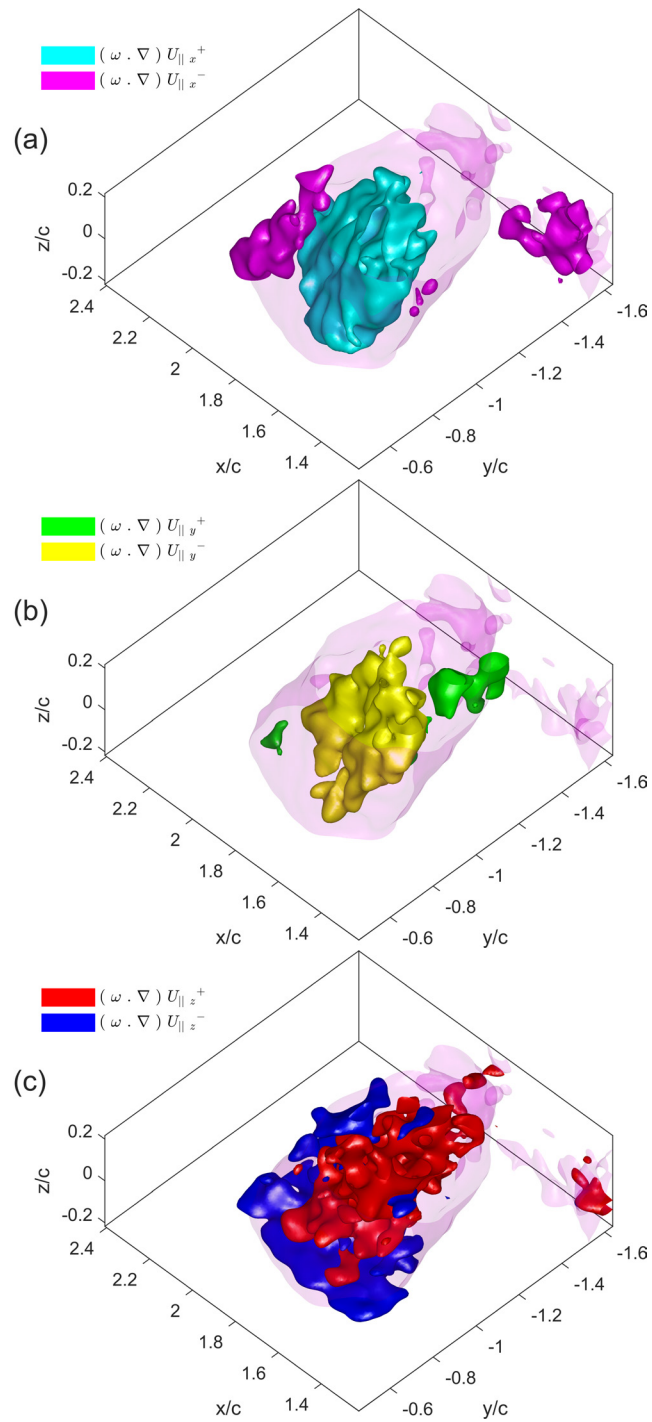


Figure 5.16: Iso-surfaces of the vorticity stretching term $(\omega \cdot \nabla)U_{\parallel} = \pm 75$ in the x -direction (a), y -direction (b) and z -direction (c) for the case of the swept plate ($\Lambda = 6^\circ$). The iso-surface of the $Q = 15$ is indicated by the light pink colour.

Chapter 6

Conclusion

The influence of the sweep angle of 6° on the fully-passive oscillating-plate turbine prototype was investigated and the performance of the turbine was related to the dynamic flow structure by analyzing the 2D and 3D LEV flow patterns. The use of the planar and tomographic PIV in the present work was successful in evaluating the flow field and visualizing the LEV. The appropriate PIV setups along with the data quality and accuracy were assessed as well (Appendix A and Appendix B.1).

The kinematic and performance parameters of the unswept plate and the swept plate were obtained for varying inflow velocity. The unswept plate was reported to achieve maximum power coefficient of $C_p = 0.61$, and efficiency of $\eta = 23.6\%$ at low inflow velocity of $U_\infty = 0.35$ m/s. Beyond $U_\infty = 0.35$ m/s, performance matrices of the unswept plate diminished with increasing inflow velocity as the turbine deviates from the ideal oscillation mode of large heave and pitch amplitudes. On the other hand, the power coefficient of the swept plate increased with increasing inflow velocity, reaching a maximum power coefficient of $C_p = 0.78$ at $U_\infty = 0.5$ m/s. The efficiency in the case of the swept plate remained relatively consistent at $\eta \approx 23\%$ throughout the majority of the tested inflow velocities, with an insignificant decrease at higher inflow velocities. The swept plate was able to maintain oscillations of large heave amplitudes throughout a wider range of velocities, which was ideal for the performance of the turbine.

Planar PIV was utilized in the visualization of the flow structure of the wake in first-half of the oscillation cycle. The initial formation of LEV and its subsequent shedding into the wake were successfully captured in the phased-averaged out-of-plane vorticity fields. In the case of the unswept plate, the high rate of growth of the LEV led to the quick shedding of the LEV from the plate, which initiated deep stall. In

the case of the swept plate, the growth of the LEV was suppressed by the presence of spanwise transport of vorticity. The flow remained attached at the mid span of the swept plate without any sign of the shedding of LEV. LEV shedding was observed near the bottomward span where the vorticity was concentrated. However, the timing of the LEV in the case of the swept plate still occurred later within the oscillation cycle when compared to the case of the unswept plate. Dispersion of vorticity of the shed LEV in the wake was observed in the case of the unswept plate, but the shed LEV in the case of the swept plate remained coherent with less pronounced vorticity dispersion. The lack of vorticity dispersion indicated that the LEV in the case of the swept plate was more stable than that of the unswept plate.

The 2D flow field results were then correlated to the induced forces experienced by the plate by calculating the moment of vorticity. The overall moment of vorticity in the case of the unswept plate was larger in magnitude. Despite that, a significant decrease in the rate of change of the moment of vorticity was observed in the case of the unswept plate and was linked to the premature vortex breakdown seen in the 2D vorticity fields. The rate of change of the moment of vorticity for the swept plate was consistent due to the more stable vortex core. The results suggest that the overall impulsive force induced by the vortex-flow on the swept plate over an oscillation cycle was significantly larger than that of the unswept plate, which was in accordance with the better performance parameters achieved by the swept plate at higher inflow velocities.

The effects of the spanwise flow component on the dynamics of the LEV structure were further analyzed using the 3D flow field obtained from the tomographic PIV technique. The proposed notion on delayed shedding of LEV vortex was verified from the spanwise variation of the structure of the LEV. Vortex core breakdown in the form of helical configuration was observed in the case of the unswept plate. The deformation and stretching of the LEV were also quantified using the vortex deformation terms embedded in the vorticity equation and linked to the vortex dispersion seen in the 2D flow fields. The results showed that positive stretching at the core of the vortex, along the vortex line, which was present in the case of the swept plate, improved the stability of the LEV and mitigated the onset of premature vortex breakdown.

The main conclusion from the present work is that the sweep angle parameter is a valuable structural parameter in oscillating-foil systems. The results show that the total power extraction of the plate benefit from continuous prolonged heave force

rather than a short high instantaneous burst of force seen in the case of the unswept plate. The introduction of the sweep angle on oscillating-plate was effective in inducing such kinematics involving large heave amplitudes, which led to the significant increase in energy extraction performance, especially at higher inflow velocities. The spanwise flow component produced by the sweeping of the leading edge was successful in the control of the growth rate of the LEV and the subsequent delay of LEV shedding. Vortex core stability was also improved in the presence of spanwise flow. The combination of these LEV dynamics was determined to be factors enhancing the turbine performance. Thus, the sweep angle should be considered when designing oscillating-foil energy harvesting devices in the future.

6.1 Future Work

The present work has opened the path for an effective method of hydrodynamic optimization of oscillating-foil turbines. The present work initiated the utilization of the sweep profile concept and verified its capability to improve the energy harvesting performance of oscillating-foil turbines. Nevertheless, the improvement was only demonstrated for a single sweep angle case at $\Lambda = 6^\circ$. There are much more to explore on the subject. Further progress is needed to fully utilize the proposed findings onto practical applications of oscillating-foil systems. The following are the recommend directions of research ensuing the present work.

A parametric study of the normalized structural parameters of the swept plate should be performed. Recalling from Section 4.1, only one set of structural parameters was tested in the present work. A parametric study across the normalized structural parameters, similar to the work done in the previous campaign by Boudreau et al.[44], is beneficial in exploring the system dynamic responses and relating them to the extent of the energy-harvesting capability of the swept plate. A recommendation of an immediate follow up study from the present work would be to increase the linear heave damping coefficient, $D_{h,e}^*$ and determine the extent of the increase of the power coefficient of the turbine at higher inflow velocities, in which was restricted by the mentioned design constraint in the present work. The adjustment to $D_{h,e}^*$ will also improve efficiency at higher inflow velocities by limiting the size of the extraction window and the flux of kinetic energy passing through it.

Further research on various sweep angle should be performed as well. The spanwise flow component induced by the sweep angle of 6° has demonstrated significant

alternations to the LEV of the fully-passive system. The larger the magnitude of the spanwise flow component will be. However, the moment of inertia and static moment of the system also increases with the sweep angle. The study on various sweep angle could be done to find a right balance between the spanwise flow component and hydrodynamical damping caused by the structural parameters, such as resistance caused by the moment of inertia and static moment of the system. It is reasonable to assume that there exists an optimal sweep angle which will improve the energy harvesting capability of oscillating-foil turbines. Simultaneously, this proposed study of various sweep angle will also characterize the relationship between the vortex stability and the spanwise flow component.

The present work demonstrated that simple changes in the geometrical features of the foil can provide significant changes in the fluid-structure interactions between the fluid and the foil. Other than the sweep angle, additional geometrical features such as the aspect ratio on the foil should be a focus of future endeavours. For example, it is recommended to start from the simple study of the aspect ratio of a rectangular swept foil, by manipulating the scaling of the chord length components (c and c') and span length components (b and b'), presented in Fig. 2.3. This study could then be further branched into complex geometries involving varying chord length along the span, such as the tapered foils which could balance the local static moment and moment of inertia. Twisted wing, where azimuth angles are introduced between the chords of each foil tip, also make an interesting investigation, in which the local angles of attack varies along the span of the foil.

Lastly, the present work involved only the use of pitching axis oriented perpendicular to the streamwise axis. The use of this orientation of the pitching axis caused the dissimilarity in the position of x_p , discussed in Section 2.2. The problem could be solved by orienting the pitching axis to be parallel to the leading edge line. This change in the orientation of the pitching axis shifts the aerodynamic center to align better with the center of pressure. However, by doing so, gravitational effects come into play. If the pitching axis is not placed at the center of the chordwise length of the blade, gravitation force will act on the pitch degree of freedom of the foil, adding another layer of complexity to the already complicated system. Nevertheless, the use of gravity to alter the pitch kinematic of the foil also poses as another innovative method of hydrodynamic optimization of oscillating-foil systems.

Appendix A

Validation of vector fields acquired from Planar PIV

The number of averaged instantaneous velocity fields is an important factor when considering the accuracy of the data, which is prominent with the experimental setup in the present work, where the instance of image capture is not consistent. As mentioned previously, the timing of the triggering of the image capture was based on the heave position of the plate supplied by the heave encoder. Due to the passive nature of the system, the dissimilarity of the heave velocity at each instance of image capture resulted in slight phase variation between each acquired raw images for a given heave position trigger. The moment of vorticity defined in Eq. 5.1 is a function of the x - and y -displacements between the vortex and the pitching axis of the plate. Any shift in the phase of the image capture will eventually reflect in the displacement of the vortex from the pitching axis, and subsequently, the consistency of the calculated moments.

The inconsistency in the phase of the image capture of the plate oscillation can be solved by the ensemble averaging over a large number of raw images. However, given an extended image acquisition period, the bearings of the prototype would suffer a considerable amount of wear. The viscous damping and coulomb friction will deviate far from its initial state at the start of each test, leading to discrepancies in the results for the particular round of test. Thus, an optimal number of images was needed to be determined to minimize the duration of the experiments, while obtaining consistent and comparable results.

The number of averages was selected according to the number of instantaneous

velocity fields required for the calculated moment of vorticity (Eq 5.1) of the phase-averaged out-of-plane vorticity field to converge. A preliminary 2D PIV experiment was conducted with the unswept plate at phase $t^* = 3/10$ at inflow velocity $U_\infty = 0.41$ m/s, matching the case described in Section 5.1. A total of 500 images were acquired at 13 Hz. Figure A.1 shows the averaged moments of vorticity of each positive and negative vorticity contribution in the x - and y -components with 25, 50, 150, 250, 300, 350, 400 and 500 instantaneous velocity fields. The moments of vorticity approached convergence with an increasing number of averaged instantaneous fields. Based on the convergence trend, 300 number of averages was determined to be the optimal number of images that provided consistent results.

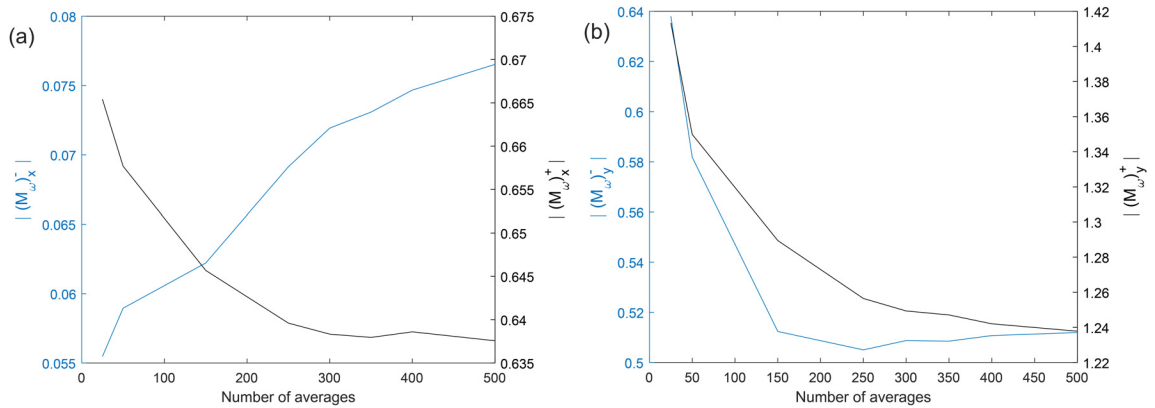


Figure A.1: The number of instantaneous vorticity fields and the calculated averaged moment of vorticity in the x -component (a) and y -component (b).

Appendix B

Assessment of the Tomographic PIV data quality

B.1 Quality of the tomographic reconstruction

The z -plane boundary of the VOI was selected by studying the signal-to-noise ratio, SNR of the illuminated volume. Estimation of SNR was done by dividing the intensity measured within the VOI, $I_{insideVOI}$ by the intensity outside the bounds of the VOI, $I_{outsideVOI}$:

$$SNR = \frac{I_{insideVOI}}{I_{outsideVOI}} \quad (\text{B.1})$$

The intensity outside the illuminated volume was not zero due to the presence of ghost particles. The ghost intensity was assumed to be uniform across the entire reconstructed volume. A larger SNR value implies that the contribution of the ghost particles within the VOI is lower compared to the contribution of the intensity by the illumination, resulting in decreased noise and improved volumetric reconstruction quality. According to Scarano [77], a volume reconstruction of $SNR \geq 2$ is an indication of good reconstruction quality with high-confidence, usually complemented by satisfactory Tomographic PIV recordings.

The double-frame imaging PIV technique involves the calculation of particle displacements from two pulses of laser illumination. Figure B.1 shows the measured z -intensity profile of the initial pulse (frame 1) and the subsequent pulse (frame 2) across the reconstructed volume. Here, the reconstructed volume had a thickness of

50 mm (an additional 10 mm on each side of the boundary), which was intentionally larger than the thickness of the DAV of 30 mm to capture the ghost particles outside the illuminated boundary. Examples of the reconstructed volumes are available in Appendix C to guide the reader on particles and intensities via physical representations. The reconstructed volume spanned from $z = 195$ mm to 245 mm and the boundary of the illuminated volume was $z = 205$ mm and 235 mm. Here, the origin of the three-dimensional vortex structure described in Section 5.3, $z^* = 0.74$ corresponds to $z = 223$ mm.

Figure. B.1 shows that the SNR values close to the boundary of the VOI at $z = 205$ mm was decreased, especially for the SNR values of the second laser pulse. This result is explained by the light reflection from the prototype components placed above the water channel and the free surface. The reflected light from the first pulse increased the background intensity during the capture of the second frame, resulting in increased noise at the edge of the volume reconstruction at $z = 195$ mm. The effort to prevent such reflection was taken by decreasing the exposure of metal surfaces with black tape and reducing the energy of the laser pulse. However, the issue could not be entirely prevented. Thus, the selected thickness of the VOI in the present work was strictly limited to regions with $SNR \geq 2$. The span $z = 212$ mm to 234 mm, marked by dashed lines in Fig. B.1, fulfilled such requirement. The estimated $I_{insideVOI}$, indicated by the red horizontal line in Fig. B.1, was obtained by averaging the intensity within the selected boundary. For the case of the unswept plate, the estimated SNR was $0.46/0.195 = 2.36$. For the case of the swept plate, the estimated SNR was $0.60/0.26 = 2.3$.

Several factors in the Tomographic PIV setup will influence the estimated SNR of any volume reconstruction. This includes the aperture angle, β , seeding density, ppp , laser pulse energy and the correct raw image pre-processing settings. Any reader who wishes to attempt Tomographic PIV must pay critical attention to these parameters to ensure reconstruction of appropriate quality.

B.2 Quality of the vector calculation

To access the quality and accuracy of the resulting 3D velocity vector field of the VOI, the continuity equation as shown in Eq. B.2 for an incompressible fluid was verified to see if it holds within the VOI. The joint probability density functions (PDFs) of $\delta U_y/\delta y$ and $-(\delta U_x/\delta x + \delta U_z/\delta z)$ for the case of the unswept and swept plates are

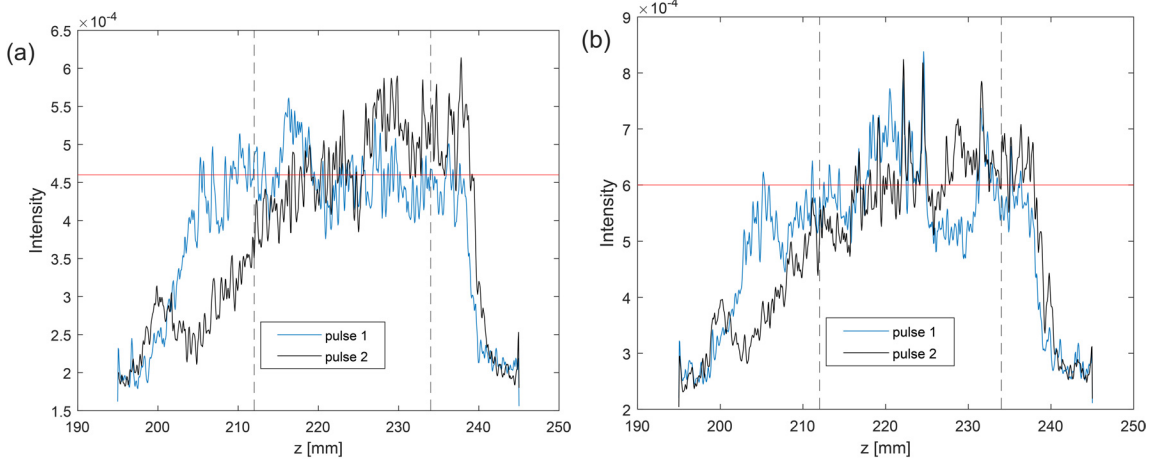


Figure B.1: Measured intensity by the dual-pulse laser across the reconstructed volume in the case of unswept plate ($\Lambda = 0^\circ$) (a) and swept plate ($\Lambda = 0^\circ$) (b).

shown in Fig. B.2 and Fig. B.3, respectively. The correlation coefficient, R^2 between the joint PDFs and the diagonal approaches 1.00 when Eq. B.2 is perfectly satisfied. Visually, this R^2 value would mean that all the contour lines in Fig. B.2 and Fig. B.3 fall right on the red diagonal line. Naturally, R^2 value of 1.00 is difficult to replicate in real-life scenarios.

$$\frac{\delta U_x}{\delta x} + \frac{\delta U_y}{\delta y} + \frac{\delta U_z}{\delta z} = 0 \quad (\text{B.2})$$

Here, the PDFs had the form of an ellipse shape. The calculated R^2 value varies for each z -plane vector field. The R^2 value seems to be closely related to the SNR of the volume reconstruction in Fig. B.1. The reconstruction quality at $z = 207$ mm was estimated to be of poor quality ($SNR < 2$) and was rejected to be included in the VOI. The poor quality of reconstruction was reflected in the R^2 values of their corresponding PDFs at 0.497 and 0.170, shown in Fig. B.2(a) and Fig. B.3(a) for the case of the unswept and swept plates, respectively.

If the contours form an elongated ellipse with its major axis aligning with the red diagonal line, a good correlation coefficient can be expected. Such was seen at the selected boundary of the VOI at $z = 213$ mm, shown in Fig. B.2(b) and Fig. B.3(b), where the R^2 values were 0.837 and 0.707 for the case of the unswept plate and swept plate, respectively. Figure B.2(c) and Fig. B.3(c) shows the averaged joint PDFs across the entire VOI thickness. The condition of $SNR \geq 2$ being the lower limit [77] is to be held strictly to preserve the subsequent quality of the vector calculation of the

volumetric reconstruction. An averaged R^2 values of 0.84 and 0.77 was achieved for the VOI of the unswept plate and swept plate, respectively, on par with the reported values by Casey et al. and Eshbal et al. [102] [103]. Thus, the calculated R^2 value assured the quality of the calculated vector field of the VOI in the present work. The quality of the vector field in any tomographic PIV work (including the present work) can be further improved by increasing the number of instantaneous velocity fields averaged. Reduction of the interrogation volume is also beneficial for the resulting correlation coefficient, but comes at the cost of decreased vector resolution.

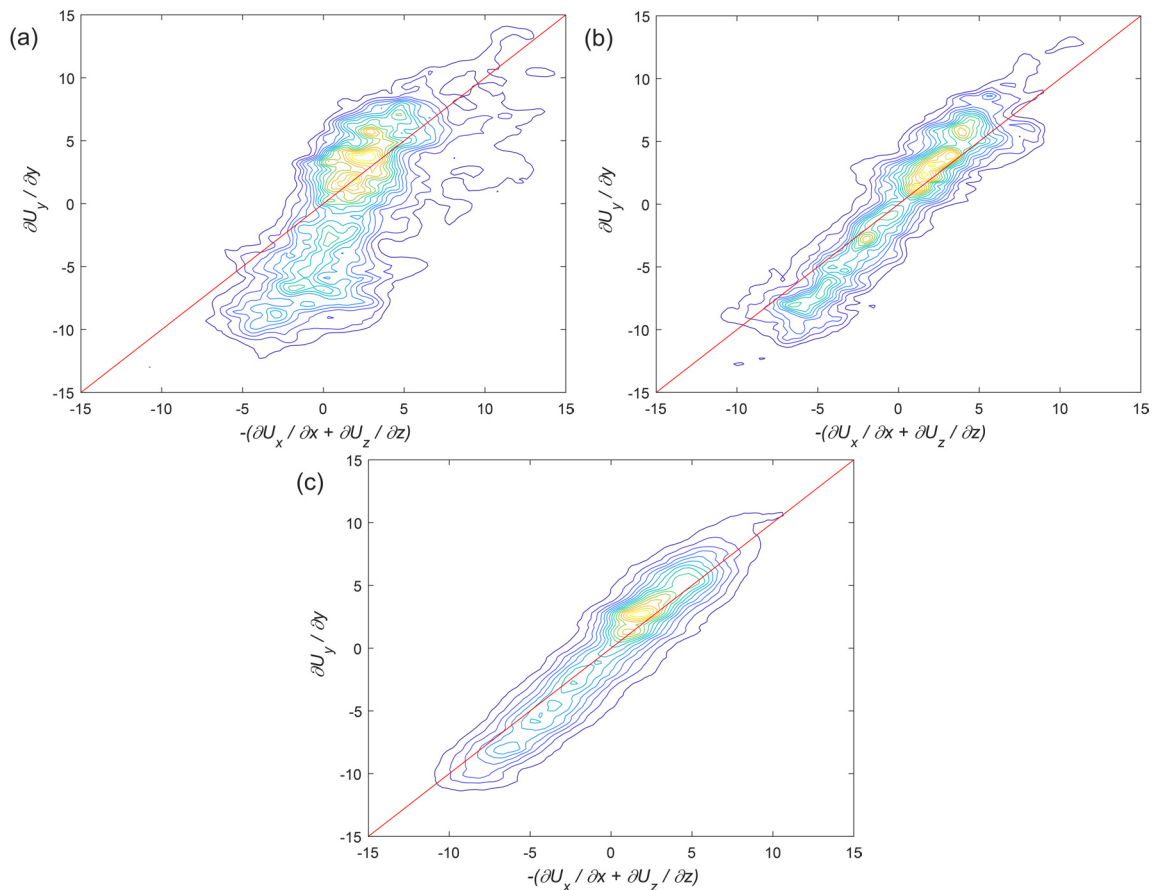


Figure B.2: Joint PDFs of the $\delta U_y/\delta y$ and $-(\delta U_x/\delta x + \delta U_z/\delta z)$ in the case of the unswept plate ($\Lambda = 0^\circ$) at $z = 207$ mm (a) and $z = 213$ mm (b), and averaged across the VOI (c). There are 15 contour levels.

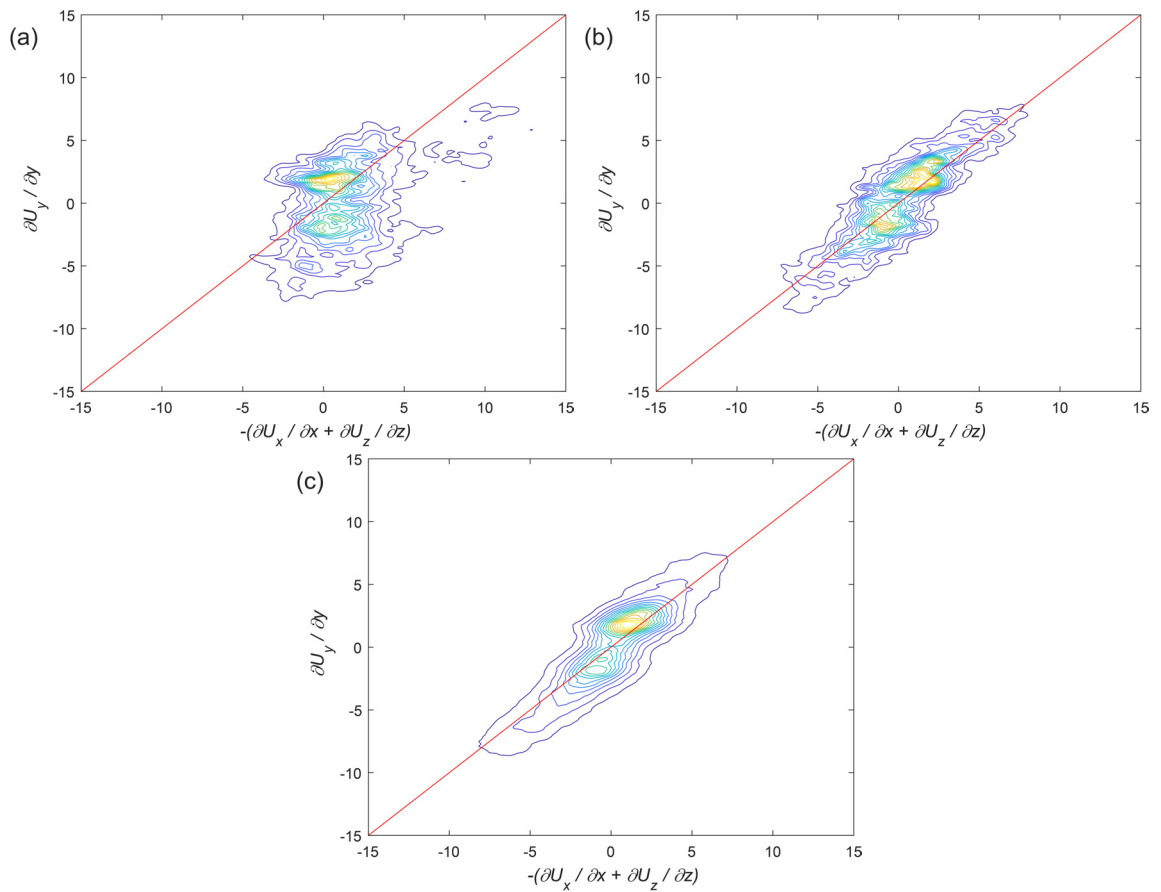


Figure B.3: Joint PDFs of the $\delta U_y / \delta y$ and $-(\delta U_x / \delta x + \delta U_z / \delta z)$ in the case of the swept plate ($\Lambda = 6^\circ$) at $z = 207$ mm (a) and $z = 213$ mm (b), and averaged across the VOI (c). There are 15 contour levels.

Appendix C

Illuminated region and the ghost intensity

Reiterating from the discussion above, on the assessment of the reconstructed quality in Appendix B.1, the reconstructed volume here had a thickness of 50 mm (an additional 10 mm on each side of the boundary), intentionally larger than the thickness of the DAV of 30 mm to capture the ghost particles outside the illuminated boundary. Figure C.1 and Fig. C.2 show examples of the x -normal and y -normal views of the volume reconstruction of each laser pulse, for the case of the unswept and swept plates, respectively. Here, the origin of the three-dimensional vortex structure described in Section 5.3, $z^* = 0.74$ corresponds to $z = 3$ mm.

Ghost particles are clearly defined here as particles outside of the illuminated region. They contributed to the ghost intensities, $I_{outsideVOI}$ used to calculate the SNR , defined in Eq. B.1. The decrease in intensity values seen in Fig. B.1 during the second pulse was related to the reflected light from the first pulse. Figure C.1(b) and Fig. C.2(b) clearly exhibit a substantial decrease in the thickness of the properly illuminated region during the second pulse, compared to the first pulse. The reflected light from the free surface and prototype components increased noise near the upper boundary of the reconstructed volume, leading to poor SNR values. As stated above, the VOI was selected where regions had $SNR \geq 2$. The selected VOI boundary corresponds to $z = -8$ mm \sim 14 mm with respect to Fig. C.1 and Fig. C.2, which lies within the properly illuminated region during both pulses.

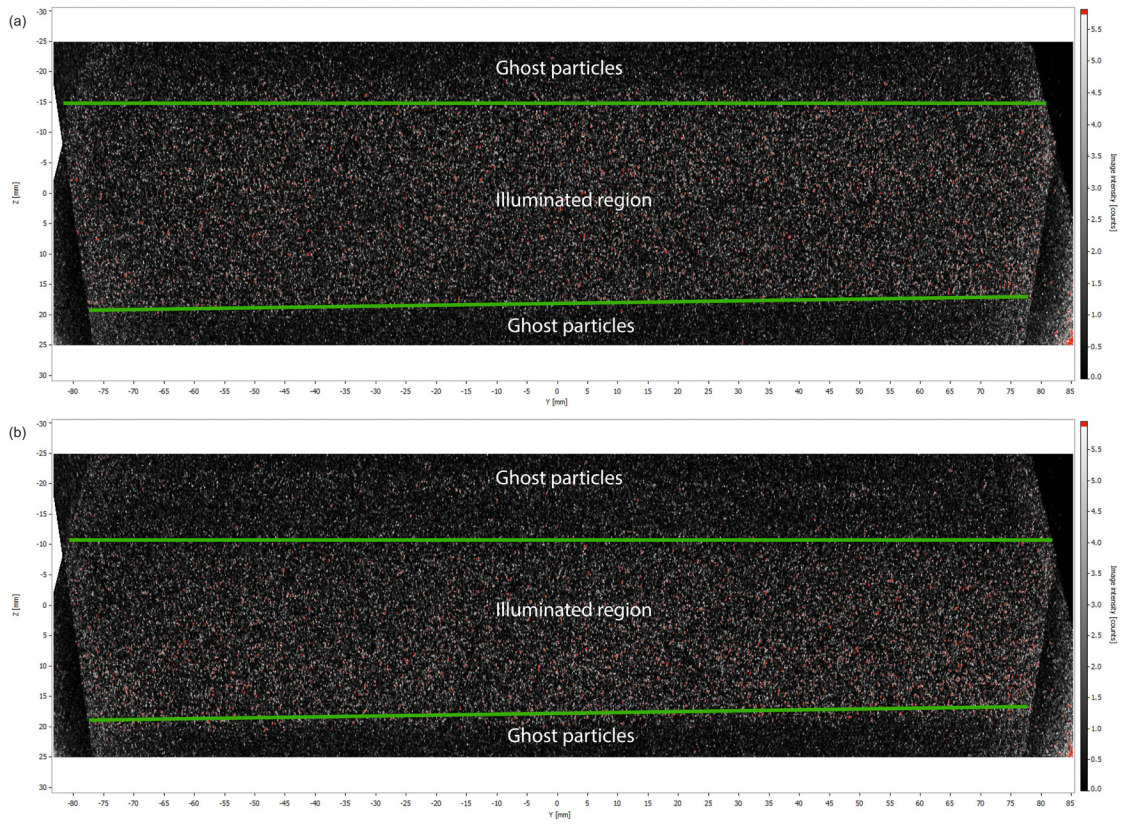


Figure C.1: An example of the x -normal view of the tomographic volume reconstruction at pulse 1 (a) and pulse 2 (b).

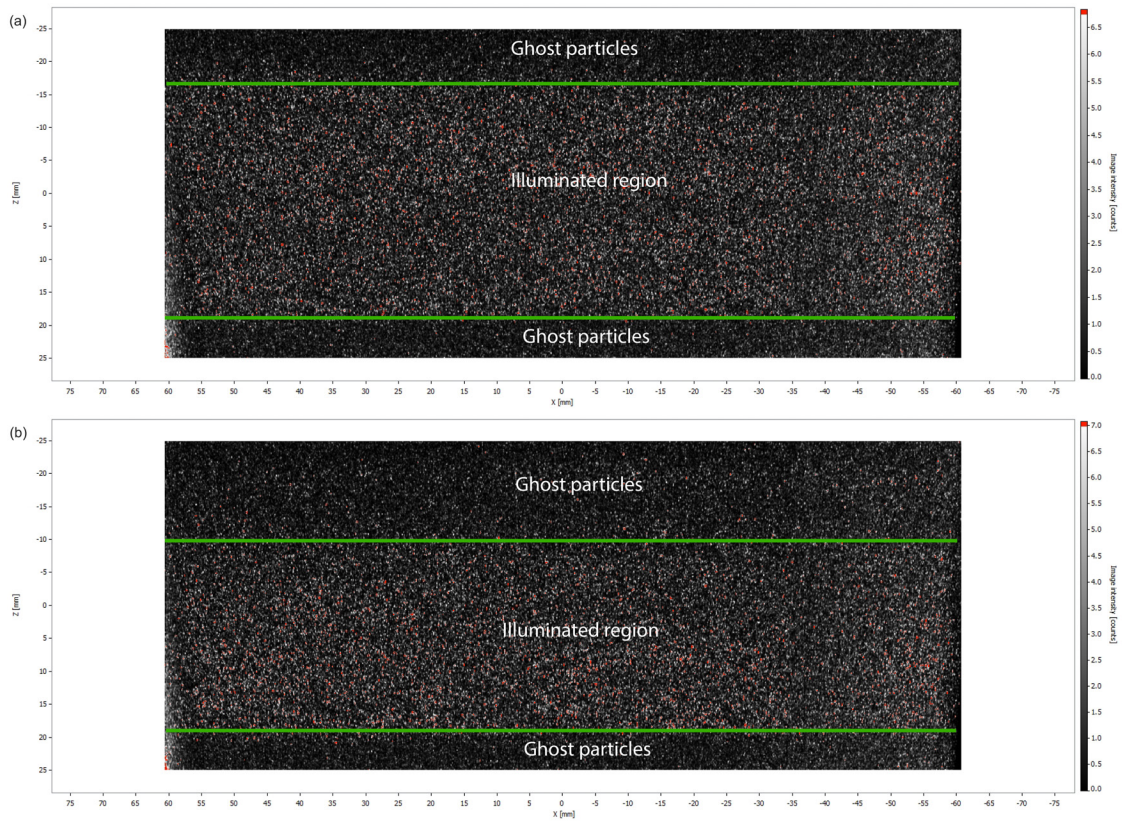


Figure C.2: An example of the y -normal view of the tomographic volume reconstruction at pulse 1 (a) and pulse 2 (b).

Appendix D

Influence of the bottom endplate

A three-dimensional wing with finite length has tip vortices due to the pressure difference between the suction side and the pressure side. The leading edge vortex creates a region of low pressure which promotes the transport of fluid from the pressure side, leading to the formation of a tip vortex. Tip vortex decreases the effective angle of attack of the wing, resulting in poor lift at the region of the tip. In the case of swept wings, the flow of fluid is induced in the spanwise component, amplifying the transport of fluid from the high pressure region to the low pressure region at the tip of the wing. Taking this phenomenon into consideration, it is then important to characterize the extent of the induced tip vortex effects in the present work. The spanwise flow component along the span of the blade was expected to induce tip vortices at the bottom tip of the plate. The relation of the tip losses to the energy extraction performance of the unswept and swept plates is investigated in this section.

The experiment was repeated at the baseline case ($Re = 19\ 000$) to observe the effects on the energy extraction performance of the fully-passive oscillating-plate without the bottom endplate. All structural parameters were kept constant, with reference to the normalized structural parameters of the baseline case mentioned in Section 4.1. Table D.1 summarises the results of the unswept plate and the swept plate, with and without the attachment of the bottom endplate. As mentioned, the results for the equivalent baseline cases (attached bottom endplate) were plotted in Fig. 4.1 as a reference to the repeatability of the kinematic and performance parameters. The standard deviations of the kinematic and performance parameters of the data presented in Table D.1 are provided in Appendix E.

In the case of the unswept plate, the bottom endplate did not significantly affect the kinematic and performance parameters. A relative drop of 6% on the efficiency

was observed during the absence of the bottom endplate. Slight variation in the power coefficient was also observed but not much greater than its standard deviation. Similar to a finite-span rectangular wing, the pressure distribution along the span of the unswept plate is not uniform. According to the simulations done by Kinsey and Dumas [61], and Villeneuve et al. [83], vortex generation is expected to be strongest around the mid span and proceeds to grow much weaker near the tip. By removing the bottom endplate, only the local pressure distribution near the vicinity of the bottom tip was affected, which accounted for relatively little on the overall forces acting on the plate. The prior explains the small consequence the bottom endplate had to the overall energy extraction performance of the unswept plate.

Table D.1: Kinematic and performance parameters of the plates, with and without the presence of the bottom endplate. The initial and final viscous damping and coulomb friction of each series of test were: $D_{h,v}^* = [0.09 - 0.11]$; $D_{\theta}^* = [0.007 - 0.005]$; $C_{FyCoulomb} = [0.03 - 0.01]$; $C_{MCoulomb} = [0.01 - 0.01]$ and $D_{h,v}^* = [0.10 - 0.13]$; $D_{\theta}^* = [0.018 - 0.007]$; $C_{FyCoulomb} = [0.03 - 0.05]$; $C_{MCoulomb} = [0.02 - 0.01]$ for the unswept plate ($\Lambda = 0^\circ$) and swept plate ($\Lambda = 6^\circ$), respectively.

$\Lambda [^\circ]$	Bottom endplate	f^*	$\phi [^\circ]$	H_0^*	$P_0 [^\circ]$	η	C_p
0	yes	0.148	84.9	0.980	82.3	22.1	0.614
Normalized Values							
0	yes	1	1	1	1	1	1
0	no	0.95	1.12	1	0.90	1.03	0.94
6	yes	0.90	1.19	1.04	0.89	1.01	0.92
6	no	0	0	0	0	0	0

On the contrary, the swept plate was not able to achieve sustainable oscillation without the bottom endplate. Any initial perturbation introduced to excite the plate did not help as well. The same occurred for any inflow velocity. This observation suggests that when the bottom endplate was attached, the local pressure distribution near the vicinity of the bottom tip accounts for most of the overall forces acting on the swept plate. The spanwise flow component transported vorticity towards the tip where they concentrate. Without a blockade, the concentrated low pressure region induced strong tip vortex, significantly decreasing the local effective angle of attack. The tip vortex inhibited the initial growth potential of the vortex along the leading edge of the swept plate, which reduced the instantaneous force experienced to initiate the onset of stable oscillation at earlier phases of the cycle. This series of events

prevented any sustainable oscillation from occurring. The results suggest that any fully-passive oscillating-plate device with sweep angle will rely on bottom endplates to prevent significant tip losses due to the spanwise flow, especially for plates of lower aspect ratios, such as the plates in present work, where $b/c = 5$.

Appendix E

Standard deviations of the kinematic and performance parameters

The time evolution of the normalized heave position and pitch position of the unswept plate over 10 cycles are shown in Fig. E.1(a) and Fig. E.1(b), respectively. The figures provide the reader a sense of the motions of the oscillating-plate and the respective variation between each oscillation cycle.

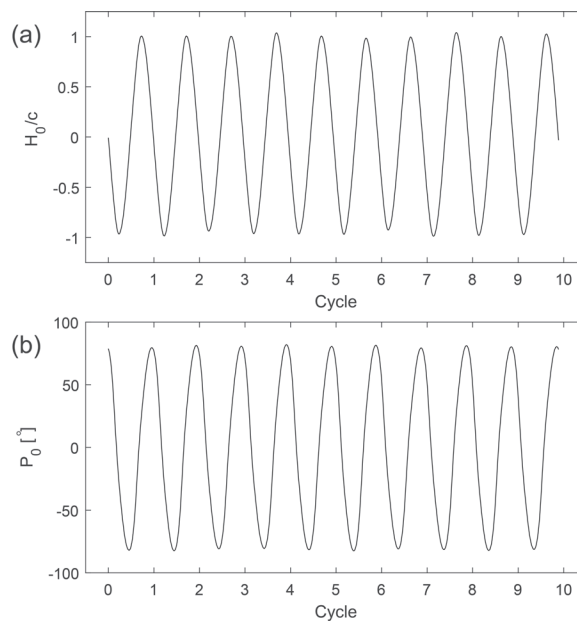


Figure E.1: Time evolution of the normalized heave (a) and pitch (b) positions of the unswept plate ($\Lambda = 0^\circ$) over 10 cycles at $U_\infty = 0.452$ m/s.

The standard deviations of the calculated kinematic and performance parameters over 90 oscillation cycles for each case presented in the present work are listed here. The standard deviations at each inflow velocity in Table E.1 and Table E.2 refer to the results of the effects of the inflow velocity on the turbine performance, discussed in Section 4.2. Table E.3 summarizes the standard deviations for the cases on the influence of the bottom endplate, discussed in Appendix D.

Table E.1: Standard deviations of the kinematic and performance parameters of the unswept plate ($\Lambda = 0^\circ$), presented in Fig 4.1.

U_∞ [ms^{-1}]	Standard deviation					
	C_p	η	H_0^*	P_0	f	ϕ
0.302	0.018	0.006	0.012	0.897	0.007	2.33
0.347	0.021	0.006	0.012	0.761	0.011	2.21
0.368	0.012	0.003	0.010	0.655	0.011	2.50
0.411	0.014	0.004	0.014	0.525	0.014	2.60
0.452	0.012	0.003	0.020	0.568	0.019	2.68
0.494	0.011	0.002	0.020	0.522	0.019	2.80
0.544	0.007	0.002	0.016	0.367	0.021	2.80
0.597	0.004	0.001	0.011	0.333	0.022	3.33

Table E.2: Standard deviations of the kinematic and performance parameters of the swept plate ($\Lambda = 6^\circ$), presented in Fig 4.1.

U_∞ [ms^{-1}]	Standard deviation					
	C_p	η	H_0^*	P_0	f	ϕ
0.302	0	0	0	0	0	0
0.347	0.021	0.006	0.016	0.917	0.007	2.49
0.368	0.021	0.005	0.016	0.796	0.007	2.55
0.411	0.021	0.004	0.016	0.848	0.008	2.21
0.452	0.020	0.004	0.016	0.850	0.009	2.46
0.494	0.034	0.006	0.022	1.902	0.018	3.65

Table E.3: Standard deviations of the kinematic and performance parameters of the plates, with and without the attachment of the bottom endplate, presented in Table D.1.

$\wedge[^\circ]$	Bottom endplate	Standard deviation					
		C_p	η	H_0^*	P_0	f	ϕ
0	yes	0.013	0.003	0.008	0.812	0.012	2.90
0	no	0.019	0.004	0.014	0.874	0.008	2.61
6	yes	0.019	0.005	0.015	0.868	0.007	2.34

Bibliography

- [1] M. Ram, M. Child, A. Aghahosseini, D. Bogdanov, A. Lohrmann, and C. Breyer, “A comparative analysis of electricity generation costs from renewable, fossil fuel and nuclear sources in g20 countries for the period 2015-2030,” *Journal of Cleaner Production*, vol. 199, pp. 687–704, Oct. 2018. [Online]. Available: <https://doi.org/10.1016/j.jclepro.2018.07.159>
- [2] M. Höök and X. Tang, “Depletion of fossil fuels and anthropogenic climate change—a review,” *Energy Policy*, vol. 52, pp. 797–809, Jan. 2013. [Online]. Available: <https://doi.org/10.1016/j.enpol.2012.10.046>
- [3] J. Rogelj, M. den Elzen, N. Höhne, T. Fransen, H. Fekete, H. Winkler, R. Schaeffer, F. Sha, K. Riahi, and M. Meinshausen, “Paris agreement climate proposals need a boost to keep warming well below 2 °c,” *Nature*, vol. 534, no. 7609, pp. 631–639, Jun. 2016. [Online]. Available: <https://doi.org/10.1038/nature18307>
- [4] I. Dincer, “Renewable energy and sustainable development: a crucial review,” *Renewable and Sustainable Energy Reviews*, vol. 4, no. 2, pp. 157–175, Jun. 2000. [Online]. Available: [https://doi.org/10.1016/s1364-0321\(99\)00011-8](https://doi.org/10.1016/s1364-0321(99)00011-8)
- [5] G. Saini and R. P. Saini, “A review on technology, configurations, and performance of cross-flow hydrokinetic turbines,” *International Journal of Energy Research*, Jun. 2019. [Online]. Available: <https://doi.org/10.1002/er.4625>
- [6] D. Jiyun, Y. Hongxing, S. Zhicheng, and G. Xiaodong, “Development of an inline vertical cross-flow turbine for hydropower harvesting in urban water supply pipes,” *Renewable Energy*, vol. 127, pp. 386–397, Nov. 2018. [Online]. Available: <https://doi.org/10.1016/j.renene.2018.04.070>

- [7] L. L. Ladokun, B. F. Sule, K. R. Ajao, and A. G. Adeogun, "Resource assessment and feasibility study for the generation of hydrokinetic power in the tailwaters of selected hydropower stations in nigeria," *Water Science*, vol. 32, no. 2, pp. 338–354, Oct. 2018. [Online]. Available: <https://doi.org/10.1016/j.wsj.2018.05.003>
- [8] Hydro-Québec. (2015) Renewable energy option: Hydrokinetic power. [Online]. Available: <http://www.hydroquebec.com/sustainable-development/documentation-center/hydrokinetic-power.html>
- [9] M. Khan, G. Bhuyan, M. Iqbal, and J. Quaicoe, "Hydrokinetic energy conversion systems and assessment of horizontal and vertical axis turbines for river and tidal applications: A technology status review," *Applied Energy*, vol. 86, no. 10, pp. 1823–1835, Oct. 2009. [Online]. Available: <https://doi.org/10.1016/j.apenergy.2009.02.017>
- [10] M. Güney and K. Kaygusuz, "Hydrokinetic energy conversion systems: A technology status review," *Renewable and Sustainable Energy Reviews*, vol. 14, no. 9, pp. 2996–3004, Dec. 2010. [Online]. Available: <https://doi.org/10.1016/j.rser.2010.06.016>
- [11] A. Kumar and R. Saini, "Performance parameters of savonius type hydrokinetic turbine – a review," *Renewable and Sustainable Energy Reviews*, vol. 64, pp. 289–310, Oct. 2016. [Online]. Available: <https://doi.org/10.1016/j.rser.2016.06.005>
- [12] M. Boudreau and G. Dumas, "Comparison of the wake recovery of the axial-flow and cross-flow turbine concepts," *Journal of Wind Engineering and Industrial Aerodynamics*, vol. 165, pp. 137–152, Jun. 2017. [Online]. Available: <https://doi.org/10.1016/j.jweia.2017.03.010>
- [13] B. Yang and X. Shu, "Hydrofoil optimization and experimental validation in helical vertical axis turbine for power generation from marine current," *Ocean Engineering*, vol. 42, pp. 35–46, Mar. 2012. [Online]. Available: <https://doi.org/10.1016/j.oceaneng.2012.01.004>
- [14] R. Gosselin, G. Dumas, and M. Boudreau, "Parametric study of h-darrieus vertical-axis turbines using CFD simulations," *Journal of Renewable and*

- Sustainable Energy*, vol. 8, no. 5, p. 053301, Sep. 2016. [Online]. Available: <https://doi.org/10.1063/1.4963240>
- [15] A. N. Gorban', A. M. Gorlov, and V. M. Silantyev, "Limits of the turbine efficiency for free fluid flow," *Journal of Energy Resources Technology*, vol. 123, no. 4, pp. 311–317, Aug. 2001. [Online]. Available: <https://doi.org/10.1115/1.1414137>
- [16] J. Hildebrand, "Anthropogenic and natural sources of ambient noise in the ocean," *Marine Ecology Progress Series*, vol. 395, pp. 5–20, Dec. 2009. [Online]. Available: <https://doi.org/10.3354/meps08353>
- [17] P. R. Bandyopadhyay, "Swimming and flying in nature—the route toward applications: The freeman scholar lecture," *Journal of Fluids Engineering*, vol. 131, no. 3, Feb. 2009. [Online]. Available: <https://doi.org/10.1115/1.3063687>
- [18] T. Maxworthy, "Experiments on the weis-fogh mechanism of lift generation by insects in hovering flight. part 1. dynamics of the 'fling'," *Journal of Fluid Mechanics*, vol. 93, no. 1, pp. 47–63, Jul. 1979. [Online]. Available: <https://doi.org/10.1017/s0022112079001774>
- [19] D. Weihs, "Stability versus maneuverability in aquatic locomotion," *Integrative and Comparative Biology*, vol. 42, no. 1, pp. 127–134, Feb. 2002. [Online]. Available: <https://doi.org/10.1093/icb/42.1.127>
- [20] J. Young, J. C. Lai, and M. F. Platzer, "A review of progress and challenges in flapping foil power generation," *Progress in Aerospace Sciences*, vol. 67, pp. 2–28, May 2014. [Online]. Available: <https://doi.org/10.1016/j.paerosci.2013.11.001>
- [21] X. Wu, X. Zhang, X. Tian, X. Li, and W. Lu, "A review on fluid dynamics of flapping foils," *Ocean Engineering*, vol. 195, p. 106712, Jan. 2020. [Online]. Available: <https://doi.org/10.1016/j.oceaneng.2019.106712>
- [22] K. Harper, M. Berkemeier, and S. Grace, "Modeling the dynamics of spring-driven oscillating-foil propulsion," *IEEE Journal of Oceanic Engineering*, vol. 23, no. 3, pp. 285–296, Jul. 1998. [Online]. Available: <https://doi.org/10.1109/48.701206>

- [23] P. R. Bandyopadhyay, “Maneuvering hydrodynamics of fish and small underwater vehicles,” *Integrative and Comparative Biology*, vol. 42, no. 1, pp. 102–117, Feb. 2002. [Online]. Available: <https://doi.org/10.1093/icb/42.1.102>
- [24] D. Barrett, M. Grosenbaugh, and M. Triantafyllou, “The optimal control of a flexible hull robotic undersea vehicle propelled by an oscillating foil,” in *Proceedings of Symposium on Autonomous Underwater Vehicle Technology*. IEEE, 1996. [Online]. Available: <https://doi.org/10.1109/auv.1996.532833>
- [25] W. McKinney and J. DeLaurier, “Wingmill: An oscillating-wing windmill,” *Journal of Energy*, vol. 5, no. 2, pp. 109–115, Mar. 1981. [Online]. Available: <https://doi.org/10.2514/3.62510>
- [26] Q. Xiao and Q. Zhu, “A review on flow energy harvesters based on flapping foils,” *Journal of Fluids and Structures*, vol. 46, pp. 174–191, Apr. 2014. [Online]. Available: <https://doi.org/10.1016/j.jfluidstructs.2014.01.002>
- [27] K. D. Jones, K. Lindsey, and M. F. Platzer, “An investigation of the fluid-structure interaction in an oscillating-wing micro-hydropower generator,” *Transactions on the Built Environment*, vol. 46, pp. 174–191, 2004.
- [28] T. Kinsey and G. Dumas, “Parametric study of an oscillating airfoil in a power-extraction regime,” *AIAA Journal*, vol. 46, no. 6, pp. 1318–1330, Jun. 2008. [Online]. Available: <https://doi.org/10.2514/1.26253>
- [29] —, “Optimal tandem configuration for oscillating-foils hydrokinetic turbine,” *Journal of Fluids Engineering*, vol. 134, no. 3, Mar. 2012. [Online]. Available: <https://doi.org/10.1115/1.4005423>
- [30] J. Xu, H. Sun, and S. Tan, “Wake vortex interaction effects on energy extraction performance of tandem oscillating hydrofoils,” *Journal of Mechanical Science and Technology*, vol. 30, no. 9, pp. 4227–4237, Sep. 2016. [Online]. Available: <https://doi.org/10.1007/s12206-016-0835-9>
- [31] G. D. Xu and W. H. Xu, “Energy extraction of two flapping foils with tandem configurations and vortex interactions,” *Engineering Analysis with Boundary Elements*, vol. 82, pp. 202–209, Sep. 2017. [Online]. Available: <https://doi.org/10.1016/j.enganabound.2017.06.010>

- [32] T. E. B. Ltd., “Stingray tidal stream energy device - phase 3,” *Crown copyright 2005*, 2005.
- [33] T. Kinsey, G. Dumas, G. Lalande, J. Ruel, A. Méhut, P. Viarouge, J. Lemay, and Y. Jean, “Prototype testing of a hydrokinetic turbine based on oscillating hydrofoils,” *Renewable Energy*, vol. 36, no. 6, pp. 1710–1718, Jun. 2011. [Online]. Available: <https://doi.org/10.1016/j.renene.2010.11.037>
- [34] H. Abiru and A. Yoshitake, “Study on a flapping wing hydroelectric power generation system,” *Journal of Environment and Engineering*, vol. 6, no. 1, pp. 178–186, 2011. [Online]. Available: <https://doi.org/10.1299/jee.6.178>
- [35] T. Kinsey and G. Dumas, “Optimal operating parameters for an oscillating foil turbine at reynolds number 500, 000,” *AIAA Journal*, vol. 52, no. 9, pp. 1885–1895, Sep. 2014. [Online]. Available: <https://doi.org/10.2514/1.j052700>
- [36] J. Deng, L. Teng, D. Pan, and X. Shao, “Inertial effects of the semi-passive flapping foil on its energy extraction efficiency,” *Physics of Fluids*, vol. 27, no. 5, p. 053103, May 2015. [Online]. Available: <https://doi.org/10.1063/1.4921384>
- [37] L. Teng, J. Deng, D. Pan, and X. Shao, “Effects of non-sinusoidal pitching motion on energy extraction performance of a semi-active flapping foil,” *Renewable Energy*, vol. 85, pp. 810–818, Jan. 2016. [Online]. Available: <https://doi.org/10.1016/j.renene.2015.07.037>
- [38] M. Boudreau, K. Gunther, and G. Dumas, “Investigation of the energy-extraction regime of a novel semi-passive flapping-foil turbine concept with a prescribed heave motion and a passive pitch motion,” *Journal of Fluids and Structures*, vol. 84, pp. 368–390, Jan. 2019. [Online]. Available: <https://doi.org/10.1016/j.jfluidstructs.2018.11.014>
- [39] D. Poirel, Y. Harris, and A. Benaïssa, “Self-sustained aeroelastic oscillations of a NACA0012 airfoil at low-to-moderate reynolds numbers,” *Journal of Fluids and Structures*, vol. 24, no. 5, pp. 700–719, Jul. 2008. [Online]. Available: <https://doi.org/10.1016/j.jfluidstructs.2007.11.005>
- [40] Z. Peng and Q. Zhu, “Energy harvesting through flow-induced oscillations of a foil,” *Physics of Fluids*, vol. 21, no. 12, p. 123602, Dec. 2009. [Online]. Available: <https://doi.org/10.1063/1.3275852>

- [41] Q. Zhu, “Energy harvesting by a purely passive flapping foil from shear flows,” *Journal of Fluids and Structures*, vol. 34, pp. 157–169, Oct. 2012. [Online]. Available: <https://doi.org/10.1016/j.jfluidstructs.2012.05.013>
- [42] Z. Wang, L. Du, J. Zhao, and X. Sun, “Structural response and energy extraction of a fully passive flapping foil,” *Journal of Fluids and Structures*, vol. 72, pp. 96–113, Jul. 2017. [Online]. Available: <https://doi.org/10.1016/j.jfluidstructs.2017.05.002>
- [43] L. Duarte, N. Dellinger, G. Dellinger, A. Ghenaim, and A. Terfous, “Experimental investigation of the dynamic behaviour of a fully passive flapping foil hydrokinetic turbine,” *Journal of Fluids and Structures*, vol. 88, pp. 1–12, Jul. 2019. [Online]. Available: <https://doi.org/10.1016/j.jfluidstructs.2019.04.012>
- [44] M. Boudreau, G. Dumas, M. Rahimpour, and P. Oshkai, “Experimental investigation of the energy extraction by a fully-passive flapping-foil hydrokinetic turbine prototype,” *Journal of Fluids and Structures*, vol. 82, pp. 446–472, Oct. 2018. [Online]. Available: <https://doi.org/10.1016/j.jfluidstructs.2018.07.014>
- [45] Q. Zhu, “Optimal frequency for flow energy harvesting of a flapping foil,” *Journal of Fluid Mechanics*, vol. 675, pp. 495–517, Mar. 2011. [Online]. Available: <https://doi.org/10.1017/s0022112011000334>
- [46] J.-C. Veilleux and G. Dumas, “Numerical optimization of a fully-passive flapping-airfoil turbine,” *Journal of Fluids and Structures*, vol. 70, pp. 102–130, Apr. 2017. [Online]. Available: <https://doi.org/10.1016/j.jfluidstructs.2017.01.019>
- [47] Q. Xiao, W. Liao, S. Yang, and Y. Peng, “How motion trajectory affects energy extraction performance of a biomimic energy generator with an oscillating foil?” *Renewable Energy*, vol. 37, no. 1, pp. 61–75, Jan. 2012. [Online]. Available: <https://doi.org/10.1016/j.renene.2011.05.029>
- [48] J.-C. Veilleux, “Optimization of a fully-passive flapping-airfoil turbine,” *Master’s thesis, Dept. of Mechanical Engineering, Laval University, Quebec, Canada*, 2014.

- [49] M. Boudreau, M. Picard-Deland, and G. Dumas, “A parametric study and optimization of the fully-passive flapping-foil turbine at high reynolds number,” *Renewable Energy*, vol. 146, pp. 1958–1975, Feb. 2020. [Online]. Available: <https://doi.org/10.1016/j.renene.2019.08.013>
- [50] J. D. Eldredge and A. R. Jones, “Leading-edge vortices: Mechanics and modeling,” *Annual Review of Fluid Mechanics*, vol. 51, no. 1, pp. 75–104, Jan. 2019. [Online]. Available: <https://doi.org/10.1146/annurev-fluid-010518-040334>
- [51] T. Q. Le and J. H. Ko, “Effect of hydrofoil flexibility on the power extraction of a flapping tidal generator via two- and three-dimensional flow simulations,” *Renewable Energy*, vol. 80, pp. 275–285, Aug. 2015. [Online]. Available: <https://doi.org/10.1016/j.renene.2015.01.068>
- [52] W. Liu, Q. Xiao, and Q. Zhu, “Passive flexibility effect on oscillating foil energy harvester,” *AIAA Journal*, vol. 54, no. 4, pp. 1172–1187, Apr. 2016. [Online]. Available: <https://doi.org/10.2514/1.j054205>
- [53] F. Siala and J. A. Liburdy, “Energy harvesting of a heaving and forward pitching wing with a passively actuated trailing edge,” *Journal of Fluids and Structures*, vol. 57, pp. 1–14, Aug. 2015. [Online]. Available: <https://doi.org/10.1016/j.jfluidstructs.2015.05.007>
- [54] A. D. Totpal, F. F. Siala, and J. A. Liburdy, “Energy harvesting of an oscillating foil at low reduced frequencies with rigid and passively deforming leading edge,” *Journal of Fluids and Structures*, vol. 82, pp. 329–342, Oct. 2018. [Online]. Available: <https://doi.org/10.1016/j.jfluidstructs.2018.04.022>
- [55] M. D. Griffith, D. L. Jacono, J. Sheridan, and J. S. Leontini, “Passive heaving of elliptical cylinders with active pitching – from cylinders towards flapping foils,” *Journal of Fluids and Structures*, vol. 67, pp. 124–141, Nov. 2016. [Online]. Available: <https://doi.org/10.1016/j.jfluidstructs.2016.09.005>
- [56] C. O. Usoh, J. Young, J. C. S. Lai, and M. A. Ashraf, “Numerical analysis of a non-profiled plate for flapping wing turbines,” *Proceedings of the 18th Australasian Fluid Mechanics Conference, AFMC 2012*, 2012.

- [57] A. Boudis, A. Benzaoui, H. Oualli, O. Guerri, A. C. Bayeul-Lainé, and O. C. Delgosha, “Energy extraction performance improvement of a flapping foil by the use of combined foil,” *Journal of Applied Fluid Mechanics*, vol. 11, no. 6, pp. 1651–1663, Nov. 2018. [Online]. Available: <https://doi.org/10.29252/jafm.11.06.29099>
- [58] B. Zhu, Y. Huang, and Y. Zhang, “Energy harvesting properties of a flapping wing with an adaptive gurney flap,” *Energy*, vol. 152, pp. 119–128, Jun. 2018. [Online]. Available: <https://doi.org/10.1016/j.energy.2018.03.142>
- [59] M. T. Bouzaher, N. Drias, and B. Guerira, “Improvement of energy extraction efficiency for flapping airfoils by using oscillating gurney flaps,” *Arabian Journal for Science and Engineering*, vol. 44, no. 2, pp. 809–819, May 2018. [Online]. Available: <https://doi.org/10.1007/s13369-018-3270-7>
- [60] M. M. Qadri, F. Zhao, and H. Tang, “Fluid-structure interaction of a fully passive flapping foil for flow energy extraction,” *International Journal of Mechanical Sciences*, vol. 177, p. 105587, Jul. 2020. [Online]. Available: <https://doi.org/10.1016/j.ijmecsci.2020.105587>
- [61] T. Kinsey and G. Dumas, “Three-dimensional effects on an oscillating-foil hydrokinetic turbine,” *Journal of Fluids Engineering*, vol. 134, no. 7, Jun. 2012. [Online]. Available: <https://doi.org/10.1115/1.4006914>
- [62] D. Kim, B. Strom, S. Mandre, and K. Breuer, “Energy harvesting performance and flow structure of an oscillating hydrofoil with finite span,” *Journal of Fluids and Structures*, vol. 70, pp. 314–326, Apr. 2017. [Online]. Available: <https://doi.org/10.1016/j.jfluidstructs.2017.02.004>
- [63] D. McLean, *Understanding Aerodynamics: Arguing from the Real Physics*. John Wiley and Sons, 2013.
- [64] C. P. Ellington, C. van den Berg, A. P. Willmott, and A. L. R. Thomas, “Leading-edge vortices in insect flight,” *Nature*, vol. 384, no. 6610, pp. 626–630, Dec. 1996. [Online]. Available: <https://doi.org/10.1038/384626a0>
- [65] J. M. Birch and M. H. Dickinson, “Spanwise flow and the attachment of the leading-edge vortex on insect wings,” *Nature*, vol. 412, no. 6848, pp. 729–733, Aug. 2001. [Online]. Available: <https://doi.org/10.1038/35089071>

- [66] D. Lentink and M. H. Dickinson, “Rotational accelerations stabilize leading edge vortices on revolving fly wings,” *Journal of Experimental Biology*, vol. 212, no. 16, pp. 2705–2719, Jul. 2009. [Online]. Available: <https://doi.org/10.1242/jeb.022269>
- [67] J. Wu, A. Vakili, and J. Wu, “Review of the physics of enhancing vortex lift by unsteady excitation,” *Progress in Aerospace Sciences*, vol. 28, no. 2, pp. 73–131, Jan. 1991. [Online]. Available: [https://doi.org/10.1016/0376-0421\(91\)90001-k](https://doi.org/10.1016/0376-0421(91)90001-k)
- [68] J. G. Wong, J. Kriegseis, and D. E. Rival, “An investigation into vortex growth and stabilization for two-dimensional plunging and flapping plates with varying sweep,” *Journal of Fluids and Structures*, vol. 43, pp. 231–243, Nov. 2013. [Online]. Available: <https://doi.org/10.1016/j.jfluidstructs.2013.09.010>
- [69] I. Borazjani and M. Daghooghi, “The fish tail motion forms an attached leading edge vortex,” *Proceedings of the Royal Society B: Biological Sciences*, vol. 280, no. 1756, p. 20122071, Apr. 2013. [Online]. Available: <https://doi.org/10.1098/rspb.2012.2071>
- [70] T. Jardin and L. David, “Spanwise gradients in flow speed help stabilize leading-edge vortices on revolving wings,” *Physical Review E*, vol. 90, no. 1, Jul. 2014. [Online]. Available: <https://doi.org/10.1103/physreve.90.013011>
- [71] J. G. Wong and D. E. Rival, “Determining the relative stability of leading-edge vortices on nominally two-dimensional flapping profiles,” *Journal of Fluid Mechanics*, vol. 766, pp. 611–625, Feb. 2015. [Online]. Available: <https://doi.org/10.1017/jfm.2015.39>
- [72] B. Cheng, S. P. Sane, G. Barbera, D. R. Troolin, T. Strand, and X. Deng, “Three-dimensional flow visualization and vorticity dynamics in revolving wings,” *Experiments in Fluids*, vol. 54, no. 1, Jan. 2013. [Online]. Available: <https://doi.org/10.1007/s00348-012-1423-0>
- [73] C. J. Wojcik and J. H. J. Buchholz, “Vorticity transport in the leading-edge vortex on a rotating blade,” *Journal of Fluid Mechanics*, vol. 743, pp. 249–261, Mar. 2014. [Online]. Available: <https://doi.org/10.1017/jfm.2014.18>
- [74] H. R. Beem, D. E. Rival, and M. S. Triantafyllou, “On the stabilization of leading-edge vortices with spanwise flow,” *Experiments in Fluids*,

- vol. 52, no. 2, pp. 511–517, Dec. 2011. [Online]. Available: <https://doi.org/10.1007/s00348-011-1241-9>
- [75] LaVision, *FlowMaster*, item-number(s): 1105011-4 ed., 2018.
- [76] S. Ghaemi and F. Scarano, “Counter-hairpin vortices in the turbulent wake of a sharp trailing edge,” *Journal of Fluid Mechanics*, vol. 689, pp. 317–356, Nov. 2011. [Online]. Available: <https://doi.org/10.1017/jfm.2011.431>
- [77] F. Scarano, “Tomographic PIV: principles and practice,” *Measurement Science and Technology*, vol. 24, no. 1, p. 012001, Oct. 2012. [Online]. Available: <https://doi.org/10.1088/0957-0233/24/1/012001>
- [78] G. E. Elsinga, F. Scarano, B. Wieneke, and B. W. van Oudheusden, “Tomographic particle image velocimetry,” *Experiments in Fluids*, vol. 41, no. 6, pp. 933–947, Oct. 2006. [Online]. Available: <https://doi.org/10.1007/s00348-006-0212-z>
- [79] LaVision, *FlowMaster Tomographic PIV*, item-number(s): 1105032 ed., 2020.
- [80] G. T. Herman and A. Lent, “Iterative reconstruction algorithms,” *Computers in Biology and Medicine*, vol. 6, no. 4, pp. 273–294, Oct. 1976. [Online]. Available: [https://doi.org/10.1016/0010-4825\(76\)90066-4](https://doi.org/10.1016/0010-4825(76)90066-4)
- [81] M. Picard-Deland, M. Olivier, G. Dumas, and T. Kinsey, “Oscillating-foil turbine operating at large heaving amplitudes,” *AIAA Journal*, vol. 57, no. 12, pp. 5104–5113, Dec. 2019. [Online]. Available: <https://doi.org/10.2514/1.j058505>
- [82] D. Read, F. Hover, and M. Triantafyllou, “Forces on oscillating foils for propulsion and maneuvering,” *Journal of Fluids and Structures*, vol. 17, no. 1, pp. 163–183, Jan. 2003. [Online]. Available: [https://doi.org/10.1016/s0889-9746\(02\)00115-9](https://doi.org/10.1016/s0889-9746(02)00115-9)
- [83] T. Villeneuve, M. Boudreau, and G. Dumas, “Lift enhancement and drag reduction of lifting blades through the use of end-plates and detached end-plates,” *Journal of Wind Engineering and Industrial Aerodynamics*, vol. 184, pp. 391–404, Jan. 2019. [Online]. Available: <https://doi.org/10.1016/j.jweia.2018.12.006>

- [84] T. L. Doligalski, C. R. Smith, and J. D. A. Walker, “Vortex interactions with walls,” *Annual Review of Fluid Mechanics*, vol. 26, no. 1, pp. 573–616, Jan. 1994. [Online]. Available: <https://doi.org/10.1146/annurev.fl.26.010194.003041>
- [85] J. Lighthill, *An informal introduction to theoretical fluid mechanics*. Oxford University Press; New York, 1986.
- [86] S. H. Lamb, *Hydrodynamics, Sixth Edition*. Press Syndicate of the University of Cambridge, 1932.
- [87] P. Oshkai and D. Rockwell, “Free surface wave interaction with a horizontal cylinder,” *Journal of Fluids and Structures*, vol. 13, no. 7-8, pp. 935–954, Oct. 1999. [Online]. Available: <https://doi.org/10.1006/jfls.1999.0237>
- [88] F. F. Siala and J. A. Liburdy, “Leading-edge vortex dynamics and impulse-based lift force analysis of oscillating airfoils,” *Experiments in Fluids*, vol. 60, no. 10, Sep. 2019. [Online]. Available: <https://doi.org/10.1007/s00348-019-2803-5>
- [89] D. Iverson, M. Rahimpour, W. Lee, T. Kiwata, and P. Oshkai, “Effect of chordwise flexibility on propulsive performance of high inertia oscillating-foils,” *Journal of Fluids and Structures*, vol. 91, p. 102750, Nov. 2019. [Online]. Available: <https://doi.org/10.1016/j.jfluidstructs.2019.102750>
- [90] J. C. R. Hunt, A. A. Wray, and P. Moin, “Eddies, streams, and convergence zones in turbulent flows,” *Center for Turbulence Research, Proceedings of the Summer Program*, 1988.
- [91] A. M. Mitchell and P. Molton, “Vortical substructures in the shear layers forming leading-edge vortices,” *AIAA Journal*, vol. 40, no. 8, pp. 1689–1692, Aug. 2002. [Online]. Available: <https://doi.org/10.2514/2.1844>
- [92] N. C. Lambourne and D. W. Bryer, “The bursting of leading-edge vortices some observations and discussion of the phenomenon,” *Aeronautical Research Council Reports and Memoranda*, no. 3282, 1961.
- [93] C. Wang, Q. Gao, R. Wei, T. Li, and J. Wang, “3d flow visualization and tomographic particle image velocimetry for vortex breakdown over a non-slender delta wing,” *Experiments in Fluids*, vol. 57, no. 6, May 2016. [Online]. Available: <https://doi.org/10.1007/s00348-016-2184-y>

- [94] T. Sarpkaya, “On stationary and travelling vortex breakdowns,” *Journal of Fluid Mechanics*, vol. 45, no. 3, pp. 545–559, Feb. 1971. [Online]. Available: <https://doi.org/10.1017/s0022112071000181>
- [95] B. Khoo, K. Yeo, D. Lim, and X. He, “Vortex breakdown in an unconfined vortical flow,” *Experimental Thermal and Fluid Science*, vol. 14, no. 2, pp. 131–148, Feb. 1997. [Online]. Available: [https://doi.org/10.1016/s0894-1777\(96\)00033-7](https://doi.org/10.1016/s0894-1777(96)00033-7)
- [96] A. Y. Gelfgat, P. Z. Bar-Yoseph, and A. Solan, “Three-dimensional instability of axisymmetric flow in a rotating lid–cylinder enclosure,” *Journal of Fluid Mechanics*, vol. 438, pp. 363–377, Jul. 2001. [Online]. Available: <https://doi.org/10.1017/s0022112001004566>
- [97] M. R. Ruith, P. CHEN, E. Meiburg, and T. Maxworthy, “Three-dimensional vortex breakdown in swirling jets and wakes: direct numerical simulation,” *Journal of Fluid Mechanics*, vol. 486, pp. 331–378, Jun. 2003. [Online]. Available: <https://doi.org/10.1017/s0022112003004749>
- [98] S. L. Dizès, M. Rossi, and H. K. Moffatt, “On the three-dimensional instability of elliptical vortex subjected to stretching,” *Physics of Fluids*, vol. 8, no. 8, pp. 2084–2090, Aug. 1996. [Online]. Available: <https://doi.org/10.1063/1.868982>
- [99] J. N. Sørensen, I. V. Naumov, and V. L. Okulov, “Multiple helical modes of vortex breakdown,” *Journal of Fluid Mechanics*, vol. 683, pp. 430–441, Aug. 2011. [Online]. Available: <https://doi.org/10.1017/jfm.2011.308>
- [100] I. Delbende, M. Rossi, and S. L. Dizès, “Stretching effects on the three-dimensional stability of vortices with axial flow,” *Journal of Fluid Mechanics*, vol. 454, pp. 419–442, Mar. 2002. [Online]. Available: <https://doi.org/10.1017/s0022112001007261>
- [101] P. R. Bandyopadhyay, “Vortex bursting near a free surface,” *Journal of Fluid Mechanics*, vol. 888, Feb. 2020. [Online]. Available: <https://doi.org/10.1017/jfm.2019.1075>
- [102] T. A. Casey, J. Sakakibara, and S. T. Thoroddsen, “Scanning tomographic particle image velocimetry applied to a turbulent jet,” *Physics of*

Fluids, vol. 25, no. 2, p. 025102, Feb. 2013. [Online]. Available: <https://doi.org/10.1063/1.4790640>

- [103] L. Eshbal, D. Kovalev, V. Rinsky, D. Greenblatt, and R. van Hout, “Tomo-PIV measurements in the wake of a tethered sphere undergoing VIV,” *Journal of Fluids and Structures*, vol. 89, pp. 132–141, Aug. 2019. [Online]. Available: <https://doi.org/10.1016/j.jfluidstructs.2019.02.003>